Non-Thermal Emission From Astrophysical Shocks and Their Observational Implications

Citation

Wang, Xiawei. 2019. Non-Thermal Emission From Astrophysical Shocks and Their Observational Implications. Doctoral dissertation, Harvard University, Graduate School of Arts & Sciences.

Non-thermal Emission from Astrophysical Shocks and their Observational Implications

A dissertation presented

by

Xiawei Wang

to

The Department of Astronomy

in partial fulfillment of the requirements

for the degree of

Doctor of Philosophy

in the subject of

Astronomy & Astrophysics

Harvard University

Cambridge, Massachusetts

April 2019

Dissertation Advisor: Professor Abraham Loeb Xiawei Wang

Non-thermal Emission from Astrophysical Shocks and their Observational Implications

Abstract

This thesis presents a series of studies on the non-thermal emission produced by collisionless shocks in various astrophysical systems and their observational implications. First, we discuss the hydrodynamics and multi-messengers from AGN outflows, which account for the missing component of the extragalactic gamma-ray background, cumulative neutrino background and ultra high energy cosmic rays. This is the first model that simultaneously accounts for all three messengers at their observed levels without parameters tuning. Next, we introduce a new model for the ignition of star formation in low-mass halos at high redshifts that otherwise do not form stars. A passing shock could trigger star formation and generate a self-sustaining starburst front. This model makes new predictions for illuminated cosmic filaments that can by tested by state-of-the-art instrumentation. In addition, we discuss star formation in AGN outflows in massive galaxies as a new mechanism for hypervelocity star production. Moreover, we show that non-thermal emission can be used to probe floating black holes in the Milky Way as well as gaseous halos at high redshifts. Finally, we branch out the application to planetary systems. The interaction between the planet's magnetoshpere and the stellar wind of the host star produces a bow shock that produces non-thermal emission detectable in multi-wavelengths. This opens a new window for the detection of exoplanet systems as well as provide constraints on their physical properties.

Contents

Acknowledgments

First and foremost, I would like to express my deepest gratefulness to my advisor, Avi Loeb. His wisdom, guidance and encouragement lit my path along the way. With all the challenges and complexities of understanding the Universe, I would have been lost if it weren't for his unfailing and tremendous supports. Thank you Avi, for giving me a chance to see potentials rather than limitations. Thank you for making me realize all the marvelous possibilities in the world.

I would like to thank my committee members, Josh Grindlay, Doug Finkbeiner, Mark Reid and Claude-André Faucher-Giguère for insightful feedbacks on my research projects throughout the years. Their helpful comments have significantly improved this thesis.

To the CfA administration, Robb Scholten, Peg Herlihy, Nina Zonnevylle, Uma Mirani, Mark Palmer, and members of CFhelp, CfA and ITC staff. Thank you all for your help and supports that made my graduate school experience so smooth.

In addition, I would like to thank all graduate students in the Astronomy department, postdocs, research scientists in the CfA for many years of inspiration and supports.

Last but not least, I would like to thank my family and friends. Thank you all for always being there for me and holding my hands along the way.

To my loved ones – I am observing the Universe on your behalf.

Chapter 1

Introduction

In this thesis, I have established analytical models to study the non-thermal emission from astrophysical shocks in a various of systems and their observational implications to understand some of the biggest puzzles in modern astronomy. This thesis is organized as follows. In chapter 2-chapter 5, we discuss the hydrodynamics and multi-messengers from quasar-driven outflows and their observational implications. In chapter 6-chapter 7, we investigate star formation triggered by shocks from active galactic nuclei (AGN) outflows. In chapter 8, we describe the non-thermal emission from intermediate mass black hole in the Milky Way. In chapter 9, we discuss a new probe to exoplanet systems via the non-thermal emission from the planet-star interaction.

1.1 Astrophysical Shocks

Shock waves are ubiquitous in astrophysical systems such as: supernova and γ-ray burst blast waves, stellar wind encountering medium, cloud-cloud collisions, accretion onto compact objects, expansion of H_{II} regions into neutral medium, interplanetary shock due to solar flares and coronal mass ejections.

A shock wave is a propagating disturbance that travels faster than the local speed of sound in the medium. It carries energy and propagates through a medium, characterized by an abrupt, nearly discontinuous, change in pressure, temperature, and density of the medium. The irreversible character of a shock wave is due to increase of entropy as kinetic energy is dissipated into heat. In most astrophysical systems, the mean free path to Coulomb collisions between particles is much larger than the scales of the system due to the low density of plasma. This indicates that the dissipation may be collisionless, and due to collective motions of the charged particles and the resulting electromagnetic fields. It has been proposed that the mechanism driving these collisionless shocks consists of plasma instabilities, on the order of plasma skin depth, which is much shorter than the mean free path of Coulomb collisions. See Zel'dovich & Raizer (1967) for more detailed physics on shock waves.

1.1.1 Fermi Acceleration

Fermi acceleration is a process where charged particles are repeatedly reflected by a magnetic field. It is suggested to be the primary mechanism by which particles obtain non-thermal energies in astrophysical shock waves. There are two types of Fermi acceleration: first-order acceleration in shocks and second-order Fermi acceleration in the environment of moving magnetized gas clouds. Fermi acceleration only applies to particles with energies exceeding the thermal energies, thus frequent collisions with surrounding particles in the medium will lead to significant energy loss. Thus, the medium has to be collisionless in order for the mechanism to be effective.

Shock waves are characterized to exhibit moving magnetic inhomogeneities both preceding and follwing them. If a charged particle propagates through the shock wave from downstream to upstream and encounters a moving change in the magnetic field, it can be reflected back through the shock from downstream to upstream at an increased speed. Multiple reflections significantly raise the particle energy. The resulting energy spectrum of particles going through this process is a power-law. The power-law index for non-relativistic shocks depends on the compression ratio.

See Blandford & Eichler (1987) for more details on Fermi acceleration by shock waves.

1.2 Non-thermal Emission

If the characteristics of the emitted radiation do not depend on the temperature of the source, the radiation is known as non-thermal radiation, where as the thermal radiation is dependent solely on the temperature of the emitter. In this thesis, we mainly model four types of non-thermal emission to probe astrophysical systems: synchrotron radiation, inverse Compton scattering, synchrotron self-Compton radiation and γ-ray processes.

1.2.1 Synchrotron Radiation

If a charged particle travels near the speed of light and propagates through a magnetic field, it spirals along the magnetic field lines in helical paths. The change in the electron's direction of motion indicates that they are accelerated, and thus will emit radiation, which is known as the synchrotron radiation. The spectrum from a single electron is not a power-law. However, if the energy distribution of the electrons is a power law as accelerated via Fermi acceleration, the superposition of individual electron spectra will appear to follow a power-law. There are some useful characteristics of synchrotron radiation:

- It's highly collimated, which indicates that the radiation seems to be coming from a thin cone.
- It's highly polarized, with the degree and orientation of the polarization providing information about the magnetic fields.
- It's emitted over a wide range of frequencies, which results in a wide energy spectrum.

Synchrotron radiation can be traced in many astrophysical systems, such as supernovae, pulsars, jets emanating from active galaxies and near black holes.

1.2.2 Inverse Compton Scattering

Inverse Compton (IC) scattering is a process in which low energy photons are scattered to high energies by relativistic electrons, as opposite of the standard Compton effect. The low energy photons are called the soft photons. The frequency of the scattered soft photons of ν_0 is $\nu \approx \gamma^2\nu_0$, where γ is the electron's Lorentz factor. Thus, IC is an efficient way to drain high energy electrons as they propagate through a source with large density of soft photons.

IC scattering is an important radiation mechanism in X-ray astronomy. For example, the lower energy photons from an accretion disk around a black hole are scattered to higher energies by relativistic electrons in the surrounding corona, which results in the power-law component in the 0.2-10 keV X-ray spectra of an accreting black hole. Another prominent effect is when the cosmic microwave background (CMB) photons move through the hot gas surrounding a galaxy cluster. The CMB photons are upscattered, known as the Sunyaev-Zeldóvich effect.

1.2.3 Synchrotron self-Compton Radiation

Synchrotron self-Compton (SSC) radiation results from inverse Compton scattering of synchrotron radiation by the same relativistic electrons that produced the synchrotron radiation. The self-Compton contributes to the radiation energy density and could lead to significant second order scattering since the SSC contribution to radiation energy density approaches the synchrotron contribution. Such a runaway positive feedback is sensitive to the brightness temperature of the source. Thus, IC loss significantly cools the relativistic electrons in sources with brightness temperature $\gtrsim 10^{12}$ K in the rest frame of the source.

1.2.4 γ-ray Processes

In addition to synchrotron radiation, IC scattering and relativistic Bremsstrahlung, another important mechanism to produce high energy γ-ray photons is via the decay of neutral pions by relativistic protons and ambient protons in the source medium. The process is known as *pp* process, which creates neutral and charges pions. Neutral pions will further decay to make γ-ray photons while charged pions will decay into muons and neutrinos.

See Rybicki & Lightman (1979) for more details and derivations on the non-thermal emission from high energy particles in this section.

1.3 Observational Implications

With the recent detection of gravitational wave by the advanced laser interferometer gravitational-wave observatory (aLIGO), the new era of multi-messenger astronomy has arrived. We have established the capability to see the same cosmic events in the electromagnetic light, particles and gravitational waves, giving us a more coherent picture of universe's most mysterious phenomena. This thesis discusses observational implications associated with non-thermal emission from astrophysical shocks across a broad range of wavelengths, which can be tested by the state-of-the-art and upcoming facilities such as the *Jansky Very Large Array*, *Square Kilometer Array*, *Atacoma Large Millimeter/submillimeter Array*, *James Webb Space Telescope*, *Hubble Space Telescope*, *Chandra*, *XMM-Newton*, *Advanced Telescope for High Energy Astrophysics*, *Nuclear Spectroscopic Telescope Array*, *Fermi Large Area Telescope*, *IceCube Neutrino Observatory*, *Pierre Auger Observatory* and *Telescope Array*.

Chapter 2

Probing the Gaseous Halo with Non-Thermal Emission from AGN-Driven Outflows

This thesis chapter originally appeared in the literature as

X. Wang & A. Loeb, Probing the Gaseous Halo with Non-Thermal Emission from AGN-Driven Outflows, *Monthly Notices of the Royal Astronomical Society*, 453, 837 (2015)

Abstract

Feedback from outflows driven by active galactic nuclei (AGN) can affect the distribution and properties of the gaseous halos of galaxies. We study the hydrodynamics and non-thermal emission from the forward outflow shock produced by an AGN-driven outflow. We consider a few possible profiles for the halo gas density, self-consistently constrained by the halo mass, redshift and the disk baryonic concentration of the galaxy. We show that the outflow velocity levels off at $\sim 10^3\,\mathrm{km\,s^{-1}}$ within the scale of the galaxy disk. Typically, the outflow can reach the virial radius around the time when the AGN shuts off. We show that the outflows are energy-driven, consistently with observations. The outflow shock lights up the halos of massive galaxies across a broad wavelength range. For Milky Way (MW) mass halos, radio observations by *The Jansky Very Large Array* (*JVLA*) and *The Square Kilometer Array* (*SKA*) and infrared/optical observations by *The James Webb Space Telescope* (*JWST*) and *Hubble Space Telescope* (*HST*) can detect the emission signal of angular size $\sim 8''$ from galaxies out to redshift $z \sim 5$. Millimeter observations by *The Atacama Large Millimeter/submillimeter Array* (*ALMA*) are sensitive to non-thermal emission of angular size $\sim 18''$ from galaxies at redshift $z \lesssim 1$, while X-ray observations by *Chandra*, *XMM-Newton* and *The Advanced Telescope for High Energy Astrophysics* (*ATHENA*) is limited to local galaxies ($z \lesssim 0.1$) with an emission angular size of $\sim 2'$. Overall, the extended non-thermal emission provides a new way of probing the gaseous halos of galaxies at high redshifts.

2.1 Introduction

Outflows from active galactic nuclei (AGN) regulate black hole (BH) growth (Silk & Rees 1998; Di Matteo et al. 2005) and may quench star formation in galaxies (Springel et al. 2005; Hopkins et al. 2008). A great amount of observational evidence has demonstrated the presence of AGN-driven outflows, including observations of absorptions in quasars (Ganguly et al. 2007; Fu & Stockton 2009; Moe et al. 2009; Villar-Martín et al. 2011;

Arav et al. 2013, 2015; Zakamska & Greene 2014) , multiphase outflows in nearby ultraluminous infrared galaxies (Rupke & Veilleux 2011; Sturm et al. 2011; Cicone et al. 2014; Feruglio et al. 2015; Tombesi et al. 2015) and quasars (Carniani et al. 2015; Gofford et al. 2015), and post-starburst galaxies (Tripp et al. 2011). The velocity of AGN-driven outflows can reach $\sim 10^3\,\mathrm{km\,s^{-1}}$ on galaxy scale, indicating that the outflows are likely to propagate into the halos of galaxies while the AGN is active. Here we propose to use AGN-driven outflows as a probe of the halo gas in galaxies.

Halo gas has been identified in multiphases (see review by Putman et al. (2012)): cold neutral hydrogen detected as high velocity clouds (Kalberla et al. 2005; Westmeier et al. 2005; Oosterloo et al. 2007; Saul et al. 2012), warm gas ($T \sim 10^{4-5}$ K) discovered in deep Hα emission line surveys (Putman et al. 2003; Lehner et al. 2012), warm-hot gas ($T \sim 10^{5-6}$ K) detected in absorption (Prochaska & Hennawi 2009; Wakker & Savage 2009; Savage et al. 2011; Marasco et al. 2013; Farina et al. 2014; Ford et al. 2014) and hot gas ($T \sim 10^6$ K) inferred from X-ray observations in emission and absorption (Bogdán et al. 2013, 2015; Miller & Bregman 2013). The presence of warm-hot and hot halo gas, extending out to the virial radius, is of particular interest since the hot gas is postulated to host a significant fraction of baryons in the galaxy (Kaufmann et al. 2006). However, the detailed properties and the origin of the extended and diffuse hot halo gas remain uncertain since there is little evidence for its existence around spiral galaxies (Putman et al. 2012). The detection of halo gas out to virial radius scale is difficult and the extent to which the outflows impact the properties of the halo gas remains uncertain. Therefore, it is important to study the interaction between AGN-driven outflows and surrounding gas on different scales as a probe of the properties of the diffuse hot halo gas and the effectiveness of the feedback mechanism.

It remains unclear whether outflows in galaxies are dominated by AGN or supernovae (SN; Hopkins et al. (2016)). In this chapter, we focus on AGN-driven outflows. First, our model assumes spherical symmetry, which is more justified for AGN-driven outflows since they are launched at the center of the galaxy whereas SN-driven outflows are distributed throughout the entire disk. More importantly, as shown later in the chapter, the strongest emission signal comes from more massive galaxies where AGN feedback is thought to dominate.

Previous work on the dynamics of galactic outflows have made simple assumptions about the total gravitational mass and the gaseous environment in which the outflow propagates (Furlanetto & Loeb 2001; King 2003; King et al. 2011; Faucher-Giguère & Quataert 2012; Nims et al. 2015), and limited the evolution of the outflows to galactic disk scales (Jiang et al. 2010; Faucher-Giguère & Quataert 2012; Hopkins et al. 2016; Nims et al. 2015). In this chapter, we explore different gas density profiles in galaxy halos and examine the non-thermal emission from the forward shock plowing into the ambient medium in details. We make observational predictions and discuss how the outflow shock and halo gas affect each other. We propose a new way to probe the gaseous halo using the non-thermal emission from the outflow shocks as they travel through the ambient medium in the galaxy and halo.

This chapter is organized as follows. In § 2.2, we describe our model for the halo and gas distribution. In § 2.3, we analyze the hydrodynamics of AGN-driven outflows. In § 2.4, we calculate the non-thermal emissions from shocks produced by outflows. In § 2.5, we show numerical results for representative cases and discuss physical significance. Finally in § 2.6, we summarize our results and discuss their implications.

2.2 Model Description

We approximate the galaxy and halo as spherically symmetric. The environment into which the outflow propagates is decribed below. Here we discuss properties of spherical outflows driven by fast nuclear wind (Jiang et al. 2010; King & Pounds 2015). The predicted radio emission from outflow shocks as discussed in § 2.4 is fainter than the radio synchrotron emission from relativistic jets in a small subset of all active galaxies (Heckman & Best 2014).

2.2.1 Mass Profile of Host Galaxy

We assume that the density distribution of the galaxy in which the outflow is initially embedded follows the NFW profile (Navarro et al. 1996):

$$\rho_{\text{NFW}}(R) = \rho_0 (1+z)^3 \frac{\Omega_m}{\Omega_m(z)} \frac{\delta_c}{c_{_N} x (1+c_{_N} x)^2} \ , \tag{2.1}$$

where $\rho_0 = 3H_0^2/8\pi G$ is the critical density today, H_0 is the Hubble constant today, G is the gravitational constant, $x = R/R_{\text{vir}}$, $c_{_N}$ is the concentration parameter which is roughly given by: $c_{_N} \approx 25(1+z)^{-1}$, $\Omega_m = 0.3$. δ_{c} is given by $\delta_c = \Delta_c c_N^3/[3(\ln(1+c_{_N}) - c_{_N}/(1+c_{_N}))]$, where $\Delta_c \approx 18\pi^2$. $\Omega_{\text{m}}(z)$ can be expressed as $\Omega_m(z) = \Omega_m(1+z)^3/[\Omega_m(1+z)^3 + \Omega_\Lambda]$, where $\Omega_\Lambda = 0.7$. R_{vir} is the virial radius, written as $R_{\text{vir}} = 0.78\, h^{-2/3} \left[\Omega_{\text{m}}\Delta_{\text{c}}/18\pi^2\Omega_{\text{m}}(z)\right]^{-1/3} M_{\text{h},8}^{1/3}/(1+z/10)\,\text{kpc}$, where $h = (H_0/100\,\text{km}\,\text{s}^{-1})$ is the Hubble parameter and $M_{\text{h}} = 10^8 M_{\text{h},8} M_\odot$ is the halo mass. We obtain the total mass of the galaxy and dark matter halo within a radius of R by

$\int 4\pi R^2 \rho_{_{\rm NFW}}(R)\, dR$, which gives:

$$\begin{aligned} M_{\rm DM}(R) =& \rho_0 (1+z)^3 \frac{\Omega_m}{\Omega_m(z)} \frac{\delta_c R_{\rm vir}^3}{c_{_N}^3} \\ & \left[\ln(1+c_{_N}x) - \frac{c_{_N}x}{1+c_{_N}x} \right] . \end{aligned} \tag{2.2}$$

We estimate the BH mass $M_\bullet$ self-consistently by the following steps (Guillochon & Loeb 2015). First we obtain the total stellar mass in the galaxy $M_\star$ determined by $M_{\rm h}$ (Moster et al. 2010):

$$M_\star = M_{\star,0} \frac{(M_{\rm h}/M_1)^{\gamma_1}}{\left[1 + (M_{\rm h}/M_1)^\beta\right]^{(\gamma_1 - \gamma_2)/\beta}} , \tag{2.3}$$

where $\log(M_{\star,0}/M_\odot) = 10.864$, $\log(M_1/M_\odot) = 10.456$, $\gamma_1 = 7.17$, $\gamma_2 = 0.201$ and $\beta = 0.557$. There is no specific bulge mass $M_{\rm bulge}$ for a given halo mass (Kormendy & Ho 2013). Numerical simulation (Bluck et al. 2014) suggests that the bulge-to-total stellar mass ratio B/T=$M_{\rm bulge}/M_\star$ is roughly uniformly distributed from 0 to 1. This ratio for the MW is ~ 0.15 (Licquia & Newman 2014). Additionally, Fisher & Drory (2011) suggest that $\sim 25\%$ of all local stellar mass is in bulges and elliptical galaxies. We then adopt a particular value of B/T ratio to be $\sim 30\%$ in our calculation and multiply this value by $M_\star$ to get $M_{\rm bulge}$ to illustrate some examples. There is likely to be only ellipticals in high mass halos, so it is justified to take a fixed B/T ratio for these systems. We also verify that modifying B/T ratio only results in a difference within a factor of 4. This variation can be cancelled out by the uncertainty in the fraction of AGN's luminosity injected into the medium as discussed later in the chapter. Finally, we obtain the BH mass $M_\bullet$ by (McConnell & Ma 2013):

$$\log(M_\bullet/M_\odot) = 8.46 + 1.05 \log\left[\frac{M_{\rm bulge}}{10^{11} M_\odot}\right] . \tag{2.4}$$

2.2.2 Gas Density Profile

We assume that the gas takes up a fraction $f_{\rm g}$ of the total mass of the dark matter in a galaxy. We adopt a cosmic mean baryon fraction, which is $f_{\rm g} \sim 16\%$ (Hinshaw et al. 2013). A fraction of the baryons $f_{\rm d}$ is concentrated in the disk of the galaxy, and the disk radius $R_{\rm disk}$ is taken to be $\sim 4\%$ of the virial radius $R_{\rm vir}$ (Shibuya et al. 2015).

Our first prescription for the gas density distribution is a broken power-law profile, given by:

$$\rho_{\rm pl}(R) = \begin{cases} C_{\rm d}\, R^{-\alpha} \quad (R \leq R_{\rm disk}) \\ C_{\rm h}\, R^{-\beta} \quad (R_{\rm disk} < R \leq R_{\rm vir}) \end{cases} \tag{2.5}$$

where α and β are the power-law indices in the disk and halo component, respectively. We assume an isothermal sphere for the gas within the disk component and fix $\alpha = 2.0$ in our calculation. The constants in the density profile $C_{\rm d}$ and $C_{\rm h}$ can be constrained by the baryon mass budget in the disk component and in total. Consequently, β is solely dependent on $f_{\rm d}$. The constraint on β by $f_{\rm d}$ is shown in Fig.2.1, where we find that when $f_{\rm d} \sim 0.25$, $\beta \sim 3$, indicating that the gas in the halo approximately follows the NFW profile. From the broken power-law density profile, we estimate the gas number density at $50 - 100$ kpc to be $10^{-5} - 10^{-4}\,{\rm cm}^{-3}$, which is consistent with numerical simulations (Sokołowska et al. 2016) and observations (Bogdán et al. 2015) of the hot halo gas distribution.

The second profile we consider for the halo gas density distribution is analogous to that of galaxy clusters, written as (Patej & Loeb 2015):

$$\rho_{\rm clu}(R) = \Gamma f_{\rm g} A \frac{(R/s)^{2\Gamma-2}}{R/r_{\rm s}\,[1+(s/r_{\rm s})(R/s)^{\Gamma}]^2}\ , \tag{2.6}$$

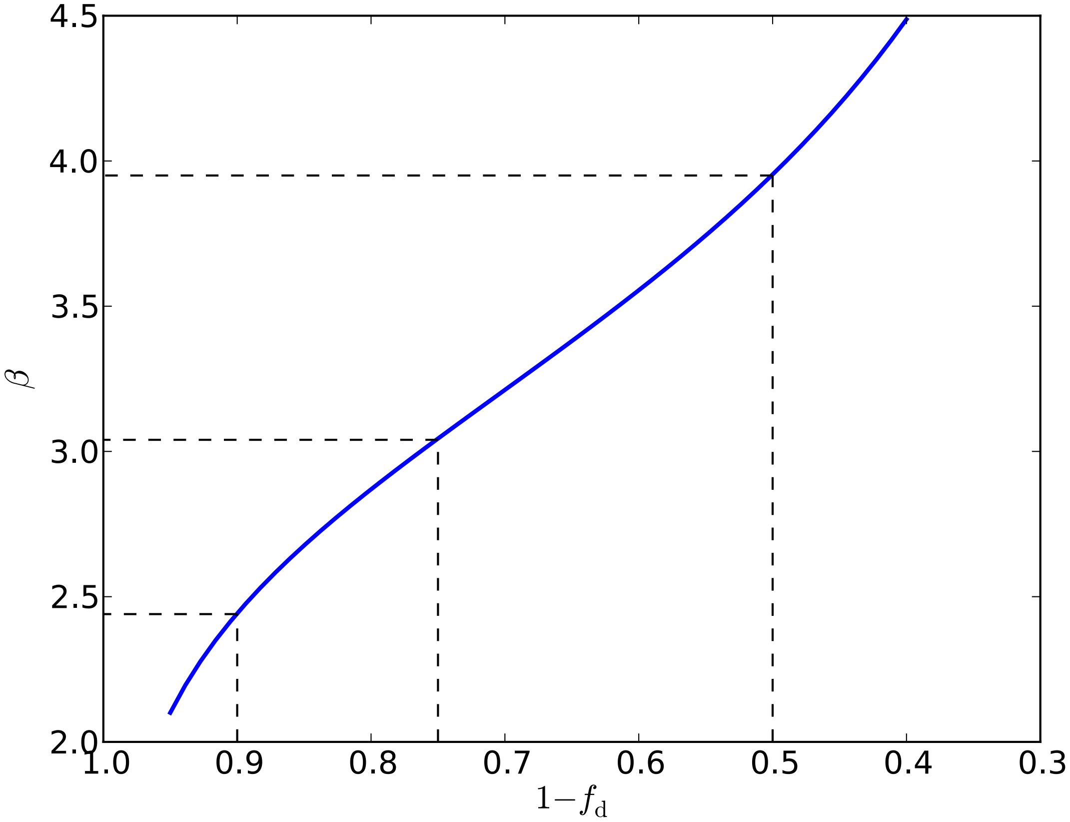

Figure 2.1 Power-law index β of the halo gas density profile as a function of the baryon fraction of the halo $(1 - f_{\rm d})$. The dashed lines correspond to values of $f_{\rm d} = 0.1$, 0.25 and 0.5, which we have taken into numerical calculation in the following sections.

where $A = \rho_0 \delta_{\rm c}$ is the scale parameter, $s = R_{\rm vir}$, $r_{\rm s} = s/c_N$ is the scale radius and Γ is the jump ratio. The density profile recovers to a scaled NFW profile for $\Gamma = 1$.

2.3 Hydrodynamics

We assume spherical symmetry for the outflow and the ambient medium. Fast wind with velocity $\sim 0.1c$ is injected into the medium, as inferred from observations of broad absorption lines in quasars (Arav et al. 2013). The wind drives an outer forward shock into the ambient medium accelerating the swept-up material and an inner reverse shock into the wind decelerating itself, separated by a contact discontinuity (King & Pounds 2015).

The equation of motion of the shell is given by (Furlanetto & Loeb 2001; Faucher-Giguère & Quataert 2012):

$$\frac{d^2 R_{\rm s}}{dt^2} = \frac{4\pi R_{\rm s}^2}{M_{\rm s}}(P_{\rm T} - P_0) - \frac{G M_{\rm tot}}{R_{\rm s}^2} - \frac{v_{\rm s}}{M_{\rm s}}\frac{dM_{\rm s}}{dt}\,, \tag{2.7}$$

where G is the gravitational constant, and $R_{\rm s}$, $v_{\rm s}$ and $M_{\rm s}$ are the radius, velocity and mass of the swept-up shell, respectively. $M_{\rm tot}$ is the total gravitational mass inside $R_{\rm s}$ that impedes the expansion of the wind bubble, written as $M_{\rm tot} = M_{\rm DM} + M_{\rm gal} + M_\bullet + M_{\rm s}/2$, composed of the mass of dark matter $M_{\rm DM}$, galaxy $M_{\rm gal}$, the central BH $M_\bullet$, and the self-gravity of the shell. The shell mass, $M_{\rm s}$, satisfies,

$$\frac{dM_{\rm s}}{dt} = 4\pi \rho_{\rm g} R_{\rm s}^2 v_{\rm s}\,, \tag{2.8}$$

where $\rho_{\rm g}$ is the ambient gas density profile in the galaxy.

Hydrostatic equilibrium gives the temperature in the ambient medium T_0:

$$\frac{dT_0}{dR} = \frac{GM_{\rm tot}m_{\rm p}}{kR^2} - \frac{T_0}{n_{\rm g}}\frac{dn_{\rm g}}{dR}\,, \tag{2.9}$$

where $m_{\rm p}$ is the proton mass, k is the Boltzmann constant and $n_{\rm g}$ is the number density profile of the ambient gas. At virial radius $R_{\rm vir}$, T_0 reaches virial temperature $T_{\rm vir} = \mu m_{\rm p} v_{\rm c}^2/2k$ where $\mu = 0.5$ is the mean molecular weight of fully ionized gas and $v_{\rm c}$ is the circular velocity, given by $v_{\rm c} = (GM_{\rm h}/R_{\rm vir})^{1/2}$. The ambient thermal pressure is given by $P_0 = n_{\rm g}kT_0$.

The thermal pressure in the shocked wind $P_{\rm T}$ declines due to radiative energy losses and work done on the ambient gas by the expansion, at a rate:

$$\frac{dP_{\rm T}}{dt} = \frac{\Lambda}{2\pi R_{\rm s}^3} - 5P_{\rm T}\frac{v_{\rm s}}{R_{\rm s}}\,, \tag{2.10}$$

where Λ is the heating and cooling function, composed of energy injection from the central source and different physical cooling processes in the shocked wind region:

$$\Lambda = L_{\rm in} - L_{\rm ff} - L_{\rm IC} - L_{\rm syn} - L_{\rm p}\,. \tag{2.11}$$

Energy is continuously injected into the shocked wind during the quasar's lifetime, taken to be the e-folding time $\tau_{\rm Edd} \approx 4.5 \times 10^7$yrs (Martini & Weinberg 2001), with a rate of $L_{\rm in}$, which is assumed to be a fraction of the AGN's bolometric luminosity $f_{\rm in}L_{\rm AGN}$. Observations infer $f_{\rm in}$ to be $\sim 1\% - 5\%$ (Arav et al. 2013; Cicone et al. 2014) and we adopt $f_{\rm in} = 5\%$ in our calculation. We assume that $L_{\rm AGN}$ is a fraction $f_{\rm AGN}$ of the Eddington luminosity $L_{\rm Edd} = 1.38 \times 10^{38}(M_\bullet/M_\odot)\ {\rm erg\,s^{-1}}$, and adopt $f_{\rm AGN} = 0.5$ in our calculation (Shen et al. 2009).

The last four terms in the right hand side of Eqn. 2.11 account for radiative cooling. $L_{\rm ff}$ is the radiative cooling rate via free-free emission in the shocked wind. $L_{\rm IC}$ describes cooling via inverse Compton (IC) scattering off photons in the quasar's radiation field and the cosmic microwave background (CMB). $L_{\rm syn}$ represents synchrotron cooling rate. $L_{\rm p}$ refers to the cooling of protons through Coulomb collisions with the electrons. The cooling rate can be expressed as $\mu E_{\rm t}/t_{\rm c}$, where $E_{\rm t} = 2\pi R_{\rm s}^3 P_{\rm T}$ is the thermal energy in the shocked wind and $t_{\rm c}$ is the timescale corresponding to different cooling processes. The total emissivity of free-free emission is given by (Rybicki & Lightman 1979): $\epsilon_{\rm ff} = 1.4\times10^{-22}\,T_{\rm e,10}^{1/2}\,n_{\rm e,0}^2\,\bar{g}_{\rm B}$, where $\bar{g}_{\rm B}$ is the Gaunt factor, $T_{\rm e,10} = (T_{\rm e}/10^{10}\,{\rm K})$ and $n_{\rm e,0} = (n_{\rm e}/1\,{\rm cm}^{-3})$ are the electron temperature and number density, respectively. The corresponding cooling timescale is $t_{\rm ff} = \frac{3}{2}kT_{\rm e}/\epsilon_{\rm ff} = 4.69\times10^{8}\,T_{\rm e,10}^{1/2}\,n_{\rm e,0}^{-1}\,\bar{g}_{\rm B}^{-1}\,{\rm yr}$. The IC cooling time of electrons of energy $E_{\rm e}$ in soft photon radiation field can be written as (King & Pounds 2015): $t_{\rm IC} = 3m_{\rm e}^2c^3/8\pi\sigma_{\rm T}U_{\rm ph}E_{\rm e}$, where $\sigma_{\rm T}$ is the Thomson scattering cross section and $U_{\rm ph}$ is the energy density of soft photons, including AGN photons with energy density $U_{\rm AGN} = L_{\rm AGN}/4\pi R_{\rm s}^2 c$ and CMB photons with energy density $U_{\rm CMB} \approx 4.2\times10^{-13}(1+z)^4\,{\rm erg\,cm^{-3}}$. Here we consider the most efficient IC cooling limit and thus leave out non-relativistic electrons, of which the IC cooling time can be significantly longer (Faucher-Giguère & Quataert 2012). We obtain the temperature in the shocked wind by the Rankine-Hugoniot jump condition $T_{\rm e} \approx 3\mu m_{\rm p} v_{\rm in}^2/16k$. The synchrotron cooling timescale is given by $t_{\rm syn} = 1.6\times10^{12}\,B_{-6}^{-2}\,T_{e,10}^{-1}\,{\rm yr}$, where $B_{-6} = (B/10^{-6}\,{\rm G})$. If two-temperature plasma effect is taken into account (Faucher-Giguère & Quataert 2012), then the proton cooling timescale $t_{\rm p}$ can be expressed as: $t_{\rm p} \approx 1.4\times10^{9}\,R_{\rm s,kpc}^2\,L_{\rm AGN,46}^{-1}\,v_{\rm s,3}^{2/5}\,v_{\rm in,0.1}^{8/5}\,{\rm yr}$, where $v_{\rm s,3} = (v_{\rm s}/10^3\,{\rm km\,s^{-1}})$ and $L_{\rm AGN,45} = (L_{\rm AGN}/10^{45}\,{\rm erg\,s^{-1}})$.

2.4 Non-thermal Emission

Next we discuss the non-thermal emission from the outflow shock as it propagates in the ambient medium (Nims et al. 2015).

2.4.1 Synchrotron Emission

As the forward shock plows through the ambient medium supersonically, a broken power-law distribution of non-thermal electrons $N(\gamma)\,d\gamma \propto \gamma^{-p}\left(1+\gamma/\gamma_{\rm b}\right)^{-1}$ is generated via Fermi acceleration in the shock to produce non-thermal emission, where p is the power-law index. $\gamma_{\rm b}$ is the break Lorentz factor, which is obtained by equating the dynamical timescale $\sim R_{\rm s}/v_{\rm s}$ and the cooling timescale $3m_{\rm e}c/4(U_{\rm B}+U_{\rm AGN}+U_{\rm CMB})\sigma_{\rm T}\gamma$. This gives $\gamma_{\rm b} = 3m_{\rm e}cv_{\rm s}/4\sigma_{\rm T}R_{\rm s}(U_{\rm B}+U_{\rm AGN}+U_{\rm CMB})$, where $m_{\rm e}$ is the electron mass, $\sigma_{\rm T}$ is the Thomson scattering cross section and $U_{\rm B} = B^2/8\pi$ is the energy density of the magnetic field. We assume that the total non-thermal luminosity is a fraction of the kinetic energy of the swept-up material, written as $L_{\rm nt} = \epsilon_{\rm nt}L_{\rm kin} \approx \frac{1}{2}\epsilon_{\rm nt}\dot{M}_{\rm s}v_{\rm s}^2$. We calibrate the magnetic field energy density as a fraction $\xi_{\rm B}$ of the thermal energy behind the shock in what follows SN remnants (Chevalier 1998), giving:

$$U_{\rm B} = \xi_{\rm B} nkT\ . \tag{2.12}$$

Observations of radio emitting bubbles from a radio-quiet quasar imply $p \sim 2$ (Harrison et al. 2015). By fitting the radio flux from bubbles at ~ 10 kpc, we obtain $\epsilon_{\rm nt} \sim 5\%$. Coefficients $\xi_{\rm B}$ can be estimated from observations of late-time radio emission from relativistic jets associated with tidal disruption events (Bower et al. 2013), synchrotron emission from shocks between jet and circumnuclear medium (Metzger et al. 2012) as well as from an analogy with supernova (SN) remnants (Chevalier 1998). These observations imply $\xi_{\rm B} \sim 0.1$.

Finally, we calculate the synchrotron emission following the standard formula from (Pacholczyk 1970; Rybicki & Lightman 1979). The emission and absorption coefficients are given by:

$$j_\nu^{\rm syn} = c_1 B \int_{\gamma_{\rm min}}^{\gamma_{\rm max}} F(x) N(\gamma)\, d\gamma \,, \tag{2.13}$$

$$\alpha_\nu^{\rm syn} = -c_2 B \frac{1}{\nu^2} \int_{\gamma_{\rm min}}^{\gamma_{\rm max}} \gamma^2 \frac{d}{d\gamma} \left[\frac{N(\gamma)}{\gamma^2}\right] F(x)\, d\gamma \,, \tag{2.14}$$

where $c_1 = \sqrt{2}e^3/4\pi m_{\rm e}c^2$, $c_2 = \sqrt{2}e^3/8\pi m_{\rm e}^2 c^2$, $F(x) \equiv x \int_x^\infty K_{5/3}(\xi)\, d\xi$ and $K_{5/3}(x)$ is the modified Bessel function of 5/3 order. The maximum Lorentz factor $\gamma_{\rm max}$ is given by the tighter constraint of equaling the acceleration timescale $\xi_{\rm acc} R_{\rm L} c/v_{\rm s}^2$ (Blandford & Eichler 1987) to either dynamical or cooling timescale, where $\xi_{\rm acc} \sim 1$ and $R_{\rm L} = \gamma m_{\rm e}c^2/eB$ is the Larmor radius. We plot $\gamma_{\rm max}$ in unit of 10^7 as a function of outflow shock radius $R_{\rm s}$ for $M_{\rm h} = 10^{12}\, M_\odot$, $f_{\rm d} = 0.25$ and $z = 1.0$ as a representative example, shown in Fig.2.2. $\gamma_{\rm max}$ varies within a factor of ~ 5 as a result of simultaneously decreasing $v_{\rm s}$ and soft photon energy density with increasing $R_{\rm s}$. We take the minimum Lorentz factor $\gamma_{\rm min} \sim 1$ in our calculation. The synchrotron emission peaks at a frequency of $\nu_{\rm syn} = 4.2 \times 10^{14}\, B_{-6}\, \gamma_7^2\,{\rm Hz}$, where $\gamma_7 = (\gamma/10^7)$.

2.4.2 Inverse Compton Scattering

The soft photons includes those from the accretion disk and CMB. The energy density of the AGN radiation field is $U_{\rm AGN} \approx 2.8 \times 10^{-10} L_{\rm AGN,45}\, R_{\rm s,kpc}^{-2}\, {\rm erg\,cm^{-3}}$. The CMB photons have an energy density of $U_{\rm CMB} \propto (1+z)^4$, which manifests themselves as a dominant source of IC scattering at high-redshift (Celotti & Fabian 2004). The spectral

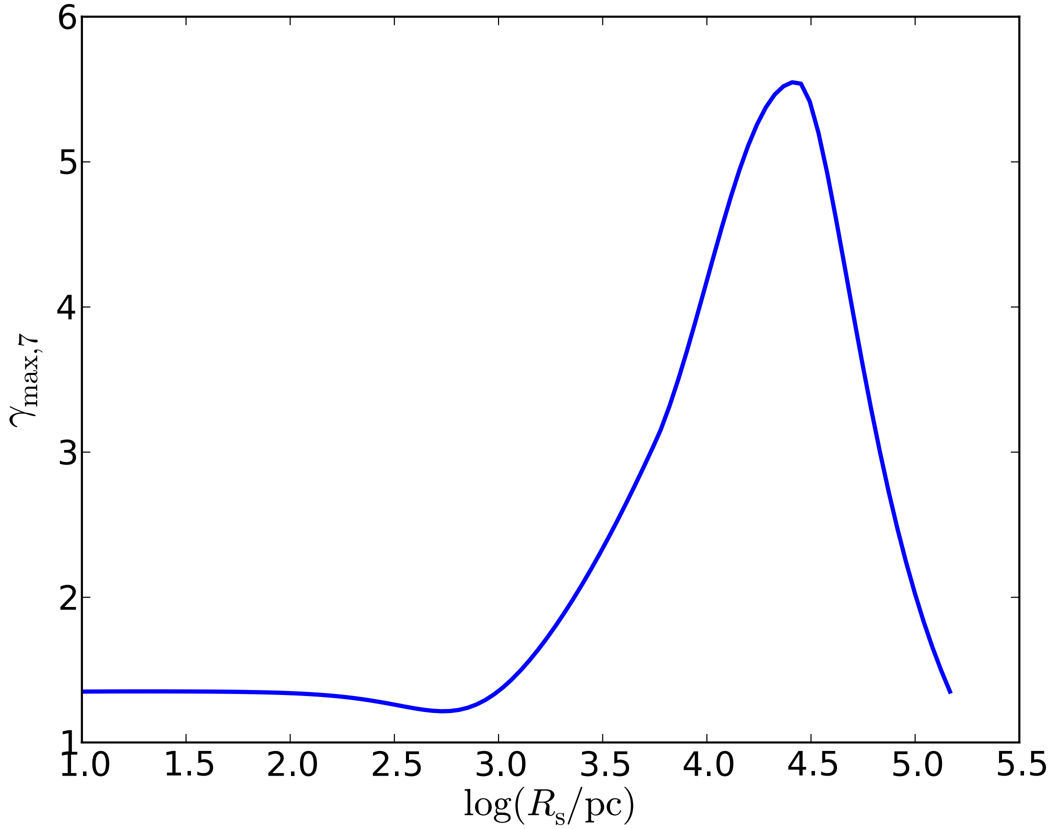

Figure 2.2 The maximum Lorentz factor of non-thermal electrons $\gamma_{\max}$ in unit of 10^7 as a function of outflow shock radius. We fix $M_{\mathrm{h}} = 10^{12}\,M_{\odot}$, $f_{\mathrm{d}} = 0.25$ and $z = 1.0$ as a representative example.

energy distribution of quasars can be constrained by observations (Elvis et al. 1994; Marconi et al. 2004; Scott & Stewart 2014). For simplicity, we approximate it as a black body spectrum (Ito et al. 2015). We model the CMB photons as a black body with a spectrum peak frequency of $\nu_{\rm CMB} \approx 1.6 \times 10^{11}(1+z)$ Hz. The peak of IC scattering of CMB photons takes place at a frequency of $\nu_{\rm IC} \approx \gamma^2 \nu_{\rm CMB} = 1.6 \times 10^{25}\, \gamma_7^2 (1+z)\,$Hz. The differential rate to produce high-energy photons with energy $\epsilon m_{\rm e} c^2$ is given by (Jones 1968; Coppi & Blandford 1990):

$$Q(\epsilon) = \int d\epsilon_0\, n(\epsilon_0) \int d\gamma N(\gamma)\, K(\epsilon, \gamma, \epsilon_0) \ , \tag{2.15}$$

where $\epsilon_0 m_{\rm e} c^2$ is the soft photon energy, $\gamma m_{\rm e} c^2$ is the electron energy and $n(\epsilon_0)$ is the number density of soft photons. $K(\epsilon, \gamma, \epsilon_0)$ is the Compton kernel, expressed as:

$$\begin{aligned} K(\epsilon, \gamma, \epsilon_0) = \frac{2\pi r_{\rm e}^2 c}{\gamma^2 \epsilon_0} [&2\kappa \ln \kappa + (1+2\kappa)(1-\kappa) \\ &+ \frac{(4\epsilon_0 \gamma \kappa)^2}{2(1+4\epsilon_0\gamma\kappa)}(1-\kappa)] \ , \end{aligned} \tag{2.16}$$

where $\kappa = \epsilon/[4\epsilon_0 \gamma(\gamma - \epsilon)]$. The emission coefficient of IC scattering can be obtained by:

$$j_\nu^{\rm IC} = \frac{h}{4\pi} \epsilon Q(\epsilon) \ , \tag{2.17}$$

where h is the Planck constant.

2.5 Numerical Results

In Figures 2.3–2.6, we show the dependence of outflow hydrodynamics solutions and emissions on $f_{\rm d}$, $M_{\rm h}$, z and density profile formulation. Since the gas distribution in the intergalactic medium (IGM) is uncertain, we restrict our calculation to halo scale within $R_{\rm vir}$.

As shown in panel *a* in Figures 2.3–2.6, we find that the swept-up shell decelerates quickly to a roughly constant velocity of $\sim 10^3\,\mathrm{km\,s^{-1}}$ in the disk. As it propagates outside the galaxy into the halo, the shell accelerates somewhat as a result of the tenuously distributed halo gas. The evolution of the shell velocity is consistent with a self-similar solution, where the shell radius is assumed to follow $R_{\mathrm{s}} \propto t^{\delta}$ and $v_{\mathrm{s}} \propto t^{\delta-1}$. We express the gas power-law density profile generally as $\rho \propto R^{\gamma}$. For $\gamma < 3$, we obtain $M_{\mathrm{s}} \propto R^{3-\gamma}$. In the energy-conserving limit, we assume that $\sim 50\%$ of the injected energy goes to the kinetic energy of the swept-up material, $L_{\mathrm{in}}t = M_{\mathrm{s}}v_{\mathrm{s}}^2$, and so we have $\delta = 3/(5-\gamma)$. For power-law index $\alpha = 2$ in our model, $\delta = 1$ and thus v_{s} approaches a constant in the disk. We can also verify that for halo component power-law index β, the outflow accelerates as $\beta > 2$. The acceleration stops as the quasar shuts off and the thermal energy in the shocked wind E_{t} drives the expansion of the shell afterwards. At this point, the outflow reaches the edge of the dark matter halo and is likely to continue to propagate into the IGM.

Panels *b* and *c* in Figures 2.3–2.6 show the radio flux as a function of shock radius and time, respectively. We scale the time to the Hubble time T_{h}, which is given by $T_{\mathrm{h}} \equiv 1/H(z) = H_0^{-1}\left[\Omega_{\mathrm{m}}(1+z)^3 + \Omega_{\Lambda}\right]^{-1/2}$. The chance of finding a galaxy with a given flux is t/T_{h}. We find that for $z \sim 1$, about a few percent of the galaxy halos embed outflows reaching R_{vir}. We also calibrate the angular diameter of the outflow shock, given by $R_{\mathrm{s}}/D_{\mathrm{A}}$, where D_{A} is the angular distance.

We show snapshots of non-thermal emission taken at two milestones in panels *e* and *f*. At the edge of the galaxy disk, the energy injection from the central source has an age of $\sim 10^7$ yrs. At the virial radius, snapshots are taken at the dead quasar remnants with outflow approaching the edge of the dark matter halo on a timescale of $\sim 10^8$ yrs, which indicates that this population should be ~ 10 times more abundant. At this point, the outflow no longer overlaps with the galaxy and there is no galaxy-bubble interactions. We find that the outflows can reach the edge of the halo around the end of quasar's lifetime. This feature indicates that AGN-driven outflows are most abundant during their passage through their host galaxy halo.

We summarize the detectability of this extended non-thermal emission in Table 2.1.

2.5.1 Dependence on Parameters

Disk mass fraction

For a halo of mass $M_{\rm h} = 10^{12}\,M_{\odot}$ at $z = 1.0$, we choose three representative values of $f_{\rm d}$ as motivated by observations (Courtois et al. 2015). We find that the shell velocity is not sensitive to $f_{\rm d}$. The outflow reaches the edge of the halo around the time the energy injection discontinues. With a velocity of $\sim 500 - 10^3\,{\rm km\,s^{-1}}$, the outflow is likely to propagate into the IGM. The non-thermal radio flux at 1 GHz remains at ~ 0.1 mJy within the disk, independent of $f_{\rm d}$. As the shell propagates into the halo, the non-thermal emission diminishes quicker in halos with higher $f_{\rm d}$ as a result of more tenuous halo gas. For $f_{\rm d} = 0.5$, the radio emission is ~ 100 times fainter than the other two cases and drops below the detection limit of *JVLA* and *SKA* before the outflow reaches $R_{\rm vir}$. Observationally, we can distinguish galaxies with high disk baryonic concentrations by the faint emission from their outflows propagating in the halos.

Table 2.1: Detectability of non-thermal emission from AGN-driven outflow shock.

	$z = 0.1$		$z = 1.0$		$z = 5.0$	
Telescopes	$F_\nu(R_{\rm disk})$; $F_\nu(R_{\rm vir})$ (mJy)	detectability	$F_\nu(R_{\rm disk})$; $F_\nu(R_{\rm vir})$ (mJy)	detectability	$F_\nu(R_{\rm disk})$; $F_\nu(R_{\rm vir})$ (mJy)	detectability
JVLA	300 ; 0.8	Yes ; Yes	1.0 ; 5×10^{-3}	Yes ; Yes	4×10^{-3} ; 6×10^{-4}	Yes ; Marginal
SKA	300 ; 0.8	Yes ; Yes	1.0 ; 5×10^{-3}	Yes ; Yes	4×10^{-3} ; 6×10^{-4}	Yes ; Marginal
ALMA	0.5 ; 4×10^{-3}	Yes ; Marginal	5×10^{-3} ; 7×10^{-5}	Marginal ; No	4×10^{-5} ; 4×10^{-4}	No ; No
JWST	3×10^{-4} ; 5×10^{-6} *	Yes ; Marginal	5×10^{-5} ; 2×10^{-6} *	Yes ; No	4×10^{-8} ; 2×10^{-5}	No ; Yes
HST	2×20^{-4} ; 5×10^{-6} *	Yes ; No	3×10^{-5} ; 2×10^{-6} *	Marginal ; No	4×10^{-8} ; 2×10^{-5}	No ; Marginal
	$\nu F_\nu(R_{\rm disk})$; $\nu F_\nu(R_{\rm vir})$ ($\rm erg\,cm^{-2}\,s^{-1}$)	detectability	$\nu F_\nu(R_{\rm disk})$; $\nu F_\nu(R_{\rm vir})$ ($\rm erg\,cm^{-2}\,s^{-1}$)	detectability	$\nu F_\nu(R_{\rm disk})$; $\nu F_\nu(R_{\rm vir})$ ($\rm erg\,cm^{-2}\,s^{-1}$)	detecatbility
XMM-Newton	10^{-16} ; 2×10^{-16}	Marginal ; Marginal	5×10^{-19} ; 4×10^{-17}	No ; No	7×10^{-20} ; 10^{-17}	No ; No
ATHENA	10^{-16} ; 2×10^{-16}	Yes ; Yes	5×10^{-19} ; 4×10^{-17}	No ; Marginal	7×10^{-20} ; 10^{-17}	No ; No
Chandra	2×10^{-17} ; 7×10^{-16}	No ; Marginal	5×10^{-19} ; 7×10^{-17}	No ; No	6×10^{-20} ; 10^{-17}	No ; No
NuSTAR	2×10^{-17} ; 7×10^{-16}	No ; No	5×10^{-19} ; 7×10^{-17}	No ; No	6×10^{-20} ; 10^{-17}	No ; No

Note: We choose $M_{\rm h} = 10^{12} M_\odot$ and $f_{\rm d} = 0.25$ as a representative example for a galaxy halo. For radio, mm/sub-mm, infrared and optical observations, we provide values of $F_\nu(R_{\rm disk})$ and $F_\nu(R_{\rm vir})$, which correspond to non-thermal flux at the edge of the disk and halo respectively, in unit of mJy. For X-ray observation, we present $\nu F_\nu(R_{\rm disk})$ and $\nu F_\nu(R_{\rm vir})$, in unit of $\rm erg\,cm^{-2}\,s^{-1}$.
The telescope detection limits are as follows:

- *The Jansky Very Large Array (JVLA)*: $\sim 1\mu$Jy for 1 σ detection and 12h integration time at most bands (National Radio Astronomy Observatory NRAO).
- *The Square Kilometer Array (SKA-MID)*: $\sim 0.7\mu$Jy RMS sensitivity for 10h integration time (Prandoni & Seymour 2014).
- *The Atacama Large Millimeter/submillimeter Array (ALMA)*: At observating frequency 345 GHz, the sensitivity $\sim 8.7\,\mu$Jy for 10h integration time is calculated by the *ALMA* Sensitivity Calculator (ASC) (https://almascience.eso.org/proposing/sensitivity-calculator).
- *The James Webb Space Telescope (JWST)*: sensitivity $\sim$ 10 nJy for wavelength $1-3\,\mu$m and $\sim$ 30nJy for wavelength $4-5\,\mu$m for 10σ detection and 10^4 s integration time (Space Telescope Science Institute STScI).
- *Hubble Space Telescope (HST)*: sensitivity $\sim$ 40 − 50 nJy for wavelength $0.6-1.5\,\mu$m for 10σ detection and 10^4 s integration time (Space Telescope Science Institute STScI).
- *Chandra*: sensitivity of high resolution camera (HRC) $\sim 9 \times 10^{-16}\rm erg\,cm^{-2}\,s^{-1}$ covering energy range 0.08 − 10 keV for 3σ detection and 3×10^5 s integration time (The Chandra Proposers' Observatory Guide 2014).
- *XMM-Newton*: $\sim 3.1 \times 10^{-16}\,\rm erg\,cm^{-2}\,s^{-1}$ in 0.5 − 2.0 keV band (Hasinger et al. 2001).
- *Advanced Telescope for High Energy Astrophysics (ATHENA)*: $\sim 4 \times 10^{-17}\,\rm erg\,cm^{-2}\,s^{-1}$ in 0.5 − 2 keV band in a 10^6s deep field (Barcons et al. 2012).
- *Nuclear Spectroscopic Telescope Array (NuStar)*: $\sim 2 \times 10^{-15}\,\rm erg\,cm^{-2}\,s^{-1}$ in 6 − 10 keV band for 3σ detection and 10^6 s integration time (Harrison et al. 2013).

* The emission may be contaminated by scattered quasar light (see § 2.6).

Halo mass

We examine $M_{\rm h}$ of $10^{11}M_\odot$, $10^{12}M_\odot$ and $10^{13}M_\odot$, covering the full range from mid to high mass halos. The energy input into outflows embedded in lower mass halos is much lower due to the self-consistent scaling relation between $M_\bullet$ and $M_{\rm h}$. The short lifetime of outflows in low mass galaxy halos makes them less abundant. Therefore, it would be observationally challenging to identify outflows from low mass halos in terms of both emission intensity and recurrence rate. At $z \sim 1$, the emission is only detectable in radio band on galaxy scale with a flux $\sim 10\,\mu$Jy. High mass galaxies produce AGN photons of higher energy density, making the detection more promising.

Redshift

The hydrodynamics of outflows is insensitive to z. Consequently, outflows reach the edge of its host galaxy and halo at similar velocities for different redshifts. At low redshift $z \sim 0.1$, the non-thermal emission is detectable in multiwavelength from radio to X-ray. For high-redshift galaxies at $z = 5$, the non-thermal emission is dominated by IC scattering off CMB photons. The emission remains observable in the radio, infrared and optical bands on halo scale.

Gas density profile

We compare the broken power-law profile to the gas density profile of galaxy clusters. We find that the outflow velocity and emission indistinguishable for these gas density profiles. However, outflows can not reach the edge of the halo for galaxy clusters, excluding them from halo scale observations in these systems.

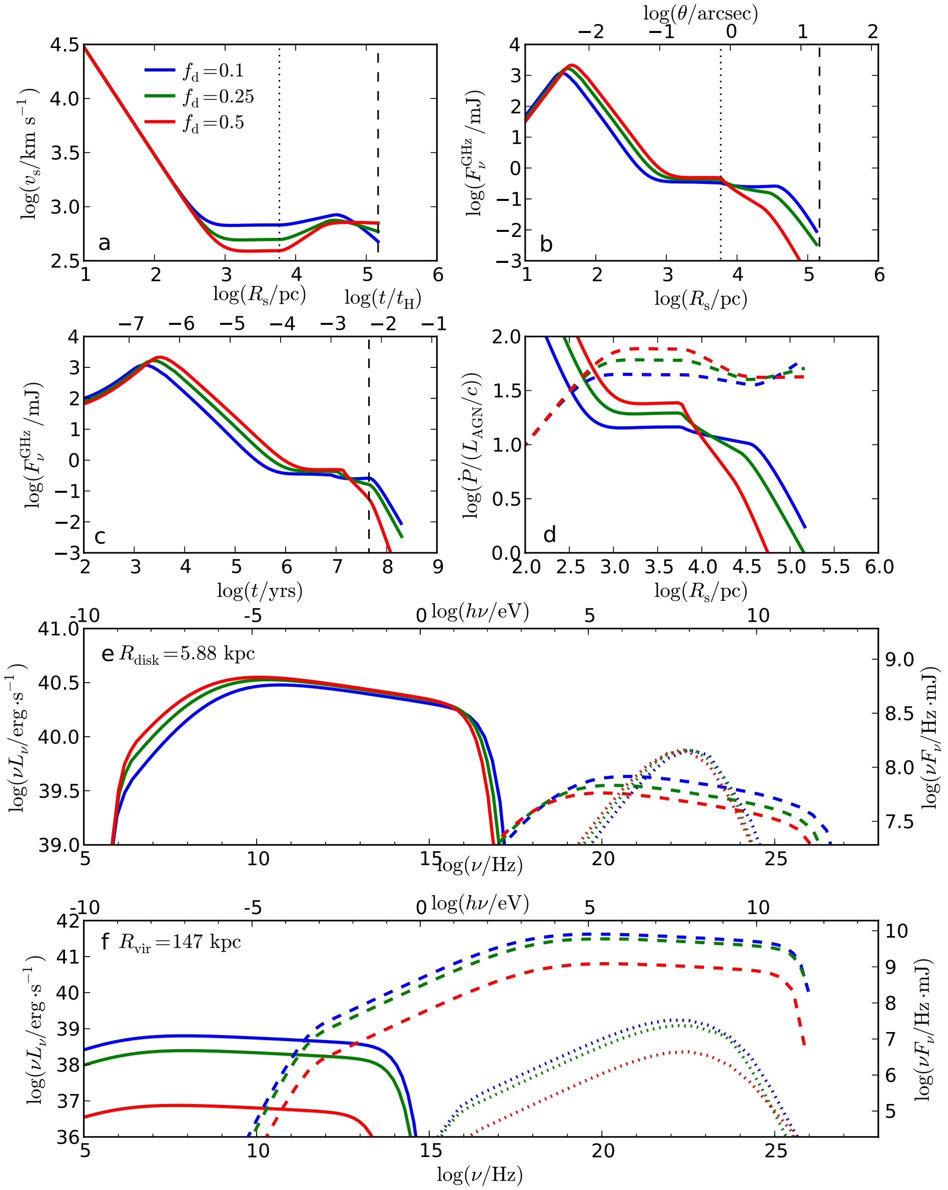

Figure 2.3 Dependence of outflow hydrodynamics and emission on baryon fraction in the disk f_{d}. We fix $M_{\mathrm{h}} = 10^{12} M_\odot$ and $z = 1.0$. Panel *a* and *b* show the shell velocity and radio synchrotron flux at 1 GHz as a function of radius. The dotted and dashed vertical lines mark the position of R_{disk} and R_{vir}, respectively. The upper x-axis of panel *b* marks the angular diameter of the outflow shock. Panel *c* shows the radio synchrotron flux as a function of time. The dashed vertical line corresponds to the point when the AGN shuts off. Time is scaled to the Hubble time T_{h} on the upper x-axis. Panel *d* demonstrates the momentum flux boost of the shell. The solid lines represent the numerical result while the dashed lines correspond to predictions in the energy-driven regime. Panel *e* and *f* illustrate snapshots of non-thermal emission power and flux at R_{disk} and R_{vir}, respectively. The solid, dashed and dotted lines correspond to synchrotron emission, IC scattering of accretion disk photons and CMB photons, respectively.

2.5.2 Energy or Momentum Conserving Outflow

Another important dynamics issue is whether the outflow is momentum or energy conserving. In the momentum-driven regime, thermal energy in the shocked wind region is efficiently radiated away, while in energy-driven outflows, such radiative losses are insignificant. We compare the timescale of the most efficient radiative cooling processes discussed in §2.3 in the shocked wind, $t_{\rm cool}$, with the dynamical timescale of the outflow, given by $t_{\rm dyn} = R_{\rm s}/v_{\rm s}$, as shown in Fig. 2.7.

The plot shows $t_{\rm cool}/t_{\rm dyn}$ for several representative cases and indicates that for some cases the outflow starts propagating as partially momentum-driven. Once the shell reaches $\sim 100\,{\rm pc}$, the partially momentum-driven regime breaks down and the shocked wind region no longer cools rapidly. At larger radii, the soft photon energy density is dominated by CMB photons and $t_{\rm cool}/t_{\rm dyn}$ decreases consequently. However, the energy conserving nature remains unchanged at larger radii, which is consistent with recent observations (Tombesi et al. 2015) and theoretical calculations (Faucher-Giguère & Quataert 2012; Zubovas & King 2012).

These results suggest that most of the wind kinetic energy is converted to the kinetic energy of the outflow, giving $\dot{P}^2/\dot{M}_{\rm s} \sim \dot{P}^2_{\rm rad}/\dot{M}_{\rm in}$, where $\dot{P}_{\rm rad} = L_{\rm AGN}/c$ is the momentum flux of AGN's radiation field and $\dot{M}_{\rm in}$ is the mass injection rate of the wind from the central source (Zubovas & King 2012). We can write the momentum flux of the outflow normalized to AGN's radiation as $\dot{P}/\dot{P}_{\rm rad} \sim v_{\rm in}/v_{\rm s}$. This relation is illustrated in panel d of Figures 3-6.

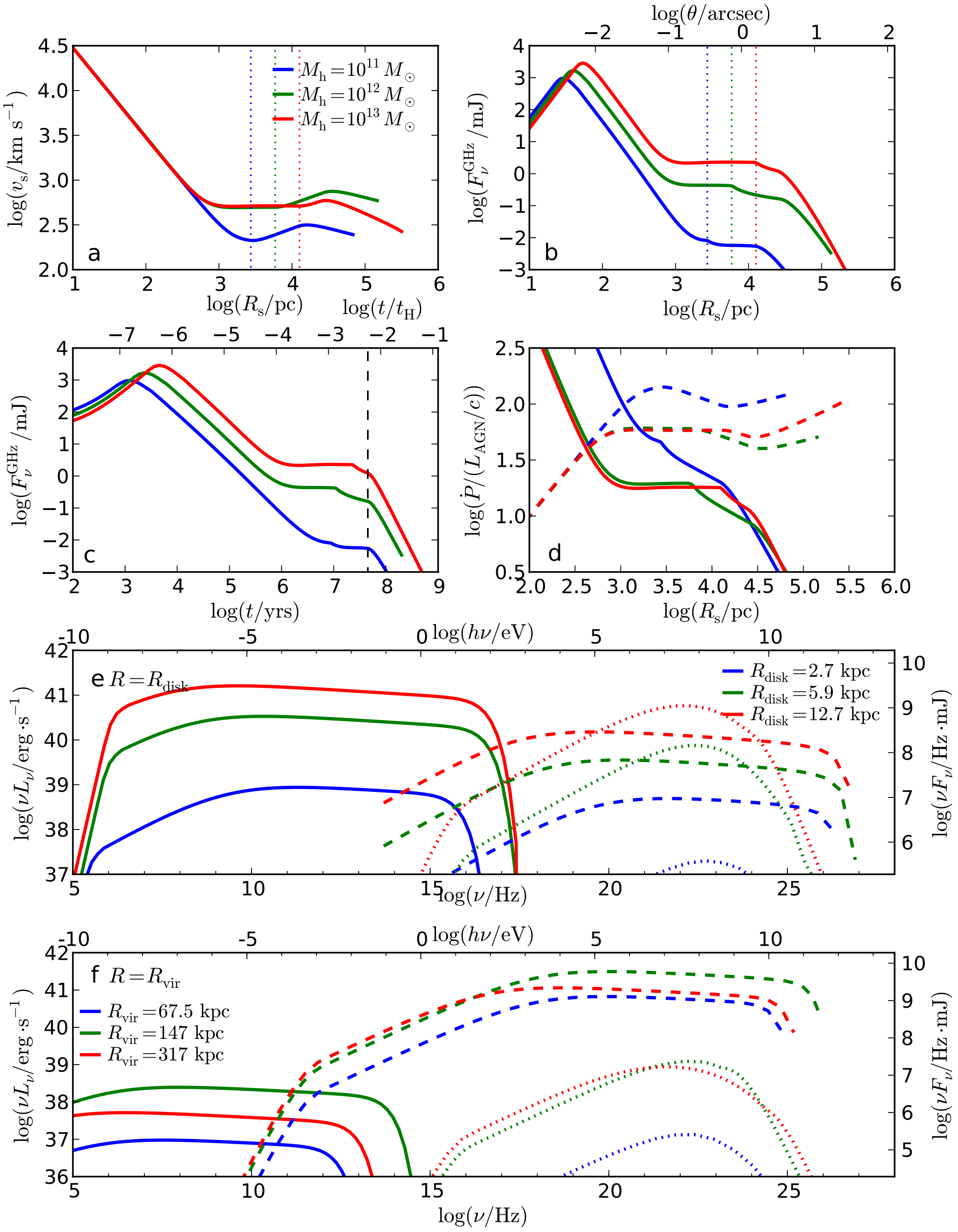

Figure 2.4 Dependence of outflow hydrodynamics and emission on halo mass M_h. We fix $f_d = 0.25$ and $z = 1.0$. The configuration and physical significance of the subplots are the same as Fig.2.3. The dotted vertical lines marks the position of R_{disk} for the three cases in panel *a* and *b*.

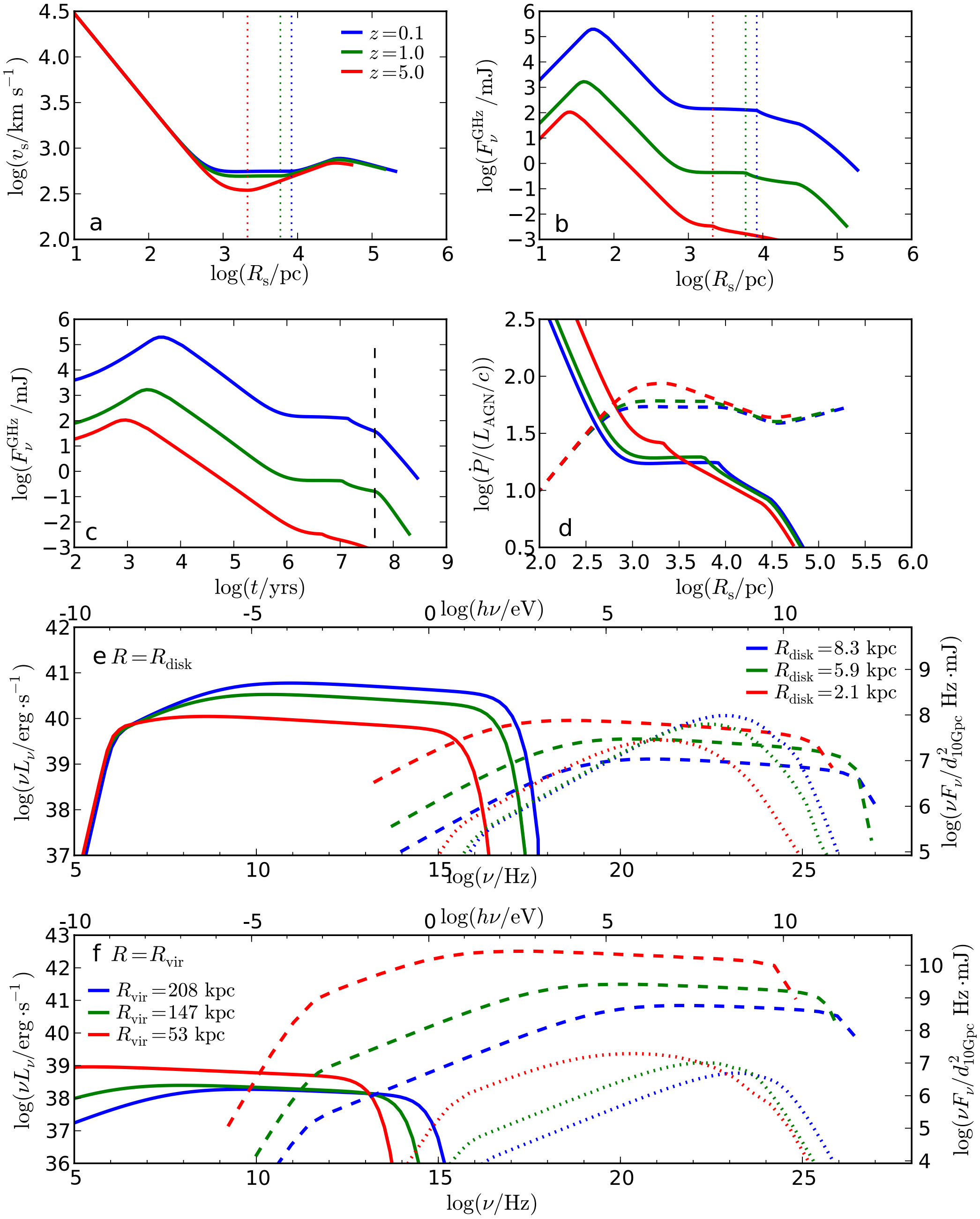

Figure 2.5 Dependence of outflow hydrodynamics and emission on redshift z. We fix $M_{\rm h} = 10^{12} M_\odot$ and $f_{\rm d} = 0.25$. The configuration and physical significance of the subplots are the same as Fig.2.3. The dotted vertical lines marks the position of $R_{\rm disk}$ for the three cases in panel a and b. The right-hand y-axis of panel e and f is scaled to a distance of 10 Gpc.

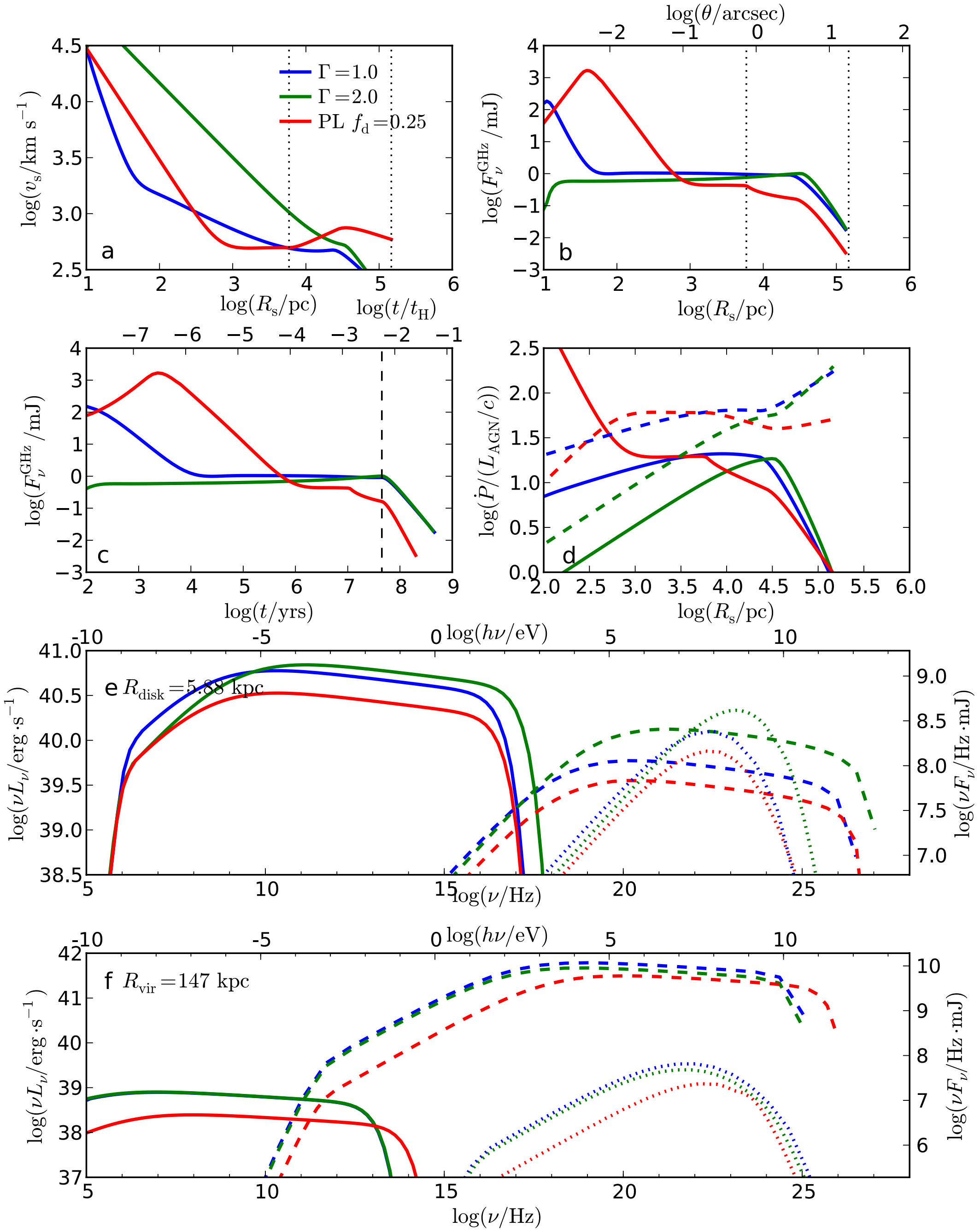

Figure 2.6 Dependence of outflow hydrodynamics and emission on gas density profile of galaxy clusters. We fix $M_h = 10^{12} M_\odot$ and $z = 1.0$. We compare galaxy cluster gas density profile with the broken power-law profile ($f_d = 0.25$). The configuration and physical significance of the subplots are the same as Fig.2.3.

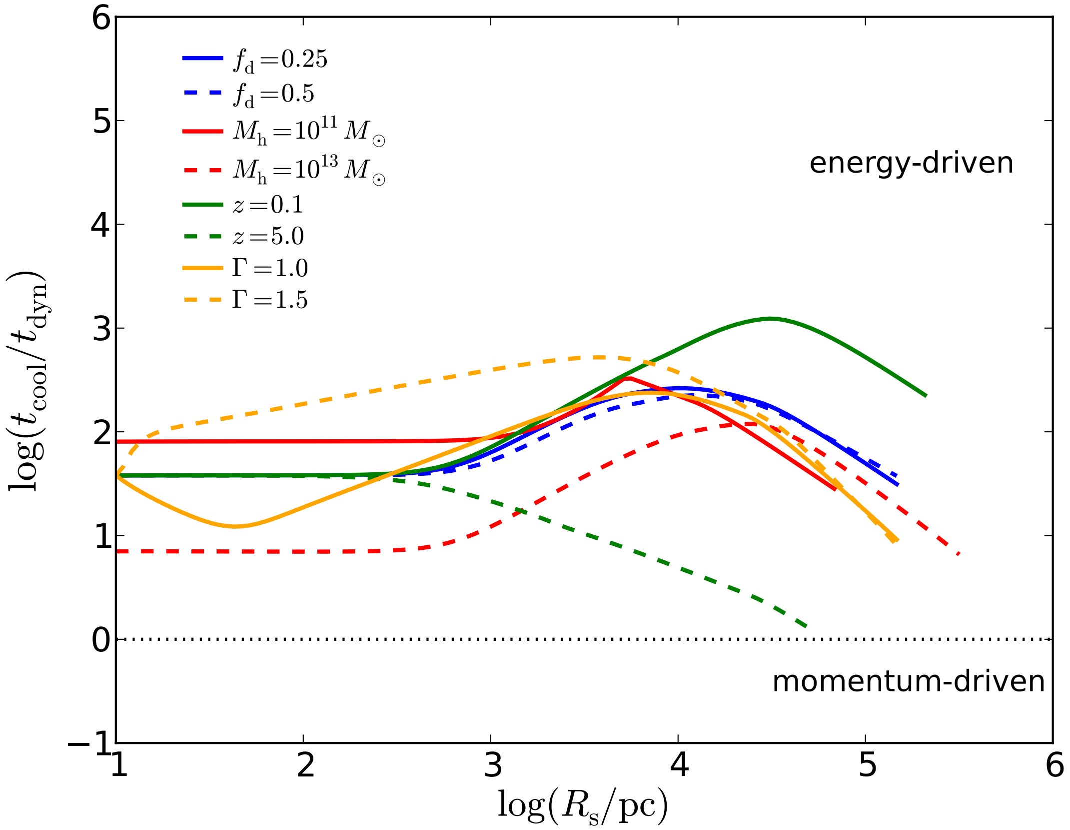

Figure 2.7 Ratio of radiative cooling timescale in the shocked wind region to outflow's dynamical time. The default values of the parameters are: $f_d = 0.25$, $M_h = 10^{12} M_\odot$ and $z = 1.0$. Each line represents a specific parameter modified from its default value while the other parameters are fixed at the default values. The dotted line separates the momentum and energy conserving regimes.

2.6 Conclusions and Discussion

We study the hydrodynamics of AGN-driven outflows out to galactic halo scales and the resulting non-thermal emission from the fast forward outflow shock propagating into the ambient medium. We have found that the outflow decelerates rapidly to a nearly constant velocity of $\sim 10^3\,\mathrm{km\,s^{-1}}$ within the galaxy disk and accelerates once it enters the halo until the central BH shuts off. Around this time, the outflow can reach the edge of the halo. We have verified that the outflow is energy-conserving on large radii, consistently with recent observations (Tombesi et al. 2015) and theoretical calculations (Faucher-Giguère & Quataert 2012; Zubovas & King 2012). The predicted non-thermal emission from outflow shocks in MW mass halos up to a redshift z of 5 is detectable over a broad range of wavelengths. At $z \sim 0.1$, the $2'$ angular scale emission is detectable by *JVLA* and *SKA* in radio band, *ALMA* in mm/sub-mm band, *JWST* and *HST* in optical and infrared bands, marginally detectable in X-ray band by *Chandra*, *XMM-Newton* and *ATHENA*. At $z \sim 1$, the signal remains observable in radio band and marginally detectable in infrared and optical bands with an angular scale of $\sim 18''$. The detection is promising even at high redshifts ($z \sim 5$) in the radio, infrared and optical bands with an angular scale of $\sim 8''$. For lower mass halos the detection should limit within the local Universe.

We find that the detailed gas distributions do not significantly affect the hydrodynamics of the outflow while the halo mass plays a more important role in regulating the outflow dynamics. We show a near universality of the non-thermal emission within the galaxy disk for different gas distributions of galaxies with same halo masses, which breaks down on the halo scale as a result of distinct density profile for tenuous halo gas. The halo mass determines the intensity of the emission since the BH mass is scaled self-consistently with halo mass. Consequently, non-thermal emission from outflows embedded in low mass halos is $\sim 1-3$ orders of magnitude fainter than that in MW mass halos. We conclude that the halo mass is the dominant factor in regulating the dynamics and emission of the outflow. In order to distinguish between different gas density distributions, halo scale observations are required.

The predicted emission should be an observational signature of the existence of extended gas in galaxy halos in a wide range of redshifts. With this method, one can probe the evolution of gaseous halos at early cosmic times. Thermal X-ray emission from free-free cooling at the forward wind shock was proposed to be an observational signature of kpc-scale outflows powered by AGN (Nims et al. 2015). The predicted thermal X-ray luminosity at the 1 keV band is smaller than our non-thermal X-ray prediction and diminishes with increasing outflow shock radius given our assumption about the gas density profile in the galaxy and halo. Since the travel time of the outflow shocks is comparable to AGN's lifetime, most of the detected halos still host an active quasar, targets can be selected for observations as an AGN. On the other hand, subtraction of the much brighter emission from the AGN is required to measure the extended diffuse emission from the outflow shocks. Radio interferometry can resolve the luminous central source and subtract emission from it to obtain the extended emission on halo scale. For optical and infrared observations, the extended emission can be subtracted using techniques similar to the removal of quasar light in *HST* images (McLeod & Rieke 1995; Bahcall et al. 1997).

A source of contamination to the extended non-thermal emission is the scattered quasar light by the surrounding electrons in the halo (Wise & Sarazin 1990; Young

2000; Holder & Loeb 2004). We find that the optical depth for Thomson scattering through the halo is $\sim 10^{-5}$, so $\sim 10^{-5}$ of the observed flux from the AGN is expected to diffuse throughout the halo. For a $10^{12}\, M_{\odot}$ mass halo, the bolometric luminosity of the scattered radiation is $\sim 10^{40}\,\mathrm{erg\,s^{-1}}$, which is comparable to the non-thermal emission at infrared and optical frequencies from outflow shocks in halos within $z \lesssim 1$ and negligible for halos at $z \sim 5$. One possible way to distinguish the scattered radiation from the non-thermal emission is by polarimetric measurement. Additionally, the scattered light is diffused throughout the halo at any given time while the emission from outflow shocks shows a discontinuity at the shock front. As the outflow propagates farther into the halo, the scattered quasar light no longer exists as the quasar fades away. There is no contamination from scattered AGN photons in radio band from radio-quiet quasars, which takes up $\sim 90\%$ of the population, so the non-thermal emission can be more easily identified in radio wavelength (Nims et al. 2015). Therefore, radio observation is expected to be most effective in detecting the halo scale non-thermal emission from outflows in a wide range of redshifts. It should be noted that the predicted radio emission from outflow shocks exists without the presence of relativistic jets, which account for the radio emission from radio galaxies (Heckman & Best 2014).

There are a few uncertainties in our model. First, spherical symmetry of both gas distribution and outflow shell is likely to be unrealistic. In fact, the outflow may be collimated from the start or can propagate along the path of least resistance, forming a bipolar or bicone structure. Observations of kpc-scale molecular outflows suggest a wide-angle biconical geometry (Rupke & Veilleux 2011; Feruglio et al. 2015). Biconical outflows with small opening angle could have less impact on the ambient medium. Second, the detailed gas distribution is uncertain and can be complicated by galaxy-to-galaxy variations, which can greatly depend on galaxy types as well as the specific gas phase. Finally, we find that the terminal velocity of the outflow arriving at the edge of the halo is $\sim 10^3\,\mathrm{km\,s^{-1}}$, which is still large enough for farther propagation of the outflow into the IGM. The propagation dynamics of the outflow into the IGM is beyond the scope of this work. Along some directions gas accretion onto the galaxy could impede the developing outflow (Suresh et al. 2015).

Acknowledgments

We thank Mark Reid and Lorenzo Sironi for helpful comments on the manuscript. This work was supported in part by NSF grant AST-1312034.

Chapter 3

Contribution of Quasar-Driven Outflows to the Extragalactic Gamma-Ray Background

This thesis chapter originally appeared in the literature as

X. Wang & A. Loeb, Contribution of Quasar-Driven Outflows to the Extragalactic Gamma-Ray Background, *Nature Physics*, 12, 12, 1116-1118 (2016)

It is presented here with minor modifications.

Abstract

The origin of the extragalactic γ-ray background permeating throughout the Universe remains a mystery forty years after its discovery (Kraushaar et al. 1972). The

extrapolated population of blazars can account for only half of the background radiation at the energy range of ∼0.1-10 GeV (Ackermann et al. 2015b; Ajello et al. 2015). Here we show that quasar-driven outflows generate relativistic protons that produce the missing component of the extragalactic γ-ray background and naturally match its spectral fingerprint, with a generic break above ~ 1 GeV. The associated γ-ray sources are too faint to be detected individually, explaining why they had not been identified so far. However, future radio observations may image their shock fronts directly. Our best fit to the *Fermi*-LAT observations of extragalactic γ-ray background spectrum provides constraints on the outflow parameters that agree with observations of these outflows (Fabian 2012; Tombesi et al. 2015) and theoretical predictions (Zubovas & King 2012; King & Pounds 2015). Although our model explains the data, there might be additional contributing sources.

3.1 Introduction

The components of the extragalactic γ-ray background (EGB) has been a puzzle since its discovery four decades ago (Fornasa & Sánchez-Conde 2015). Recently, the Large Area Telescope (LAT) on *Fermi* provided fifty-month measurement of the integrated emission from γ-ray sources, with photon energy extending from 0.1 to 820 GeV (Ackermann et al. 2015b). The latest analysis of *Fermi*-LAT data implies that both resolved and unresolved blazars account for $\sim 50^{+12}_{-11}\%$ of the EGB at energy range of $0.1 - 10$ GeV, leaving the origin of the remaining component in question (Ajello et al. 2015).

Active galactic nuclei (AGN) are observed to exhibit strong outflows with velocities of $\sim 0.1\,c$, as manifested by broad absorption lines (Arav et al. 2013)' (Tombesi et al.

2015). The ratio between the input kinetic luminosity of the outflows $L_{\rm in}$ and the bolometric luminosity of quasars $L_{\rm bol}$, $f_{\rm kin}$, is observationally inferred to be $f_{\rm kin} \sim 1-5\%$ (Fabian 2012; Tombesi et al. 2015). The shock wave produced by the interaction of a quasar-driven outflow with the surrounding interstellar medium is expected to accelerate protons to relativistic energies, similarly to the shocks surrounding supernova (SN) remnants where observations of γ-ray emission due to decay of neutral pion (π^0) indicate relativistic proton-proton (pp) collisions via $pp \rightarrow \pi^0 \rightarrow 2\gamma$ (Ackermann et al. 2013). Here, we calculate the analogous γ-ray emission from quasar-driven outflows.

This chapter is organized as follows. In §3.2, we calculate the γ-ray spectrum from quasar-driven outflows. In §3.3, we estimate the contribution of quasar outflows to the EGB. In §3.4, we investigate the contribution of radio galaxies to the EGB. In §3.5, we summarize our results and discuss their implications.

3.2 Gamma-Ray Emission from Quasar Outflows

The energy distribution of accelerated protons per unit volume can be written as $N(E_{\rm p}) = N_0\, E_{\rm p}^{-\Gamma_{\rm p}}$, where $E_{\rm p}$ is the proton energy, and N_0 is a normalization constant, and the power-law idex $\Gamma_{\rm p} \sim 2-3$, based on theoretical models (Caprioli 2012) and observations of shocks around SN remnants (Ackermann et al. 2013)' (Ackermann et al. 2015a). We adopt a fiducial value of $\Gamma_{\rm p} \sim 2.7$ and show that our results are not very sensitive to variations around it (see *Appendix* for details). N_0 can be constrained by the total energy condition $\epsilon_{\rm nt}\epsilon_{\rm th} = \int_{E_{\rm min}}^{E_{\rm max}} N(E_{\rm p}) E_{\rm p}\, dE_{\rm p}$, where $\epsilon_{\rm th}$ is the thermal energy density of the shocked particles and $\epsilon_{\rm nt} \sim 10\%$ is the fraction of the shock kinetic energy converted to accelerate protons (Caprioli & Spitkovsky 2014b). The minimum energy of the accelerated protons, $E_{\rm min}$ is set to be the order of proton rest energy $m_{\rm p}c^2$ and their maximum energy is obtained by equating the acceleration time of protons, $t_{\rm acc}$, to either time scale of pp collision, $t_{pp} \sim (n_{\rm p}\sigma_{pp}c)^{-1}$, or the dynamical time scale of the outflow shock $t_{\rm dyn} \sim R_{\rm s}/v_{\rm s}$. The e-folding time to accelerate protons to relativistic energies is $t_{\rm acc} \sim E_{\rm p}c/eBv_{\rm s}^2$, where e is the electron charge and B is the magnetic field strength (Blandford & Eichler 1987). We assume a fraction of the post shock thermal energy, $\xi_{\rm B}$, is carried by the magnetic field and adopt $\xi_{\rm B} \sim 0.1$, in analogy with SN remnants (Chevalier 1998). Here, $n_{\rm p}$ is proton number density, σ_{pp} is the inelastic cross section of pp collision, $R_{\rm s}$ and $v_{\rm s}$ are the radius and velocity of the outflowing shell, which can be obtained by solving the hydrodynamics of outflows (Wang & Loeb 2015) (see chapter 2 for details).

We compute the spectral energy distribution (SED) of gamma-ray emission produced by neutral pion (π^0) decay. For $E_{\rm p} \lesssim 0.1$ TeV, the γ-ray luminosity is given by (Aharonian & Atoyan 2000):

$$L(E_{\rm g}) = 2VE_{\rm g}^2 \int_{E_{\rm min}}^{\infty} \frac{q_\pi(E_\pi)}{\sqrt{E_\pi^2 - m_\pi^2c^4}}\, dE_\pi \ , \tag{3.1}$$

where $E_{\rm min} = E_{\rm g} + m_\pi^2c^4/4E_{\rm g}$, m_π and E_π are the mass and energy of π^0 and V is the volume of the outflow. $q_\pi(E_\pi)$ is the emissivity of π^0, given by (Aharonian & Atoyan 2000):

$$q_\pi(E_\pi) = \frac{cn_{\rm g}}{\kappa_{pp}}\sigma_{pp}(x)N(x) \ , \tag{3.2}$$

where $x = m_{\rm p}c^2 + E_\pi/\kappa_{pp}$, $\kappa_{pp} \sim 17\%$ is the fraction of the relativistic proton energy that goes to neutral pions in each interaction, $N(x)$ is the energy distribution of accelerated protons and $n_{\rm g} = \rho_{\rm g}/m_{\rm p}$ is the number density of the ambient medium. The inelastic cross section of pp collision σ_{pp} is approximated by (Aharonian & Atoyan 2000):

$$\sigma_{pp}(E_{\rm p}) \approx 30\,[0.95 + 0.06\ln(E_{\rm kin}/{\rm GeV})]\ {\rm mb}\ , \tag{3.3}$$

for $E_{\rm kin} \geq 1$ GeV, and $\sigma_{pp} = 0$ is assumed at lower energies, where $E_{\rm kin} = E_{\rm p} - m_{\rm p}c^2$ is the kinetic energy of protons. This implies that the γ-ray emission is produced by relativistic protons with energy $\gtrsim 2$ GeV. We have verified that the variation in results adopting other approximations of σ_{pp} is negligible (Kelner et al. 2006). We estimate that the timescale of Coulomb collisions (Sturner et al. 1997) is ~ 10 times longer than t_{pp}, meaning that pp collisions is the dominant proton cooling process. The γ-ray SED of an individual quasar outflow for different power-law indices of accelerated protons $\Gamma_{\rm p}$ is shown in Fig.3.1. For a quasar with halo mass $\sim 10^{12}\,M_\odot$ at redshift $z \sim 0.1$, the expected GeV γ-ray luminosity is $\sim 10^{39} - 10^{40}\,{\rm erg\,s^{-1}}$, which falls off the detection limit of *Fermi*-LAT by $\sim 2-3$ orders of magnitude.

3.3 Integrated γ-ray Background

The contribution from quasar outflows to the EGB can be estimated by summing the γ-ray emission over the known quasar population of all bolometric luminosity at all redshifts. The cumulative specific intensity is given by:

$$I(E_{\rm g}) = \iint \Phi(L_{\rm bol}, z)\frac{\overline{L}_\gamma\left(E'_{\rm g}, L_{\rm bol}, z\right)}{4\pi D_{\rm L}^2(z)}\exp\left[-\tau_{\gamma\gamma}(E'_{\rm g}, z)\right]\frac{dV}{dzd\Omega}\,d\log L_{\rm bol}\,dz\ , \tag{3.4}$$

where $E'_{\rm g} = E_{\rm g}(1+z)$ is the intrinsic photon energy, $\Phi(L_{\rm bol}, z)$ is the quasar bolometric luminosity function (Hopkins et al. 2007) and $D_{\rm L}(z)$ is the luminosity distance to redshift z. $\overline{L}_\gamma\left(E_{\rm g}, L_{\rm bol}, z\right) = t_{\rm Sal}^{-1}\int L_\gamma\left(E_{\rm g}, \tau, L_{\rm bol}, z\right)\,d\tau$ is the time-averaged γ-ray luminosity of an individual quasar outflow, where $t_{\rm Sal} \sim 4\times 10^7$ yrs is the Salpeter time for a radiative

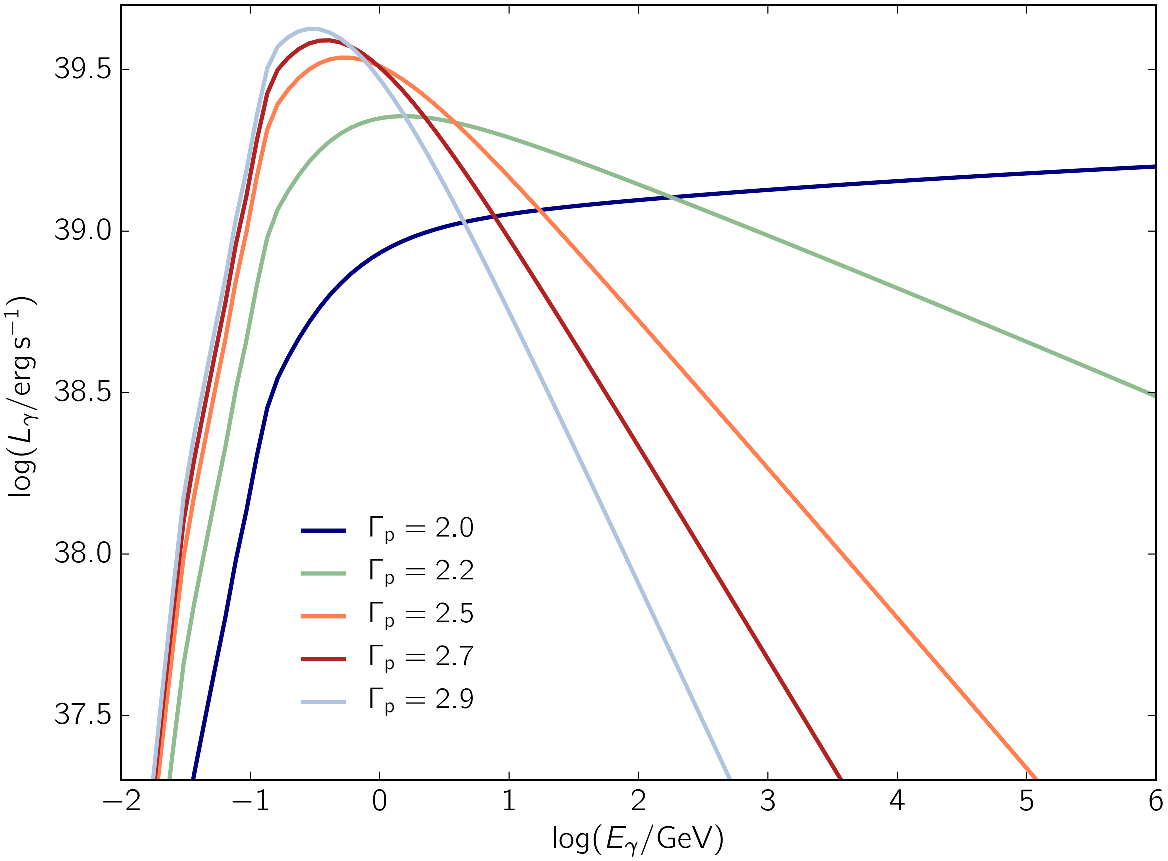

Figure 3.1 Spectral energy distribution of an individual quasar outflow embedded in a halo mass of $10^{12}\,M_\odot$ at redshift 0.1. The lines correspond to power-law indices of accelerated protons $\Gamma_\mathrm{p} = 2.0$, 2.2, 2.5, 2.7 and 2.9, respectively.

efficiency of 10% (Yu & Tremaine 2002). Here, the bolometric luminosity function of quasars is given by (Hopkins et al. 2007):

$$\Phi(L_{\rm bol}, z) = \frac{\Phi_\star}{(L_{\rm bol}/L_\star)^{\gamma_1} + (L_{\rm bol}/L_\star)^{\gamma_2}}; , \tag{3.5}$$

where $L_{\rm bol}$ is the bolometric luminosity, $L_\star$ varies with redshift, described by $\log L_\star = (\log L_\star)_0 + k_{L,1}\xi + k_{L,2}\xi^2 + k_{L,3}\xi^3$, $\xi = \log[(1+z)/(1+z_{\rm ref})]$, $z_{\rm ref} = 2$ and $k_{L,1}$, $k_{L,2}$ and $k_{L,3}$ are free parameters. We adopt parameter values of the pure luminosity evolution model, where $\log(\Phi_\star/{\rm Mpc}^{-3}) = -4.733$, $(\log(L_\star/L_\odot))_0 = 12.965$, $L_\odot = 3.9 \times 10^{33}\,{\rm erg\,s^{-1}}$, $k_{L,1} = 0.749$, $k_{L,2} = -8.03$, $k_{L,3} = -4.40$, $\gamma_1 = 0.517$ and $\gamma_2 = 2.096$. We integrate the γ-ray emission over bolometric luminosity range $10^{42} - 10^{48}\,{\rm erg\,s^{-1}}$ and redshift range $0 - 5$. The comoving volume per unit redshift is given by (Carroll et al. 1992):

$$\frac{dV}{dzd\Omega} = D_{\rm H}\frac{D_{\rm L}^2(z)}{(1+z)^2E(z)} , \tag{3.6}$$

where $D_{\rm H} = c/H_0$ and $E(z) = \sqrt{\Omega_{\rm M}(1+z)^3 + \Omega_\Lambda}$. We adopt $H_0 = 70\,{\rm km\,s^{-1}\,Mpc^{-1}}$, $\Omega_{\rm M} = 0.30$ and $\Omega_\Lambda = 0.7$.

The diffuse extragalactic background light (EBL) associated with the cumulative UV-optical-infrared emission by star-forming galaxies and AGN over the wavelength range of $0.1 - 10^3\,\mu$m, attenuates high-energy photons via e^+e^- pair production. The high energy γ-ray spectrum is therefore attenuated by photon-photon scattering on the EBL, through a factor of $\exp(-\tau_{\gamma\gamma})$, where $\tau_{\gamma\gamma}(E_{\rm g}, z)$ is the EBL optical depth (Stecker et al. 2007) for photons with energy $E_{\rm g}$ at redshift of z.

Figure 3.2 shows the cumulative γ-ray emission from quasar-driven outflows. We set upper and lower limits on the contribution from radio galaxies to the EGB based on the most recent *Fermi*-LAT catalog (3FGL) (Ackermann et al. 2015c) and find that radio galaxies can account for $\sim 7 \pm 4\%$ of the EGB at $E_{\mathrm{g}} \lesssim 10$ GeV, roughly $2-5$ times less than previous estimate based on sources identified in the first and second *Fermi*-LAT catalog (1FGL (Inoue 2011) & 2FGL (Di Mauro et al. 2014)). The insufficient knowledge of the γ-ray emission's origin and core variability of radio galaxies lead to uncertainties in the estimation of their contribution to the EGB as discussed the in following section. Star-forming galaxies has been evaluated to constitute $\sim 13 \pm 9\%$ of the EGB (Ackermann et al. 2012). We show that the contribution from quasar outflows takes up the remaining $\sim 20-40\%$ of the EGB, which dominates over the total of radio galaxies and star-forming galaxies, and can naturally account for the amplitude and spectral shape of the remaining EGB, while at higher energies the EGB is dominated by blazars (Ajello et al. 2015). We have verified that the cumulative contribution from radio galaxies and star-forming galaxies does not match the EGB's spectral shape in that the EGB would be overproduced at $E_{\mathrm{g}} \gtrsim 10$ GeV if the sum of radio galaxies and star-forming galaxies makes up the missing component at $E_{\mathrm{g}} \lesssim 10$ GeV. We find that the break in the spectral energy distribution (SED) of quasar outflows at $\lesssim 10$ GeV is independent of the parameter choices for the outflow dynamics. This generic cutoff in the emission spectrum of quasar outflows naturally fits the missing EGB component.

The fraction of the shock kinetic energy used to accelerate protons ϵ_{nt} and the fraction of the quasar's bolometric luminosity that powers the outflow f_{kin} are free parameters whose product $\eta = \epsilon_{\mathrm{nt}} f_{\mathrm{kin}}$ can be constrained by the EGB data. We search the minimum of $\chi^2 = \sum_{i=1}^{N} \left(I_{\mathrm{obs}}^{i} - I_{\mathrm{mod}}^{i}\right)^2 / \Delta_i^2$ throughout the parameter space, where N is the number of data points, Δ_i is the error bar of the i^{th} observed point and I_{obs}^{i} and I_{mod}^{i} are the EBG intensity of the observed and expected values, respectively. We find the best fit value of $\eta = (3.98 \pm 0.76) \times 10^{-3}$ at 90% significance. For $\epsilon_{\mathrm{nt}} \sim 10\%$

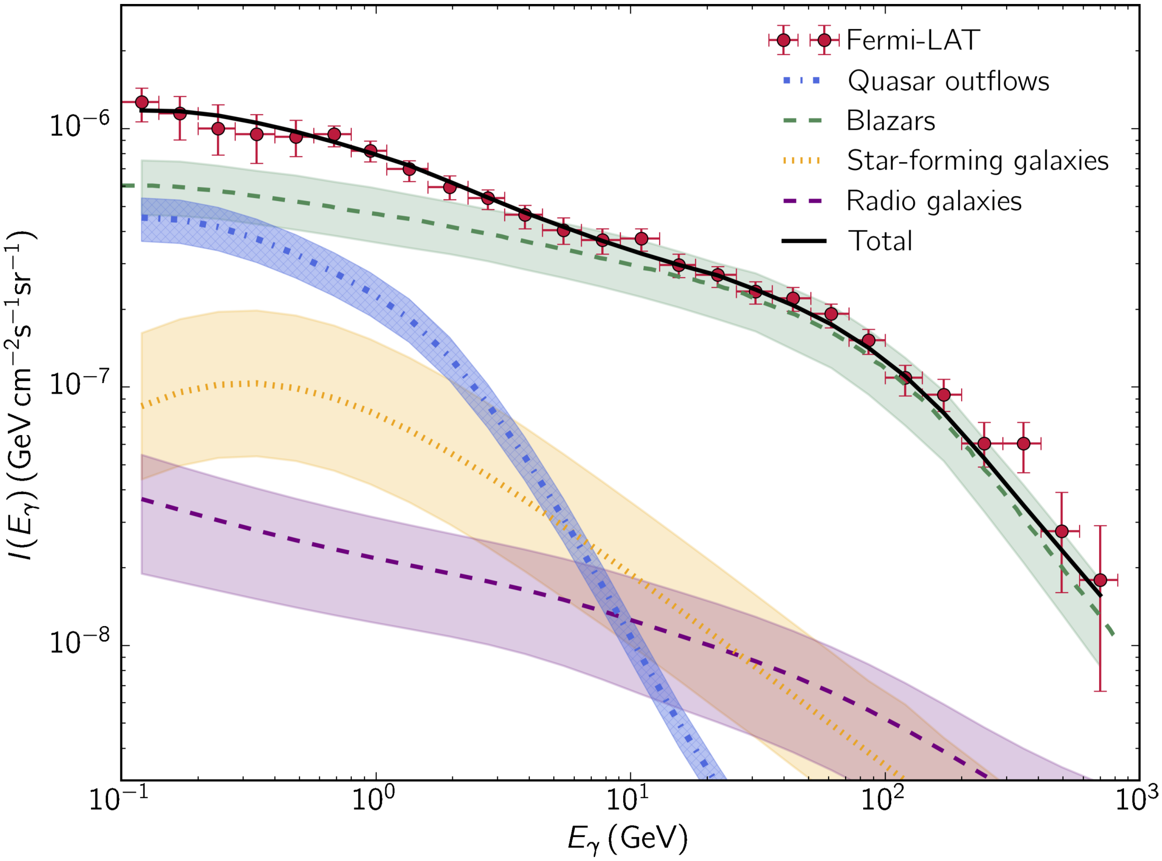

Figure 3.2 Spectral energy distribution of the integrated γ-ray background. *Fermi*-LAT data of the extragalactic γ-ray background is shown as the red points with error bars taken from Ackermann et al. (2015b). The green dashed line corresponds to the contribution from blazars as estimated by Ajello et al. (2015). The purple dashed line shows the contribution from radio galaxies, following Inoue (2011) and Di Mauro et al. (2014), derived from the most recent sample in *Fermi*-LAT catalog (Ackermann et al. 2015c). The orange dotted line corresponds to the contribution from star-forming galaxies as estimated by Ackermann et al. (2012), assuming γ-ray emission spectral shape follows that of the MW. The dot-dashed blue line represents the contribution from our quasar-driven outflow model with $\eta_{-3} = 3.98$, where $\eta_{-3} = (\eta/10^{-3})$. The total contribution to EGB from all sources is shown as the solid black line. The shaded regions indicate the uncertainties of each component.

as inferred from observations of SN remnants (Ackermann et al. 2013) and theoretical models (Caprioli 2012; Caprioli & Spitkovsky 2014b), we deduce a value of $f_{\rm kin} \sim 1-5\%$, which agrees well with observations of outflows (Arav et al. 2013; Tombesi et al. 2015) and theoretical predictions (Zubovas & King 2012; King & Pounds 2015).

3.4 Constraints on Radio Galaxies' Contribution to the EGB

We estimate the contribution to the EGB by radio galaxies (RGs) using samples identified in the most recent *Fermi*-LAT catalog, 3FGL (Ackermann et al. 2015c). Compared with previous *Fermi*-LAT catalogues, PKS 0943-76 has been removed due to misassociation (Ackermann et al. 2015c). The association of Fornax A (NGC 1316) has not been confirmed by 3FGL (Ackermann et al. 2015c). Newly identified FRI (Fanaroff-Riley type I) sources include 4C+39.12 and 3C 264, and FRII sources include 3C 303, 3C 286 and 3C 275.1. Consequently, 19 objects constitute our RG sample and their parameters are summarized in Table 3.1.

We note that some FRI sources such as IC 310, PKS 0625-35 and NGC 1275 show blazar-like variabilities, which could lead to debatable source classification with BL Lac objects. TXS 0348+013, 3C 207, 3C 275.1, 3C 286 and 3C 380 are classified as steep-spectrum radio quasars (SSRQs) and thus are non-standard FRIIs (Di Mauro et al. 2014). However, FRI/BLL and SSRQ sources are also included in sample selection of Inoue (2011) and Di Mauro et al. (2014). Therefore, we keep them in our source selection in consistency with previous analysis and we have verified that removal of them lead to negligible change in radio-γ-ray correlation as discussed later.

Previously, the contribution of RGs to the EGB has been evaluated based on the γ-ray luminosity function of RGs, which is established from a correlation between γ-ray and 5 GHz *core-only* radio luminosities of RGs (Inoue 2011). However, the origin of the γ-ray emission from RGs remains uncertain. γ-ray emission could be produced by ultrarelativistic electrons of high density in the radio lobes by scattering soft photons via self-synchrotron Compton or external Compton processes. Such γ-ray emission has been resolved and confirmed in the lobes of a nearby FRI RG, Cen A by *Fermi*-LAT (Abdo et al. 2010a). Due to the lack of simultaneous radio and γ-ray observations of RGs, core variabilities could invalidate this correlation. In our calculation below, we choose radio data closest in date to γ-ray observations. The correlation between the *core-only* radio luminosity and the total γ-ray luminosity would be distorted if some of the unresolved γ-ray emission originates outside the core of the corresponding galaxies. In such a case, the γ-ray emission from the core would be overestimated, and the radio-γ-ray correlation would provide an upper limit on the contribution of RGs to the EGB. The actual contribution would be between this upper limit and the result one gets when correlating the *total* radio and γ-ray emission of these galaxies.

We recalculate the L_γ-$L_{\rm rad}$ correlation for both *core-only* and *total* radio luminosity cases using the most recent samples. We follow the BCES (bivariate correlated errors and intrinsic scatter) method by Akritas & Bershady (1996) to fit regression parameters and uncertainties. Using the BCES($L_\gamma \mid L_{\rm rad}$) slope estimator, we find that the best fit L_γ-$L_{\rm rad}^{\rm tot}$ and $f_{\rm g}$-$F_{\rm rad}^{\rm tot}$ correlation can be expressed as:

$$\log(L_{\gamma,40}) = (0.972 \pm 0.087)\log(L_{\rm rad,40}^{\rm tot}) + (1.944 \pm 0.233)\,, \tag{3.7a}$$

$$\log(f_{\rm g}) = (0.682 \pm 0.185) \log(F^{\rm tot}_{\rm rad}) + (-11.330 \pm 0.141) \ , \tag{3.7b}$$

where $L_{\gamma,40}$ and $L^{\rm tot}_{\rm rad,40}$ are L_γ and total radio luminosity $L^{\rm tot}_{\rm rad}$ in units of $10^{40}\,{\rm erg\,s^{-1}}$. Similarly, the best fit L_γ-$L^{\rm core}_{\rm rad}$ and $f_{\rm g}$-$F^{\rm core}_{\rm rad}$ are given by:

$$\log(L_{\gamma,40}) = (0.934 \pm 0.073) \log(L^{\rm core}_{\rm rad,40}) + (2.582 \pm 0.103) \,, \tag{3.8a}$$

$$\log(f_{\rm g}) = (0.790 \pm 0.183) \log(F^{\rm core}_{\rm rad}) + (-10.910 \pm 0.106) \ , \tag{3.8b}$$

where $L^{\rm core}_{\rm rad}$ is the core-only radio luminosity in units of $10^{40}\,{\rm erg\,s^{-1}}$. γ-ray-radio correlations based on 1FGL (Inoue 2011) and 2FGL (Di Mauro et al. 2014) samples are given by:

$$\log(L_{\gamma,40}) = (1.16 \pm 0.02) \log(L^{\rm core}_{\rm rad,40}) + (2.5 \pm 1.41) \,, \tag{3.9}$$

$$\log(L_{\gamma,40}) = (1.008 \pm 0.025) \log(L^{\rm core}_{\rm rad,40}) + (2.32 \pm 1.98) \,. \tag{3.10}$$

We compare our fitted L_γ-$L^{\rm tot}_{\rm rad}$ and L_γ-$L^{\rm core}_{\rm rad}$ correlation with previous results, shown in Fig.3.3 and Fig.3.4, respectively. We calculate the corresponding Spearman coefficients and partial correlation coefficient of L_γ and $L_{\rm rad}$, $f_{\rm g}$ and $F_{\rm rad}$ and the corresponding p-values, summarized in Table 3.2.

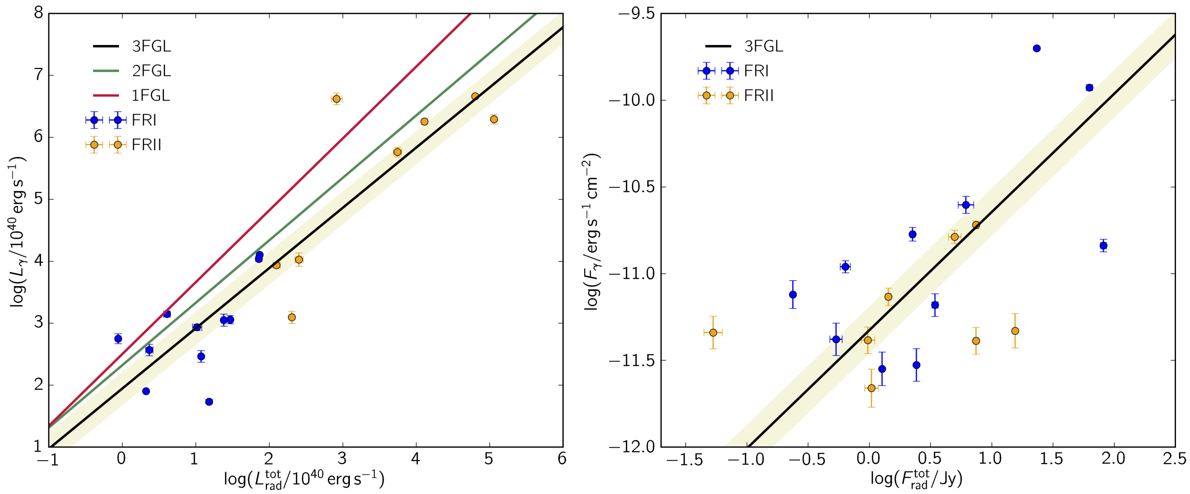

Figure 3.3 Correlation between γ-ray luminosity/flux above 100 MeV and *total* radio luminosity/flux at 5 GHz of RGs. The blue and orange points with error bars represent FRI and FRII type RGs selected from *Fermi*-LAT third catalog (3FGL) (Ackermann et al. 2015c). On the left panel, the red and blue lines show the L_γ-$L_{\mathrm{rad}}^{\mathrm{core}}$ correlation fitted by Inoue (2011) based on 1FGL and Di Mauro et al. (2014) based on 2FGL used to evaluate the γ-ray luminosity function of RGs, respectively, while the black lines represent the fit using samples from the third *Fermi*-LAT catalog (3FGL) (Ackermann et al. 2015c), using BCES sampler (Akritas & Bershady 1996). On the right panel, we show the correlation between radio and γ-ray fluxes using the same linear regression sampler. The shaded beige bands indicate 1σ uncertainty.

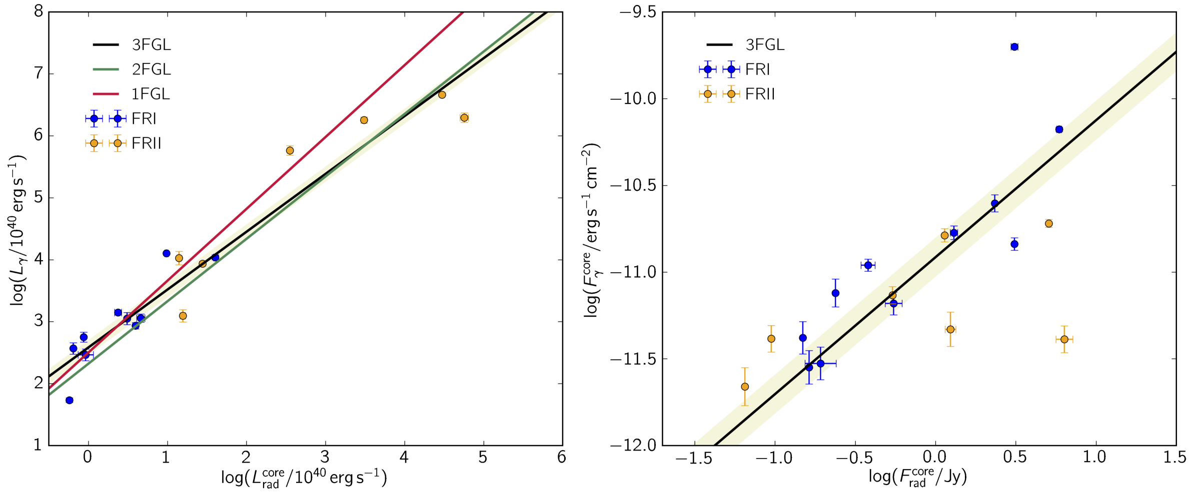

Figure 3.4 Correlation between γ-ray luminosity/flux above 100 MeV and *core-only* radio luminosity/flux at 5 GHz of RGs. Legends are the same as Fig.3.3.

Table 3.1 Parameters of radio galaxies in 3FGL.

Object name	3FGL name	z	S_γ $(10^{-9}\,\mathrm{ph\,cm^{-2}\,s^{-1}})$	F_γ $(10^{-12}\,\mathrm{erg\,s^{-1}\,cm^{-2}})$	Γ	$F_{\mathrm{rad}}^{\mathrm{core}}$ (Jy)	$F_{\mathrm{rad}}^{\mathrm{tot}}$ (Jy)	α	Type	Ref
NGC 1218	J0308.6+0408	0.029	7.10 ± 2.13	6.59 ± 1.07	2.07 ± 0.11	0.548 ± 0.07	3.44 ± 0.20	0.64	FRI	1,2
IC 310	J0316.6+4119	0.019	5.63 ± 2.39	7.58 ± 1.55	1.90 ± 0.14	0.238 ± 0.004	0.238 ± 0.004	0.75	FRI†	3
NGC 1275	J0319.8+4130	0.018	256.51 ± 4.84	199.05 ± 3.93	2.08	3.10 ± 0.16	23.3	0.78	FRI	4,5
4C+39.12	J0334.2+3915	0.021	5.18 ± 2.39	4.18 ± 1.00	2.11 ± 0.17	0.149	0.535 ± 0.066	0.39	FRI†	5,6
TXS 0348+013	J0351.1+0128	1.120	8.09 ± 4.29	4.57 ± 1.11	2.43 ± 0.18	…[c]	0.053 ± 0.01	…[c]	FRII‡	5
3C 111	J0418.5+3813	0.049	43.17 ± 10.06	16.30 ± 1.50	2.79 ± 0.08	1.14	4.98 ± 0.618	0.73	FR II	5,7
Pictor A	J0519.2-4542	0.035	9.28 ± 4.93	4.68 ± 1.20	2.49 ± 0.18	1.24 ± 0.10	15.5 ± 0.47	1.07	FR II	1,8
PKS 0625-35	J0627.0-3529	0.055	10.54 ± 1.60	16.87 ± 1.59	1.87 ± 0.06	1.30 ± 0.07	2.25 ± 0.09	0.65	FRI†	1,9
NGC 2484	J0758.7+3747	0.043	4.36 ± 2.15	2.82 ± 0.70	2.16 ± 0.16	0.163	1.27 ± 0.02	0.07	FRI	1,7
3C 207	J0840.8+1315	0.681	14.77 ± 4.25	7.35 ± 0.89	2.47 ± 0.09	0.539 ± 0.003	1.43 ± 0.07	0.90	FRII‡	1,10
3C 264	J1145.1+1935	0.022	2.89 ± 1.62	2.97 ± 0.72	1.98 ± 0.20	0.192 ± 0.048	2.43 ± 0.01	0.46	FRI	1,2
M87	J1230.9+1224	0.004	14.36 ± 2.53	14.52 ± 1.27	2.04 ± 0.07	3.10 ± 0.04	81.70 ± 4.28	0.79	FRI	1,11
3C 275.1	J1244.1+1615	0.555	8.09 ± 4.01	4.13 ± 0.80	2.43 ± 0.16	0.095	0.973 ± 0.133	0.96	FRII‡	5,7
3C 286	J1330.5+3023	0.850	7.97 ± 4.95	4.10 ± 0.80	2.60 ± 0.16	6.34 ± 0.82	7.43 ± 0.37	0.88	FRII‡	1, 5
Cen B	J1346.6-6027	0.013	41.88 ± 9.60	24.92 ± 3.00	2.32 ± 0.09	2.34	6.14 ± 0.97	0.13	FRI	12,13
3C 303	J1442.6+5156	0.141	1.65 ± 1.06	2.19 ± 0.63	1.91 ± 0.18	0.065	1.04 ± 0.14	0.95	FR II	5,7
NGC 6251	J1630.6+8232	0.025	21.65 ± 1.67	10.95 ± 0.91	2.22	0.38 ± 0.04	0.637 ± 0.064	0.72	FRI	14,15
3C 380	J1829.6+4844	0.692	35.22 ± 4.00	19.08 ± 1.03	2.37 ± 0.04	5.07 ± 0.105	7.45 ± 0.37	0.71	FRII‡	1,16
Cen A	J1325.4-4301[a]	0.002	170.47 ± 15.46	66.5 ± 2.1	2.70 ± 0.03	5.88 ± 0.21	62.8 ± 0.099	0.70	FRI	8,17
	J1324.0-4330e[b]	" "	115.30 ± 16.71	51.7 ± 4.2	2.53 ± 0.05	…	…	" "	" "	

Note. — Objects are selected from the Clean Sample of Table 5 from Ackermann et al. (2015)[1].
S_γ — γ-ray photon flux above 100 MeV.
F_γ — γ-ray energy flux above 100 MeV.
Γ — Photon index power-law index between 0.1–100 GeV.
$F_{\mathrm{rad}}^{\mathrm{core}}$, $F_{\mathrm{rad}}^{\mathrm{tot}}$ — Core, total radio flux at 5 GHz. The error bars indicate measurement errors.
α — Radio spectral index.
Object type — FRI and FRII: type I and II Fanaroff-Riley galaxy. †‡ Non-standard[3].
References — 1. Kuhr et al. (1981)[5]; 2. Kharb et al. (2009)[6]; 3. Kadler et al. (2012)[7]; 4. Taylor et al. (2006)[8]; 5. Gregory & Condon (1991)[9]; 6. Giovannini et al. (2001)[10]; 7. Laurent-Muehleisen et al. (1997)[11]; 8. Tingay et al. (2003)[12]; 9. Murphy et al. (2010)[13]; 10. Mullin et al. (2006)[14]; 11. Nagar et al. (2001)[15]; 12. Marshall et al. (2005)[16]; 13. Massardi et al. (2008)[17]; 14. Linford et al. (2012)[18]; 15. Evans et al. (2005)[19]; 16. Mantovani et al. (2009)[20]; 17. Wright et al. (1994)[21].

[a,b] Cen A core and lobes, respectively.

[c] No measurement is given.

Following Inoue (2011) and Di Mauro et al. (2014), we calculate RG's contribution to the EGB using our updated γ-ray-radio correlation. The γ-ray luminosity function (GLF) can be obtained by:

$$\rho_\gamma = \kappa \rho_{\rm rad} \frac{d \log L_{\rm rad}}{d \log L_\gamma} \ , \tag{3.11}$$

where $\rho_{\rm rad}$ is the radio luminosity function (RLF) of RGs, and κ is the fraction of γ-ray loud RGs, constraint by source-count distribution as discussed later in the text. For the *total*-radio-γ-ray luminosity correlation, we adopt the total RLF and corresponding parameters given by model C of Willott et al. (2001) and convert it to the cosmological constants in this work. For the *core-only* radio luminosity correlation, we convert the total RLF to core RLF, following the method proposed by Di Mauro et al. (2014), according to the core-total radio luminosity correlation of RGs (Lara et al. 2004):

$$\log L_{\rm rad,core}^{5\,\rm GHz} = (0.77 \pm 0.08) \log L_{\rm rad,tot}^{1.4\,\rm GHz} + (4.2 \pm 2.1) \ , \tag{3.12}$$

where core radio luminosity at 5 GHz $L_{\rm rad,core}^{5\,\rm GHz}$ and total radio luminosity at 1.4 GHz $L_{\rm rad,tot}^{1.4\,\rm GHz}$ are in units of W Hz^{-1}. We adopt a radio spectral index $\alpha_{\rm r} = 0.8$ for conversion of radio luminosities at different frequencies in our calculation (Willott et al. 2001).

Table 3.2. Comparison of correlation coefficients

	L_γ-$L_{\rm rad}$	p-value	L_γ-$L_{\rm rad}(z)$	$f_{\rm g}$-$F_{\rm rad}$	p-value	$f_{\rm g}$-$F_{\rm rad}(z)$
Total	0.863	1.957×10^{-6}	0.680	0.511	0.026	0.547
Core	0.938	8.94×10^{-9}	0.775	0.676	0.002	0.752

Note. — We compare the correlation between γ-ray and *total*, *core-only* radio luminosities and fluxes. p-values are given in columns next to corresponding Spearman coefficients. In the last column, partial coefficients are given to exclude the dependence on redshift z.

The intrinsic γ-ray photon flux per unit energy is obtained by:

$$\frac{dS_\gamma}{dE_\mathrm{g}}(E_\mathrm{g}, L_\gamma, z, \Gamma) = \frac{2-\Gamma}{E_1^2}\left(\frac{E_\mathrm{g}}{E_1}\right)^{-\Gamma}\left[\left(\frac{E_2}{E_1}\right)^{2-\Gamma} - 1\right]^{-1}\frac{L_\gamma(1+z)^{2-\Gamma}}{4\pi D_\mathrm{L}^2(z)} \ , \tag{3.13}$$

where Γ is the γ-ray photon index. Therefore, we obtain the integrated γ-ray SED from RGs, expressed as:

$$\begin{aligned} I(E_\mathrm{g}) =& E_\mathrm{g}^2 \int_{\Gamma_\mathrm{min}}^{\Gamma_\mathrm{max}} \frac{dN_\Gamma}{d\Gamma} d\Gamma \int_{z_\mathrm{min}}^{z_\mathrm{max}} \frac{dV}{dzd\Omega}\, dz \int_{L_{\gamma,\mathrm{min}}}^{L_{\gamma,\mathrm{max}}} d\log L_\gamma \, \rho_\gamma(L_\gamma, z) \\ & \times \frac{dS_\gamma}{dE_\mathrm{g}}\left(E'_\mathrm{g}, z, L_\gamma, \Gamma\right) \exp\left[-\tau_{\gamma\gamma}(E'_\mathrm{g}, z)\right] \left\{1 - \omega\left[S_\gamma(L_\gamma, z)\right]\right\} , \end{aligned} \tag{3.14}$$

where $dN_\Gamma/d\Gamma$ is the distribution of γ-ray photon index Γ, which is assumed to be Gaussian in an analogy to blazars, with an average value of 2.25 and a scatter of 0.28 based on our RG sample. $\omega(S_\gamma)$ is the detection efficiency of *Fermi*-LAT at a photon flux of S_γ. However, $\omega(S_\gamma)$ is not given in 3FGL, so we adopt the derived detection efficiency for detection threshold TS > 25 and $|b| < 10^\circ$ derived for 2FGL (Di Mauro et al. 2014). We adopt $\Gamma_\mathrm{min} = 1.0$, $\Gamma_\mathrm{max} = 5.0$, $z_\mathrm{min} = 0.0$, $z_\mathrm{max} = 5.0$, $L_{\gamma,\mathrm{min}} = 10^{38}\,\mathrm{erg\,s^{-1}}$ and $L_{\gamma,\mathrm{max}} = 10^{50}\,\mathrm{erg\,s^{-1}}$ in our calculation.

The expected cumulative flux distribution can be obtained by:

$$N_\mathrm{exp}(> S_\gamma) = 4\pi \int_{\Gamma_\mathrm{min}}^{\Gamma_\mathrm{max}} \frac{dN_\Gamma}{d\Gamma}\, d\Gamma \int_{z_\mathrm{min}}^{z_\mathrm{max}} \frac{dV}{dzd\Omega}\, dz \int_{L_\gamma(S_\gamma, z)}^{L_{\gamma,\mathrm{max}}} \rho_\gamma(L_\gamma, z)\, d\log L_\gamma \ , \tag{3.15}$$

where S_γ is the photon flux above 0.1 GeV and $L_\gamma(S_\gamma, z)$ is the corresponding γ-ray luminosity at a redshift of z. The observed source-count distribution of our sample is given by (Abdo et al. 2010b):

$$N_\mathrm{obs}(> S_\gamma) = \sum_{i=1}^{N(>S_{\gamma,i})} \frac{1}{\omega(S_{\gamma,i})} \ , \tag{3.16}$$

where we sum up all RG sources with photon flux $S_{\gamma,i} > S_\gamma$. κ can be constraint by normalizing N_exp to N_obs. We find the best fit at 1σ significance is $\kappa = 0.081 \pm 0.008$

by using *total*-radio-γ-ray luminosity correlation (Eq.3.7), and $\kappa = 2.32 \pm 0.15$ by using *core*-radio-γ-ray luminosity correlation (Eq.3.8, 3.12). This indicates that the *core-only* radio-γ-ray correlation overproduces γ-ray loud RGs constraint by the observed source-count distribution. In this case, we fix $\kappa = 1$ in our calculation following Di Mauro et al. (2014).

We obtain the resulting integrated γ-ray spectrum for both cases, which set the upper and lower limits of RG's contribution to the EGB. In our calculation, we adopt the mid-value of this range as RG's contribution and show the full range as uncertainty.

We find that the RGs make up $\sim 7 \pm 4\%$ of the EGB. We have verified that if RGs accounts for the rest of the EGB besides blazars and star-forming galaxies at $E_{\rm g} \lesssim 10$ GeV, then the EGB would be overproduced at higher energies. However, quasar outflow's SED has a generic break at < 10 GeV, which naturally account for the missing component of the EGB.

3.5 Discussion

The bright phase of the γ-ray emission from an individual quasar ends abruptly when the outflow exits from the surrounding galactic disk, as shown in Figure 3.5, making it difficult to detect afterwards. Outflows embedded in Milky Way (MW) mass halos propagating to 10 kpc scale are expected to produce GeV γ-ray emission of $\sim 10^{39} - 10^{40}\,{\rm erg\,s^{-1}}$. In the local Universe ($z < 0.1$), we find that only $\lesssim 0.1\%$ of quasars host γ-ray bright outflows that are detectable by *Fermi*-LAT at GeV energies. These outflows are too faint to be detected in γ-rays individually, explaining why they have not been identified so far. A possible candidate of galactic outflow relic is the Fermi bubbles at the Galactic center (Su et al. 2010), whose γ-ray emission has been explained by hadronic process similar to our model (Crocker & Aharonian 2011; Crocker et al. 2015). Our interpretation can be tested through observations of quasar outflows at other wavelengths. Radio emission is simultaneously produced via synchrotron from accelerated electrons by the same outflow shocks (see black solid line in Fig.3.5). Radio telescopes such as *the Jansky Very Large Array* and *the Square Kilometre Array* provide high sensitivity to detect this emission and confirm the parameters of outflows (Wang & Loeb 2015) at redshifts up to ~ 5. For most AGNs, the radio emission is free of contamination from the central source or scattering of its light by surrounding electrons. Source stacking (Cillis et al. 2004) could be performed in the future to find direct evidence for the cumulative γ-ray signal from multiple outflow-hosting quasars. The calibration of the outflow parameters based on their γ-ray emission can be used to forecast their contribution to the neutrino background through pion production in pp collisions (see chapter 4 for details).

Acknowledgments

We thank Douglas Finkbeiner, James Guillochon and Lorenzo Sironi for helpful comments on the manuscript. We thank Jonathan Grindlay, Vinay Kashyap, Mark Reid, Aneta Siemiginowska and Stephen Portillo for useful discussion. This work is supported by NSF grant AST-1312034.

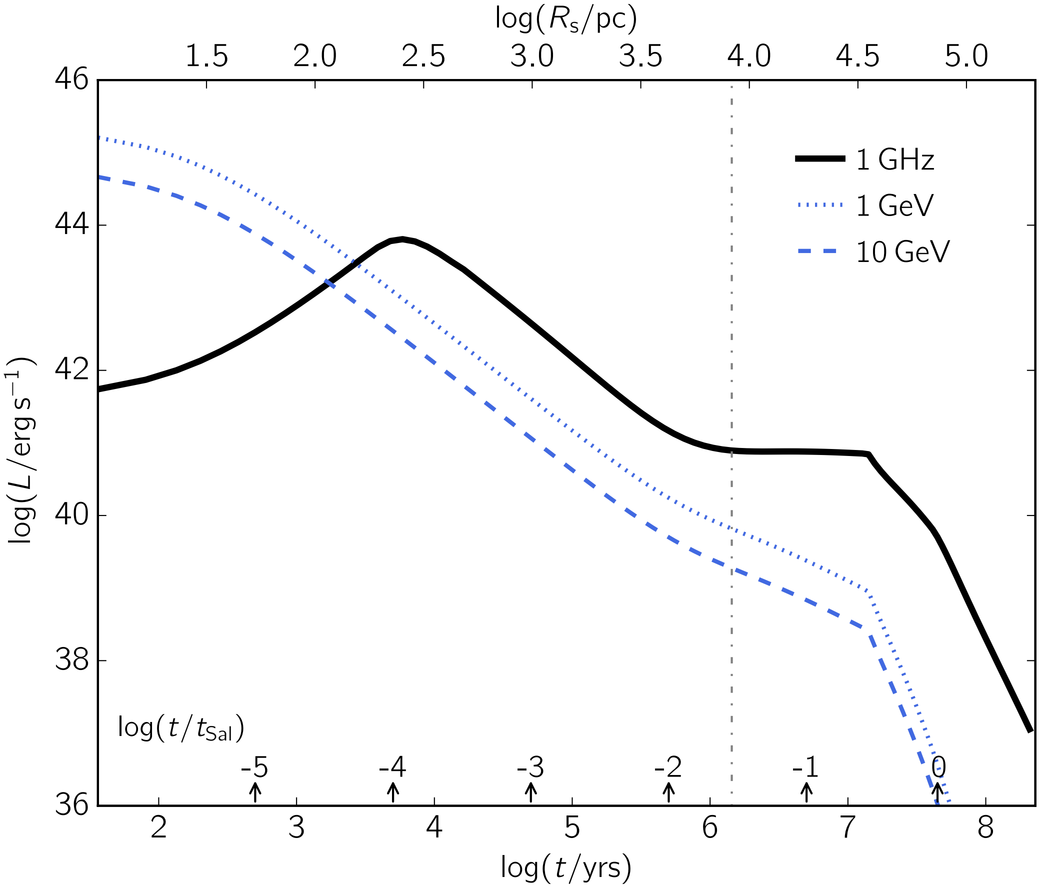

Figure 3.5 Light curve of γ-ray emission from AGN-driven outflows and its radio counterpart, for a halo mass $M_{\rm h} = 10^{12}\, M_\odot$ and redshift $z = 0.1$. The solid black line represents the radio synchrotron emission at 1 GHz from electrons accelerated at the outflow shock front (Wang & Loeb 2015). The dotted and dashed blue lines show the γ-ray emission from accelerated protons with photon energies at 1 GeV and 10 GeV, respectively. The dot-dashed vertical line marks the transition of the outflow from the disk to the halo of its host galaxy. The radio and γ-ray luminosity are shown as a function of time, t, and outflow shock radius, R_s, on the lower and upper horizontal axes, respectively. Above the lower horizontal axis, we express the time as a fraction of the Salpeter time $t_{\rm Sal}$, indicating roughly the probability of finding a quasar at each time or position. The vast majority of the quasar outflows are too faint to be detected individually, explaining why their contribution to the EGB had not been recognized.

Chapter 4

Cumulative Neutrino Background from Quasar-Driven Outflows

This thesis chapter originally appeared in the literature as

X. Wang & A. Loeb, Cumulative Neutrino Background from Quasar-Driven Outflows, *Journal of Cosmology and Astroparticle Physics*, 12, 012 (2016)

Abstract

Quasar-driven outflows naturally account for the missing component of the extragalactic γ-ray background through neutral pion production in interactions between protons accelerated by the forward outflow shock and interstellar protons. We study the simultaneous neutrino emission by the same protons. We adopt outflow parameters that best fit the extragalactic γ-ray background data and derive a cumulative neutrino background of $\sim 10^{-7}\,\mathrm{GeV\,cm^{-2}\,s^{-1}\,sr^{-1}}$ at neutrino energies $E_\nu \gtrsim 10$ TeV, which

naturally explains the most recent IceCube data without tuning any free parameters. The link between the γ-ray and neutrino emission from quasar outflows can be used to constrain the high-energy physics of strong shocks at cosmological distances.

4.1 Introduction

There is currently strong observational evidence for the existence of large-scale outflows driven by the active galactic nuclei (AGN), including the presence of broad absorption lines in quasars (Zakamska & Greene 2014; Arav et al. 2015) and multiphase outflows in nearby ultraluminous infrared galaxies (ULIRGs) (Rupke & Veilleux 2011; Tombesi et al. 2015). Semi-relativistic winds with a speed of $\sim 0.1\,c$ are typically produced by quasars in the surrounding interstellar medium, driving a forward shock that accelerates a swept-up shell accompanied by a reverse shock that decelerates the wind itself (Faucher-Giguère & Quataert 2012; King & Pounds 2015).

In a previous paper, we derived a detailed hydrodynamical model for the quasar outflow's interaction with the ambient medium (Wang & Loeb 2015) (see chapter 2 for details), including a disk and a halo components for the host galaxy gas. The gas density profile was self-consistently determined by the halo mass and redshift. The continuous energy injection was assumed to be a fraction of the quasar's bolometric luminosity $f_{\rm kin} L_{\rm bol}$ during the quasar's lifetime, which is of order the Salpeter time $t_{\rm Sal} \sim 4 \times 10^7$ yrs for a radiative efficiency of 0.1 (Yu & Tremaine 2002). In the upper panel of Fig.4.2, we show the forward shock velocity $v_{\rm s}$ as a function of radius $R_{\rm s}$ for the outflow in a dark matter halo of mass $\sim 10^{12}\,M_\odot$ at a redshift of $z \sim 0.1$. We find that $v_{\rm s} \gtrsim 10^3\,{\rm km\,s^{-1}}$ within the galactic disk with a decline to few hundreds ${\rm km\,s^{-1}}$ when the outflow reaches the edge of the halo. In analogy with supernova (SN) remnants (Caprioli 2012; Ackermann et al. 2013), protons should be accelerated via Fermi acceleration to relativistic energies in the forward outflow shock.

The resulting proton number density per unit volume per unit energy can be expressed as a power-law with an exponential high-energy cutoff:

$$\frac{dN_{\rm p}}{dE_{\rm p}} = N_0 E_{\rm p}^{-\Gamma_{\rm p}} \exp\left(-\frac{E_{\rm p}}{E_{\rm max}}\right) \ , \tag{4.1}$$

where $\Gamma_{\rm p}$ is the power-law index, N_0 is the normalization constant and $E_{\rm max}$ is the maximum energy of the accelerated protons. The value of N_0 can be obtained by setting $\int N_{\rm p}(E_{\rm p})E_{\rm p}dE_{\rm p} = \frac{3}{2}\epsilon_{\rm nt}n_{\rm s}kT_{\rm s}$, where $\epsilon_{\rm nt}$ is the fraction of energy that goes to accelerated protons and $n_{\rm s}$ and $T_{\rm s}$ are the number density and temperature of the shocked medium, respectively. $E_{\rm max}$ can be obtained by equaling the acceleration time scale, $t_{\rm acc}$, and the minimum between the cooling timescale and the dynamical timescale, $t_{\rm dyn} \sim R_{\rm s}/v_{\rm s} \approx 10^6\, R_{\rm s,kpc}v_{\rm s,3}^{-1}$ yrs. We adopt $t_{\rm acc} \sim E_{\rm p}c/eBv_{\rm s}^2 \approx 300\, E_{\rm p,TeV}B_{-6}^{-1}v_{\rm s,3}^{-1}$ yrs, where B is the post-shock magnetic field (Blandford & Eichler 1987). Here $E_{\rm p,TeV} = (E_{\rm p}/{\rm TeV})$, $v_{\rm s,3} = (v_{\rm s}/10^3{\rm km\,s^{-1}})$, $R_{\rm s,kpc} = (R_{\rm s}/{\rm kpc})$ and $B_{-6} = (B/\mu{\rm G})$. We assume that a fraction of the post shock thermal energy is carried by the magnetic field, giving $B = (8\pi\xi_{\rm B}n_{\rm s}kT_{\rm s})^{1/2}$, with a value $\xi_{\rm B} = 0.1$ calibrated based on SN remnants (Chevalier 1998). Protons may lose energy via synchrotron, inverse Compton scattering, hadro-nuclear (pp) or photo-hadronic ($p\gamma$) processes. As discussed later, pp collisions provide the dominant cooling mechanism for protons. The corresponding timescale, t_{pp}, can be written as (Kelner et al. 2006):

$$t_{pp}^{-1} = n_{\rm p}\sigma_{pp}c\kappa_{pp} \ , \tag{4.2}$$

where $\kappa_{pp} \sim 0.5$ is the inelasticity parameter and σ_{pp} is the cross section for pp collisions

(Kelner et al. 2006):

$$\sigma_{pp} = (34.3 + 1.88\ell + 0.25\ell^2) \left[1 - \left(\frac{E_{\rm th}}{E_{\rm p}}\right)^4\right]^2 \ {\rm mb}\ , \tag{4.3}$$

with $\ell = \ln E_{\rm p,TeV}$ and $E_{\rm th} \approx 1.22$ GeV being the threshold energy for pp collisions. For $B_{-6} = 1$, $v_{\rm s,3} = 1$ and $R_{\rm s,kpc} = 1$, we find $E_{\rm max} \sim 10^6$ GeV. The parameters $f_{\rm kin}$ and $\epsilon_{\rm nt}$ and $\Gamma_{\rm p}$ constrain the hadronic emission from quasar outflows.

γ-ray emission is produced via the decay of the neutral pions generated in pp collisions, $\pi^0 \rightarrow 2\gamma$. The detailed calculation of the integrated γ-ray background is discussed in chapter 3. While blazars account for $\sim 50\%$ of the extragalactic γ-ray background (EGB) at $E_{\rm g} \lesssim 10$ GeV and almost all the EGB at higher energies (Ajello et al. 2015), we use parameter values consistent with outflow observations (Tombesi et al. 2015) and find that our model produces γ-ray emission that make up $\sim 30\%$ of the EGB at $E_{\rm g} \lesssim 10$ GeV and matches the required spectral shape of the EGB. The γ-ray emission by quasar outflows dominates over radio galaxies and star-forming galaxies, based on the most recent *Fermi*-LAT data (Ackermann et al. 2015b) and previous studies (Inoue 2011; Ackermann et al. 2012; Di Mauro et al. 2014; Wang & Loeb 2016a). For a given $\Gamma_{\rm p}$, we can fix the free parameters in our model, $f_{\rm kin}\epsilon_{\rm nt}$, by fitting the EGB data. For $\epsilon_{\rm nt} \sim 10\%$, we find that $f_{\rm kin} \sim 3\%$, in agreement with observations of outflows (Tombesi et al. 2015).

4.2 Neutrino Production

Next, we calculate the simultaneous neutrino emission from the same protons, which lose energy via two main channels of pion production: $p + \gamma \rightarrow p + \pi^0$ or $n + \pi^+$ and

$p + p \rightarrow \pi^+ + \pi^- + \pi^0$. In the $p\gamma$ channel, relativistic protons lose energy by interacting with X-ray photons from the hot coronae above the accretion disk. The timescale for $p\gamma$ interactions is given by (Stecker 1968; Murase et al. 2012):

$$\begin{aligned} t_{p\gamma}^{-1} &= \frac{c}{2\gamma_{\rm p}^2} \bar{\epsilon}_{\rm pk} \Delta\bar{\epsilon}_{\rm pk} \sigma_{\rm pk} \kappa_{\rm pk} \\ &\times \int_{\bar{\epsilon}_{\rm pk}/2\gamma_{\rm p}}^{\infty} \frac{(dN_{\rm ph}/dE_{\rm ph})}{E_{\rm ph}^2}\, dE_{\rm ph} \ , \end{aligned} \tag{4.4}$$

where $\bar{\epsilon}_{\rm pk} \sim 0.3$ GeV, $\sigma_{\rm pk} \sim 5 \times 10^{-28}\,{\rm cm}^2$, $\kappa_{\rm pk} \sim 0.2$, $\Delta\bar{\epsilon}_{\rm pk} \sim 0.2$ GeV, $\gamma_{\rm p} = E_{\rm p}/m_{\rm p}c^2$, and $dN_{\rm ph}/dE_{\rm ph}$ is the number density of soft photons per photon energy. Assuming an X-ray luminosity $L_{\rm X} \sim 0.1 L_{\rm bol}$ and a power-law template with a spectral index of ~ 2.5 for $dN_{\rm ph}/dE_{\rm ph}$ (Elvis et al. 1994; Marconi et al. 2004), we estimate that $t_{p\gamma} \sim 10^{12}$ yrs $\gg t_{pp} \sim 10^8$ yrs for $E_{\rm p} \sim 1$ PeV accelerated by a 10-kpc scale outflow from a quasar with a bolometric luminosity, $L_{\rm bol} \sim 10^{46}\,{\rm erg\,s^{-1}}$. A detailed comparison of these timescales as a function of $E_{\rm p}$ is shown in Fig.4.1, where we find that $t_{p\gamma}$ is indeed substantially longer than t_{pp} for $E_{\rm p} \lesssim E_{\rm max}$. Therefore, we neglect $p\gamma$ interactions and consider pp collisions as the dominant channel for proton cooling. We have also verified that synchrotron and inverse Compton cooling of protons are negligible (Sturner et al. 1997).

Neutrinos are generated via the decay of charged pions, $\pi^+ \rightarrow \mu^+ + \nu_\mu \rightarrow e^+ + \nu_e + \bar{\nu}_\mu + \nu_\mu$ and $\pi^- \rightarrow \mu^- + \bar{\nu}_\mu \rightarrow e^- + \bar{\nu}_e + \nu_\mu + \bar{\nu}_\mu$. At the source, the production flavor ratio of neutrinos is $(\nu_e : \nu_\mu : \nu_\tau) = (\bar{\nu}_e : \bar{\nu}_\mu : \bar{\nu}_\tau) = (1 : 2 : 0)$, where ν_e, ν_μ and ν_τ are electron, muon and tau neutrinos, respectively. Neutrino oscillations on the way to Earth results in equal numbers of ν_e, ν_μ and ν_τ. We consider ν and $\bar{\nu}$ equally since terrestrial neutrino detectors do not distinguish between them (Crocker et al. 2000).

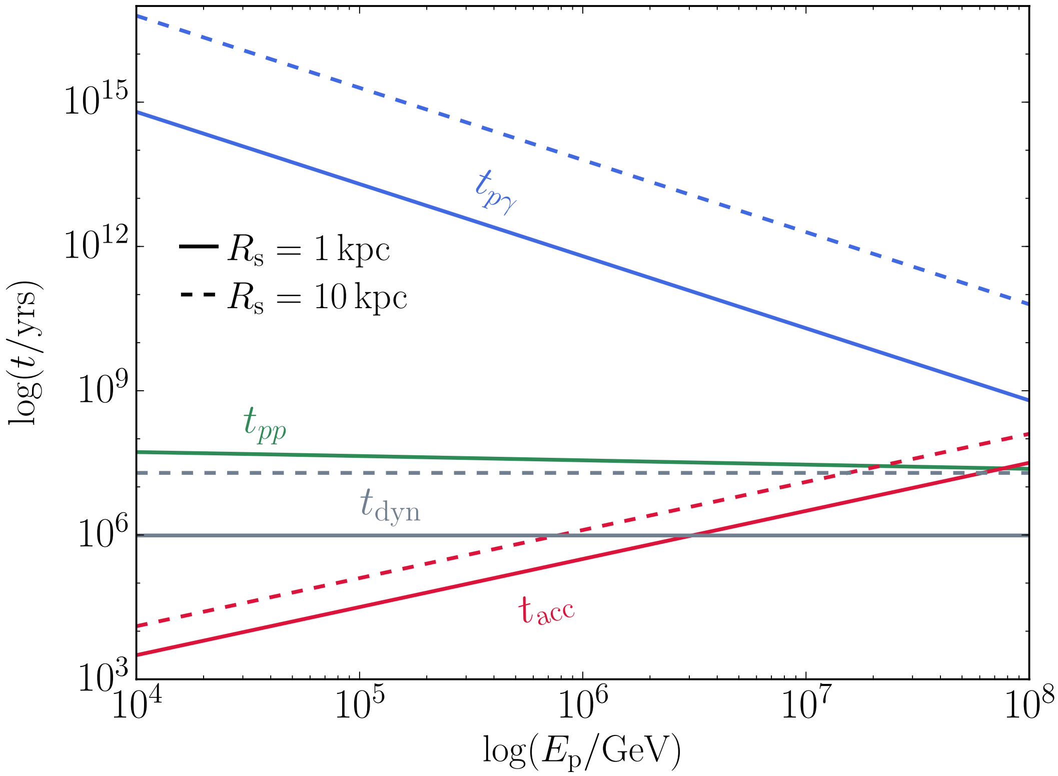

Figure 4.1 Comparison of relevant timescales for the acceleration of protons, t_acc, the dynamics of the outflow shock, t_dyn and for pp and $p\gamma$ interactions, represented by the red, grey, green and blue lines, respectively. The solid and dashed lines correspond to cases where the outflow propagates to distances of 1 kpc and 10 kpc, respectively. We assume a quasar bolometric luminosity of $10^{46}\,\mathrm{erg\,s^{-1}}$ and a magnetic field of 1 μG.

The neutrino spectrum from an individual outflow is given by:

$$\begin{aligned}\Phi_\nu(E_\nu) = cn_{\rm p}\int_0^1 \sigma_{pp}(E_\nu/x)\frac{dN_{\rm p}}{dE_{\rm p}}(E_\nu/x) \\ F_\nu(x, E_\nu/x)\frac{dx}{x}\ ,\end{aligned} \tag{4.5}$$

where $x = E_\nu/E_{\rm p}$ and F_ν is the neutrino spectrum calculated based on the prescription given by Kelner et al. (2006) (see *Appendix* for details). In the lower panel of Fig.4.2, we show the resulting neutrino spectrum when an outflow propagates to the edge of the galactic disk $R_{\rm d}$. The flux is sensitive to $\Gamma_{\rm p}$ in that a steeper proton spectrum leads to fewer neutrinos with energies above 1 TeV. Note that the neutrino flux drops significantly as the outflow propagates outside the galactic disk, due to the declines in the shock velocity and the ambient gas density.

4.3 Cumulative Neutrino Background

The integrated neutrino flux from quasar outflows can be obtained by summing the neutrino emission over the entire quasar population at all bolometric luminosities, $L_{\rm bol}$, and redshifts, z,

$$\begin{aligned}E_\nu^2\Phi_\nu = \iint \Phi(L_{\rm bol}, z)\frac{\bar{L}_\nu(E'_\nu, L_{\rm bol}, z)}{4\pi D_{\rm L}^2(z)} \\ \times\, d\log L_{\rm bol}\frac{dV}{dzd\Omega}dz\end{aligned} \tag{4.6}$$

where V is the comoving cosmological volume, $E'_\nu = E_\nu(1+z)$ is the neutrino energy at the source frame, and $\bar{L}_\nu = t_{\rm Sal}^{-1}\int L_\nu(E_\nu, L_{\rm bol}, z, t)\, dt$ is the time-averaged neutrino flux from an individual source. $\Phi(L_{\rm bol}, z)$ is the bolometric luminosity function, given by (Hopkins et al. 2007):

$$\Phi(L_{\rm bol}, z) = \frac{\Phi_\star}{(L_{\rm bol}/L_\star)^{\gamma_1} + (L_{\rm bol}/L_\star)^{\gamma_2}}\ , \tag{4.7}$$

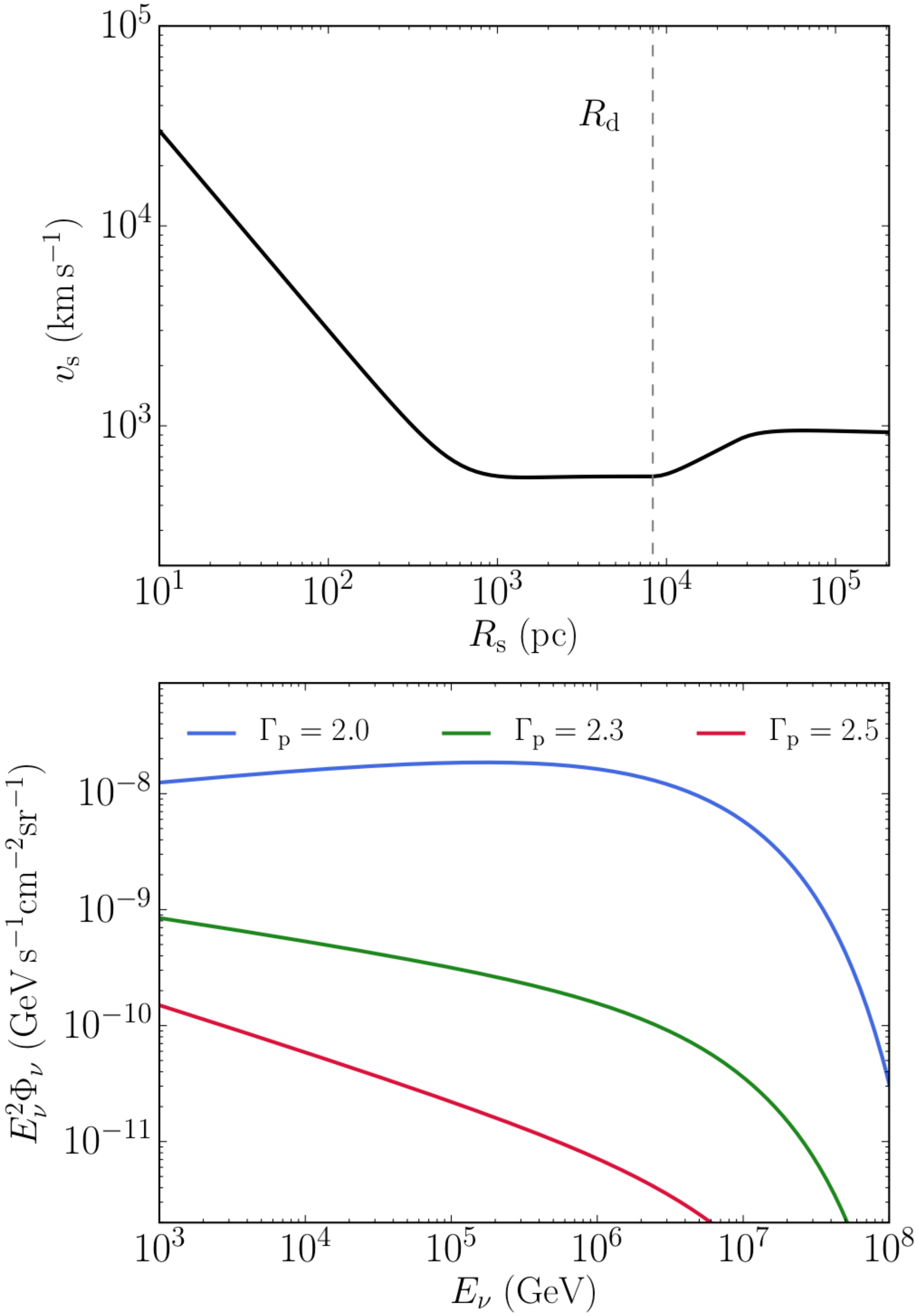

Figure 4.2 Quasar outflow speed vs distance and corresponding neutrino flux summed over all flavors from *pp* collisions. The outflow is hosted by a $10^{12}M_\odot$ halo at redshift of $z = 0.1$. In the upper panel, we show the speed of the outflowing shell, v_s, as a function of its radius, R_s. The dashed vertical line marks the location of the galactic disk, R_d. The lower panel shows the neutrino flux from *pp* collisions as the outflow propagates to the edge of the disk. The blue, green and red lines correspond to different values of the power-law index of the accelerated protons, namely $\Gamma_\mathrm{p} = 2.0$, 2.3 and 2.5, respectively.

where $L_\star$ varies with redshift according to the functional dependence, $\log L_\star = (\log L_\star)_0 + k_{L,1}\xi + k_{L,2}\xi^2 + k_{L,3}\xi^3$, $\xi = \log[(1+z)/(1+z_{\rm ref})]$, with $z_{\rm ref} = 2$ and $k_{L,1}$, $k_{L,2}$ and $k_{L,3}$ being free parameters. We adopt parameter values of the pure luminosity evolution model, where $\log(\Phi_\star/{\rm Mpc}^{-3}) = -4.733$, $(\log(L_\star/L_\odot))_0 = 12.965$, $L_\odot = 3.9\times10^{33}\,{\rm erg\,s^{-1}}$, $k_{L,1} = 0.749$, $k_{L,2} = -8.03$, $k_{L,3} = -4.40$, $\gamma_1 = 0.517$ and $\gamma_2 = 2.096$. The comoving volume per unit solid angle can be expressed as:

$$\frac{dV}{dzd\Omega} = D_{\rm H}\frac{D_{\rm L}^2(z)}{(1+z)^2E(z)}\ , \tag{4.8}$$

where $D_{\rm H} = c/H_0$ and $E(z) = \sqrt{\Omega_{\rm M}(1+z)^3+\Omega_\Lambda}$. We adopt the standard cosmological parameters: $H_0 = 70\,{\rm km\,s^{-1}Mpc^{-1}}$, $\Omega_{\rm M} = 0.3$ and $\Omega_\Lambda = 0.7$ and integrate over the bolometric luminosity range of $L_{\rm bol} = 10^{42}-10^{48}\,{\rm erg\,s^{-1}}$ and the redshift range of $z = 0-5$.

Figure 4.3 shows the cumulative neutrino background (CNB) from quasar-driven outflows compared to the most recent IceCube data, which are fitted by two separate models (Aartsen et al. 2015): a differential model fitted by nine free parameters (indicated as the black points with error bars), and a single power-law model (indicated as the gray shaded region) in the form of $\Phi_\nu^{\rm pl} = \phi\times(E_\nu/100\,{\rm TeV})^{-\gamma}$ where $\phi = 6.7^{+1.1}_{-1.2}\times10^{-18}\,{\rm GeV^{-1}cm^{-2}s^{-1}sr^{-1}}$ and $\gamma = 2.50\pm0.09$.

For each value of $\Gamma_{\rm p}$, we fix $\epsilon_{\rm nt}f_{\rm kin}$ based on the best fit to the EGB and produce the neutrino background without allowing additional freedom in the parameter choices. Interestingly, we find that the resulting flux explains the neutrino background observed by IceCube for $\Gamma_{\rm p}\approx 2.2-2.4$, which is the range of values inferred for shocks around SN remnants (Ackermann et al. 2015a). For $R_{\rm s}\sim 1$ kpc and $v_{\rm s}\sim 10^3\,{\rm km\,s^{-1}}$, $E_{\rm max}\sim 10^6$ GeV while for $R_{\rm s}\sim 50$ kpc and $v_{\rm s}\sim 500\,{\rm km\,s^{-1}}$, $E_{\rm max}$ reaches 10^8 GeV. This leads to

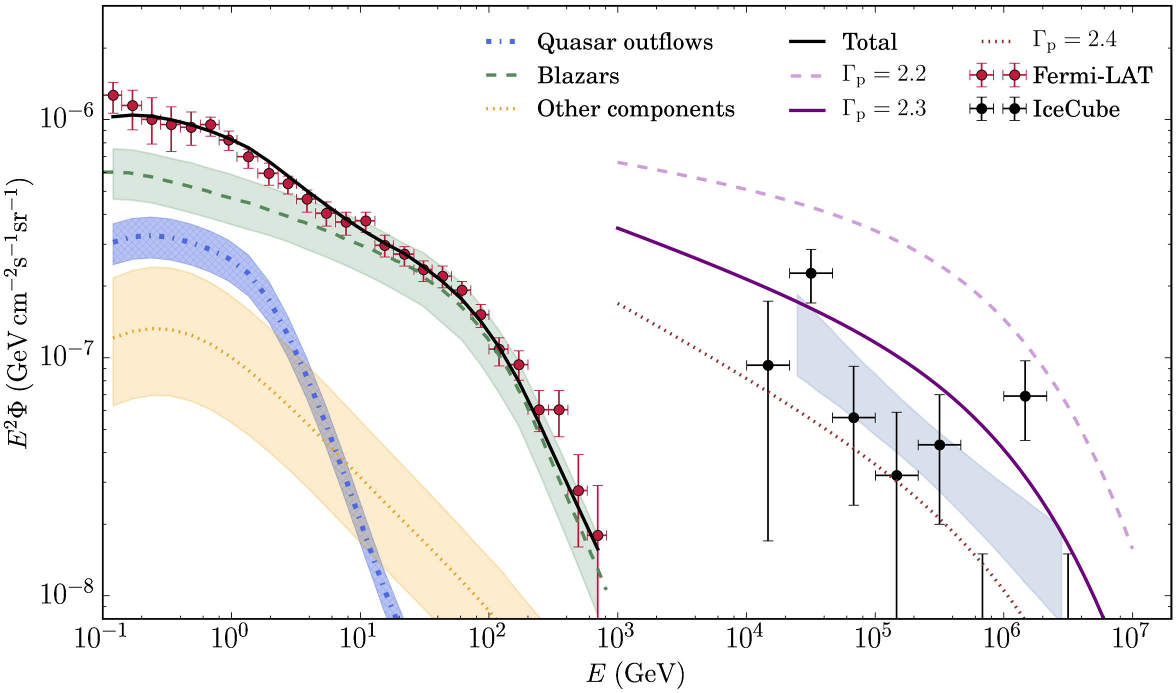

Figure 4.3 Cumulative γ-ray (left) and neutrino background (right) from quasar-driven outflows. The red points with error bars on the left are the observed data points for the γ-ray background from *Fermi*-LAT (Ackermann et al. 2015b). The blue, green and orange shaded regions correspond to the contribution from quasar outflows, blazars and other components (including radio galaxies and star-forming galaxies), respectively, and the total contribution from all components is represented by the solid black line. The power-law and differential model of IceCube neutrino data (all flavors combined) are shown on the right as the gray shaded region and the black points with error bars, respectively (Aartsen et al. 2015). The pink, purple and brown lines correspond to the cumulative neutrino flux produced by quasar outflows where the accelerated protons have an energy distribution with a power-law index of $\Gamma_p = 2.2$, 2.3 and 2.4, respectively.

the spectral break in the neutrino spectrum at $E_\nu \sim 10^5$ GeV, as the production of E_ν is dominated by protons of energy $E_{\rm p} \approx 20 E_\nu$ (Kelner et al. 2006). The observed photon spectrum cuts off at a much lower energy due to the attenuation of emitted γ-rays by electron-positron pair production on the cosmic UV-optical-infrared background photons out to the high redshifts $z > 2$ where most quasars reside (Stecker et al. 2007).

4.4 Multi-messenger Implications

Assuming *pp* interactions, the all flavor neutrino flux can be expressed in terms of the γ-ray flux, $E_\nu^2 \Phi_\nu \approx 6 E_{\rm g}^2 \Phi_\gamma$ for $E_\nu \approx 0.5 E_{\rm g}$ (Murase et al. 2013; Zandanel et al. 2015; Murase et al. 2016). This relation sets an upper limit on the power-law index of the accelerated protons (Murase et al. 2013):

$$\Gamma_{\rm p} \lesssim 2 + \frac{\ln\left[3 E_{\rm g}^2 \Phi_\gamma|_{E_{\rm g}} / (E_\nu^2 \Phi_\nu|_{E_\nu})\right]}{\ln(2E_\nu/E_{\rm g})} \ . \tag{4.9}$$

Given the most recent *Fermi*-LAT data (Ackermann et al. 2015b) and IceCube data (Aartsen et al. 2015), we have verified that $\Gamma_{\rm p} \lesssim 2.2 - 2.4$, in agreement with theoretical models (Caprioli 2012; Caprioli & Spitkovsky 2014b) and observations of SN remnant shocks (Ackermann et al. 2015a). If $\Gamma_{\rm p}$ is taken beyond this limit, the EGB would be overproduced when attempting to accommodate the neutrino background.

Other astrophysical sources have been confirmed to produce neutrinos and may contribute to the CNB (Waxman & Loeb 2001; Alvarez-Muñiz & Halzen 2002; Mannheim et al. 2001; Loeb & Waxman 2006; Waxman & Bahcall 1999, 1997). Blazars make up approximately half of the EGB at $E_{\rm g} \lesssim 10$ GeV and almost all the flux at higher photon energies. They are estimated to explain the entire neutrino background at $E_\nu \gtrsim 0.5$

PeV but only $\sim 10\%$ at lower energies, based on a leptohadronic model (Padovani et al. 2015). Star-forming galaxies produce $\sim 13 \pm 9\%$ of the EGB (Ackermann et al. 2012) via pp interaction, indicating that they do not contribute significantly to the CNB for values of $\Gamma_{\rm p}$ of interest (Tamborra et al. 2014). The central AGN in galaxy clusters is estimated to account for the neutrino background at $E_\nu \gtrsim 0.1$ PeV, but not at lower energies (Fang & Olinto 2016). Additionally, the contribution from galaxy clusters to the EGB is only a few percent and thus negligible (Zandanel et al. 2015; Fornasa & Sánchez-Conde 2015). Other sources can be ruled out based on the γ-ray/neutrino branching ratio as they do not generate sufficient γ-ray emission to account for the EGB. In comparison, the quasar outflow model can fully explain both the missing component of the EGB and the CNB. The multi-messenger link between γ-ray and neutrino emission can be used to trace and confirm individual sources of neutrinos (Becker et al. 2005; Murase et al. 2016).

4.5 Summary

In this chapter, we adopted the quasar outflow parameters constrained by the best fit to the EGB data and calculated the simultaneous neutrino emission from these outflows. The integrated neutrino flux of $\sim 10^{-7}\,\mathrm{GeV\,s^{-1}\,cm^{-2}\,sr^{-1}}$ at $E_\nu \approx$10 TeV, naturally explains the most recent IceCube data. The dominant mechanism for producing the γ-ray and neutrino emission is the interaction between protons accelerated by the outflow and the ambient interstellar protons. In such a scenario, the branching ratio between γ-rays and neutrinos sets an upper limit on the power-law index of the accelerated proton distribution $\Gamma_{\rm p}$ to be $\sim 2.2 - 2.4$ as inferred in SN remants (Ackermann et al. 2015a; Caprioli 2012; Caprioli & Spitkovsky 2014b). Alternative sources such as blazars, star-forming galaxies and galaxy clusters can not account for both the γ-ray and neutrino backgrounds, while quasar outflows naturally explain both with a set of parameters consistent with direct observations of outflows (Tombesi et al. 2015) and SN remnants (Ackermann et al. 2015a). The inferred multi-messenger link can be used to constrain the high-energy physics of strong shocks at cosmological distances.

Acknowledgments

We thank Douglas Finkbeiner for helpful comments on the manuscript. This work is supported by NSF grant AST-1312034.

Appendix

Following Kelner et al. (2006), we use an analytical approximation for the neutrino spectrum. The muonic neutrino spectrum F_{ν_μ} is given by $F_{\nu_\mu} = F_{\nu_\mu^{(1)}} + F_{\nu_\mu^{(2)}}$, where $F_{\nu_\mu^{(1)}}$ corresponds to neutrinos produced through $\pi \to \mu\nu_\mu$,

$$\begin{aligned} F_{\nu_\mu^{(1)}}(x, E_{\mathrm{p}}) = & B' \frac{\ln y}{y} \left[\frac{1 - y^{\beta'}}{1 + k' y^{\beta'}(1 - y^{\beta'})} \right]^4 \left[\frac{1}{\ln y} \right. \\ & \left. - \frac{4\beta' y^{\beta'}}{1 - y^{\beta}} - \frac{4k'\beta' y^{\beta'}(1 - 2y^{\beta'})}{1 + k' y^{\beta'}(1 - y^{\beta'})} \right] , \end{aligned} \tag{4.10}$$

with $x = E_{\nu_\mu}/E_{\mathrm{p}}$ and $y = x/0.427$. Here,

$$B' = 1.75 + 0.204\ell + 0.010\ell^2 \ , \tag{4.11}$$

$$\beta' = \left(1.67 + 0.111\ell + 0.0038\ell^2\right)^{-1} \ , \tag{4.12}$$

$$k' = 1.07 - 0.086\ell + 0.002\ell^2 \ . \tag{4.13}$$

The muonic neutrino spectrum from the decay of muons $F_{\nu_\mu^{(2)}}$ can be described as:

$$F_{\nu_\mu^{(2)}}(x, E_\mathrm{p}) = -B_e \frac{\left[1 + k_e(\ln x)^2\right]^3}{x(1 + 0.3/x^{\beta_e})} (\ln x)^5 \ , \tag{4.14}$$

where $x = E_e/E_\pi$. Here,

$$B_e = \left(69.5 + 2.65\ell + 0.3\ell^2\right)^{-1} \tag{4.15}$$

$$\beta_e = \left(0.201 + 0.062\ell + 0.00042\ell^2\right)^{-1/4} \ , \tag{4.16}$$

$$k_e = \frac{0.279 + 0.141\ell + 0.0172\ell^2}{0.3 + (2.3 + \ell)^2} \ . \tag{4.17}$$

The integrated γ-ray/neutrino emission can be expressed as, similarly to Eqn.4.5:

$$\begin{aligned} E^2_{\gamma/\nu}\Phi_{\gamma/\nu} = \frac{c}{4\pi H_0} \iint \phi(L_\mathrm{bol}, z) \frac{L_{\gamma/\nu}(E'_{\gamma/\nu}, L_\mathrm{bol}, z)}{E(z)} \\ \times f(E'_{\gamma/\nu}, z) \, d\log L_\mathrm{bol} \, dz \ , \end{aligned} \tag{4.18}$$

where $f(E'_{\gamma/\nu}, z) = \exp[-\tau_{\gamma\gamma}(E'_\gamma, z)]$ for γ-rays and $f(E'_{\gamma/\nu}, z) = 1$ for neutrinos. $\tau_{\gamma\gamma}$ is the optical depth of extragalactic background light (Stecker et al. 2007). The resulting γ-ray and neutrino backgrounds are shown in the left and middle panel of Fig.4.3, respectively.

Chapter 5

Ultra High Energy Cosmic Rays from Non-Relativistic Quasar Outflows

This thesis chapter originally appeared in the literature as

X. Wang & A. Loeb, Ultra High Energy Cosmic Rays from Non-Relativistic Quasar Outflows, *Physical Review, D*, 95, 063007 (2017)

Abstract

It has been suggested that non-relativistic outflows from quasars can naturally account for the missing component of the extragalactic γ-ray background and explain the cumulative neutrino background through pion decay in collisions between protons accelerated by the outflow shock and interstellar protons. Here we show that the same

quasar outflows are capable of accelerating protons to energies of $\sim 10^{20}$ eV during the early phase of their propagation. The overall quasar population is expected to produce a cumulative ultra high energy cosmic ray flux of $\sim 10^{-7}\,\mathrm{GeV\,cm^{-2}s^{-1}sr^{-1}}$ at $E_{\rm CR} \gtrsim 10^{18}$ eV. The spectral shape and amplitude is consistent with recent observations for outflow parameters constrained to fit secondary γ-rays and neutrinos without any additional parameter tuning. This indicates that quasar outflows simultaneously account for all three messengers at their observed levels.

5.1 Introduction

The observed ultra high energy cosmic ray (UHECR) spectrum is characterized by various spectral features (Hillas 2006; Kotera & Olinto 2011). The hardening of the spectrum at $\sim 4 \times 10^{18}$ eV, so-called the ankle, can be produced by a transition from Galactic to extragalactic cosmic rays (CRs) for either mixed composition or iron-dominated models (Allard et al. 2007), or by pair production propagation losses in proton-dominated models (Berezinsky et al. 2006). The flux suppression detected above $\sim 3 \times 10^{19}$ eV, is either caused by the interaction between UHECRs and the cosmic microwave background (CMB) photons, the so-called Greisen-Zatsepin-Kuzmin (GZK) cutoff (Greisen 1966; Zatsepin & Kuz'min 1966), or is potentially associated with the maximum energy of the accelerated nuclei (Aloisio et al. 2011). The spectrum can be fitted by a power-law with spectral index of ~ 3 between the cosmic knee ($\sim 10^{15}$ eV) and the ankle, and ~ 2.6 between the ankle and the GZK cutoff. The origin of UHECRs remains uncertain but it is believed to be of an extragalactic origin (Kotera & Olinto 2011).

Growing observational evidence reveals the existence of large-scale outflows driven by the active galactic nuclei (AGN). It includes the detection of multi-phase outflows in nearby ultraluminous infrared galaxies (Rupke & Veilleux 2011; Tombesi et al. 2015) and the presence of broad absorption lines in quasars (Zakamska & Greene 2014; Arav et al. 2015). In chapter 2 (Wang & Loeb 2015), we derived a detailed hydrodynamical model of quasar outflow's interaction with the ambient interstellar medium (ISM) (See chapter 2 for details). Protons accelerated by the outflow shock to relativistic energies interact with the interstellar protons and produce secondary γ-ray photons and neutrinos via pion production that naturally account for the missing component of the extragalactic γ-ray background (EGB) (Wang & Loeb 2016a), as well as the cumulative neutrino background (CNB) (Wang & Loeb 2016b).

In this chapter, we calculate the cumulative UHECR flux above $\sim 10^{18}$ eV produced by non-relativistic quasar outflows and discuss the multi-messenger implications with secondary γ-rays and neutrinos simultaneously generated by the same population of sources.

5.2 UHECR Production

Ultra-fast winds with a velocity $\sim 0.1\,c$ are continuously injected into the ISM of the host galaxy during the quasar's lifetime (King & Pounds 2015), taken to be the Salpeter time $t_{\rm Sal} \sim 4 \times 10^7$ yrs, and drive a forward outflow shock that accelerates protons to relativistic energies via the Fermi acceleration, in analogy with supernova-driven shocks (Caprioli 2012). Here we consider the non-relativistic spherical outflows, rather than the collimated relativistic jets seen in only $\sim 10\%$ of the AGN population (Faucher-Giguère

& Quataert 2012; King & Pounds 2015). The resulting proton spectrum can be described by a power-law profile with an exponential cutoff (Caprioli 2012):

$$\frac{dN}{dE_{\rm p}} = N_0 E_{\rm p}^{-\Gamma_{\rm p}} \exp\left(-\frac{E_{\rm p}}{E_{\rm max}}\right) \ , \tag{5.1}$$

where $E_{\rm p}$ is the proton energy, $E_{\rm max}$ is the maximum energy of the accelerated protons and $\Gamma_{\rm p}$ is the power-law index. N_0 is the normalization constant that can be constraint by:

$$\int_{E_{\rm min}}^{E_{\rm max}} E\frac{d\dot{N}}{dE}dE = \epsilon_{\rm nt} L_{\rm kin} \ , \tag{5.2}$$

where the minimum proton energy $E_{\rm min} \sim m_{\rm p}c^2$, $m_{\rm p}$ is the proton mass and $\epsilon_{\rm nt}$ is the fraction of outflow's kinetic luminosity $L_{\rm kin}$ converted to accelerated protons. We assume that $L_{\rm kin}$ is a fraction, $f_{\rm kin}$, of the quasar's bolometric luminosity $L_{\rm bol}$. Secondary γ-ray photons and neutrinos are produced via pion decay from interaction between accelerated protons and ambient protons in the ISM. We adopt $\epsilon_{\rm nt} \sim 0.1$ similarly to the conditions in supernova remnants (SNRs) (Caprioli 2012; Caprioli & Spitkovsky 2014b) and $f_{\rm kin} \sim 1-5\%$ from fitting the resulting γ-rays and neutrinos to the EGB (Wang & Loeb 2016a) and CNB (Wang & Loeb 2016b), consistently with observations (Ackermann et al. 2015b) and theoretical models (Caprioli 2012) of supernova shocks. The maximum energy of the accelerated protons, $E_{\rm max}$, can be extrapolated from $E_{\rm max} \approx E_{\rm sh}\omega_{\rm c}t_{\rm dyn}/3\kappa$ for shocks with an Alfvén Mach number $\mathcal{M} \gtrsim 100$ (Caprioli & Spitkovsky 2014b), where $E_{\rm sh} = m_{\rm p}v_{\rm s}^2/2$, $\omega_{\rm c} = eB_0/m_{\rm p}c$, $\kappa \propto B_0/B \propto 1/\sqrt{\mathcal{M}}$, and B_0 and B are the pre-shock and post-shock magnetic field, respectively. B_0 can be obtained from equipartition of energy in the ambient ISM. Here $\mathcal{M} = v_{\rm s}/v_{\rm A}$, $v_{\rm A} = B_0/\sqrt{4\pi n_0 m_{\rm p}}$ and n_0 and T_0 are the ambient ISM number density and temperature, described by Wang & Loeb (2015). The dynamical time, $t_{\rm dyn} \sim R_{\rm s}/v_{\rm s}$, where $R_{\rm s}$ and $v_{\rm s}$ are the radius and velocity of the outflow, respectively, as determined from outflow hydrodynamics (see chapter 2 for details). For $R_{\rm s} \lesssim 200$ pc, $\mathcal{M} \sim 10^2 - 10^3$. We can also derive $E_{\rm max}$ by equating the acceleration timescale (Blandford & Eichler 1987), $t_{\rm acc} \sim E_{\rm p}c/eBv_{\rm s}^2$, to the minimum of the dynamical ($t_{\rm dyn}$) and cooling ($t_{\rm cool}$) timescale. For simplicity, we adopt the most optimistic assumption of energy equipartition (Bustard et al. 2017), in analogy to SNRs, namely that a fraction of the post-shock thermal energy is carried by the magnetic field, $B^2/8\pi = \xi_{\rm B} n_{\rm s} kT_{\rm s}$, where $\xi_{\rm B} \sim 0.1$ based on observations (Chevalier 1998), k is the Boltzmann constant, and $n_{\rm s}$ and $T_{\rm s}$ are the number density and temperature of the shocked medium, respectively. We have verified that the results from the above two approaches are consistent.

Accelerated protons lose energies via hadronuclear (*pp*) or photohadronic ($p\gamma$) interactions. In the *pp* scenario, the cooling timescale is given by (Kelner et al. 2006):

$$t_{pp}^{-1} = n_{\rm s}\sigma_{pp}c\kappa_{pp} \ , \tag{5.3}$$

where $\kappa_{pp} \sim 0.5$ is the inelasticity parameter, $\sigma_{pp} \approx 30[0.95 + 0.06\ln(E_{\rm kin}/1{\rm GeV})]$ mb is the cross section of *pp* collision (Aharonian & Atoyan 2000) and $E_{\rm kin} = E_{\rm p} - m_{\rm p}c^2$. The $p\gamma$ cooling timescale can be obtained by (Stecker 1968; Waxman & Bahcall 1997):

$$t_{p\gamma}^{-1} = \frac{c}{2\gamma_{\rm p}^2}\int_{\epsilon_{\rm th}}^{\infty} d\epsilon\, \sigma_{p\gamma}(\epsilon)\kappa(\epsilon)\epsilon \int_{\epsilon/2\gamma_{\rm p}}^{\infty} d\epsilon_\gamma\, \epsilon_\gamma^{-2}\, n(\epsilon_\gamma) \ , \tag{5.4}$$

where $\epsilon_{\rm th} \sim 145$ MeV is the threshold energy for pion production in the rest frame of the protons and $\gamma_{\rm p} = E_{\rm p}/m_{\rm p}c^2$. The numerical approximation for the total photohadronic cross section, $\sigma_{p\gamma}$, is taken from Mücke et al. (2000). $n(\epsilon_\gamma)$ is the number density of soft photons in the energy range ϵ_γ to $\epsilon_\gamma + d\epsilon_\gamma$. We adopt a template for quasar's spectral energy distribution which includes infrared emission from the dusty torus, optical and UV emission from the accretion disk and X-ray emission from the corona (Marconi et al.

2004; Collinson et al. 2017). A comparison of the relevant timescales is shown in Figure 5.1.

The most effective acceleration of UHECRs occurs in the early phase of outflow's propagation. We estimate the optical depth of protons interacting with soft photons from the quasar and verify that only absorption of CMB photons have a non-negligible impact on the UHECR spectrum. The resulting $E_{\rm max}$ and B as a function of outflow radius $R_{\rm s}$ and elapsed time t is depicted in Figure 5.2.

Figure 5.2 shows that $E_{\rm max}$ reaches $\sim 10^{20}$ eV after the wind is launched and rapidly declines to $\lesssim 10^{17}$ eV as $v_{\rm s}$ decreases when the outflow enters the galactic halo, below the energy range of interest here. The duration of UHECR production is $\sim 10^4$ yrs, $\sim 0.01\%$ of a quasar's lifetime. This suggests that only $\sim 0.01\%$ of quasars at any given time produce UHECRs; this sets a threshold on the sample size of AGNs needed to obtain a meaningful cross-correlation signal with the arrival directions of UHECRs. An additional constraint on UHECR production is the size of the source and the magnetic field intensity calibrated by equipartition with the post-shock thermal energy, known as the Hillas criterion (Hillas 1984). The UHECR source should be capable of confining the particles up to $E_{\rm max}$, or equivalently, the size of the source must be larger than the maximum Larmor radius of the particle. Measurements by the Pierre Auger Collaboration favor a heavier composition at the highest energies (The Pierre Auger Collaboration et al. 2015). However, there are uncertainties in the modelling of hadronic interactions in the shower (Kotera & Olinto 2011). For simplicity, we adopt a proton-only prescription for the UHECRs accelerated by outflows since the ISM is mainly composed of protons, but we expected heavier nuclei to be accelerated as well based on the ISM metallicity. We verified that the size of the outflow satisfies $R_{\rm s} \gtrsim E_{\rm p}/eB$, as shown in the shaded region

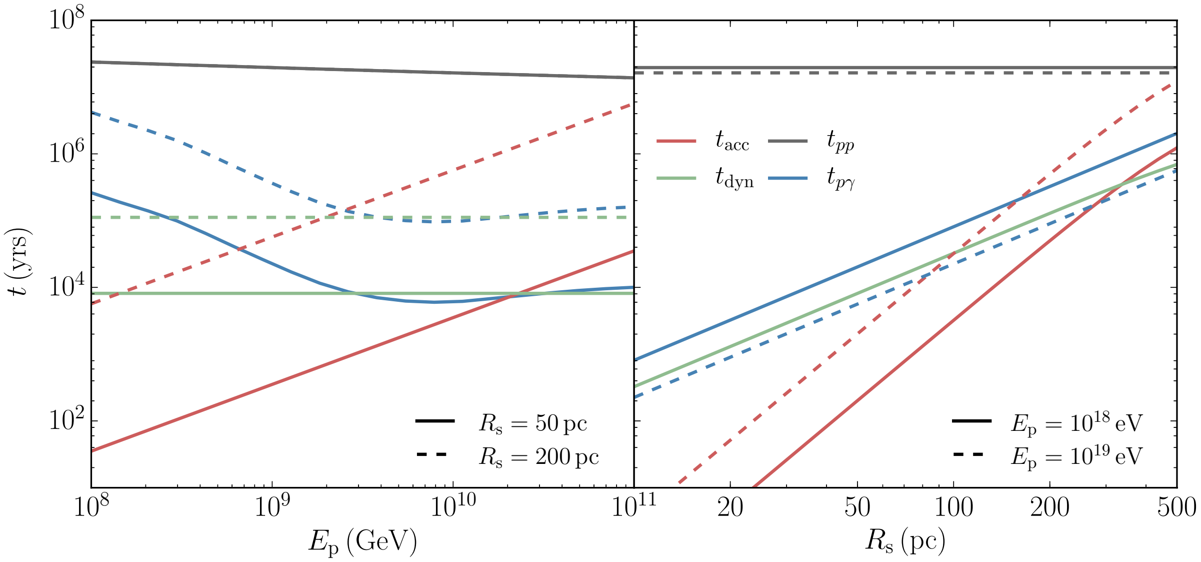

Figure 5.1 Comparison of relevant timescales. On the left panel, we compare the acceleration, dynamical, pp and $p\gamma$ timescales as a function of proton energy when the outflow propagates to 50 pc (solid) and 200 pc (dashed), respectively, within a host galaxy halo of mass of $10^{12} M_\odot$ at a redshift of $z = 0.1$. In the right panel, we show the timescales as a function of outflow radius for $E_\mathrm{p} = 10^{18}$ eV (solid) and 10^{19} eV (dashed). The gas density profile is self-consistently determined by the halo mass and redshift (Wang & Loeb 2015). The magnetic field energy density is estimated to be a fraction $\xi_\mathrm{B} \sim 0.1$ of the equipartition value. For $\epsilon_\mathrm{nt} \sim 10\%$ and $f_\mathrm{kin} \sim 5\%$, we find that pp collision timescale, t_{pp}, is substantially longer than $p\gamma$ interaction timescale, $t_{p\gamma}$, at lower energies and smaller outflow radii. Therefore, the dynamical timescale t_dyn and $t_{p\gamma}$ set a tighter constraint on E_max.

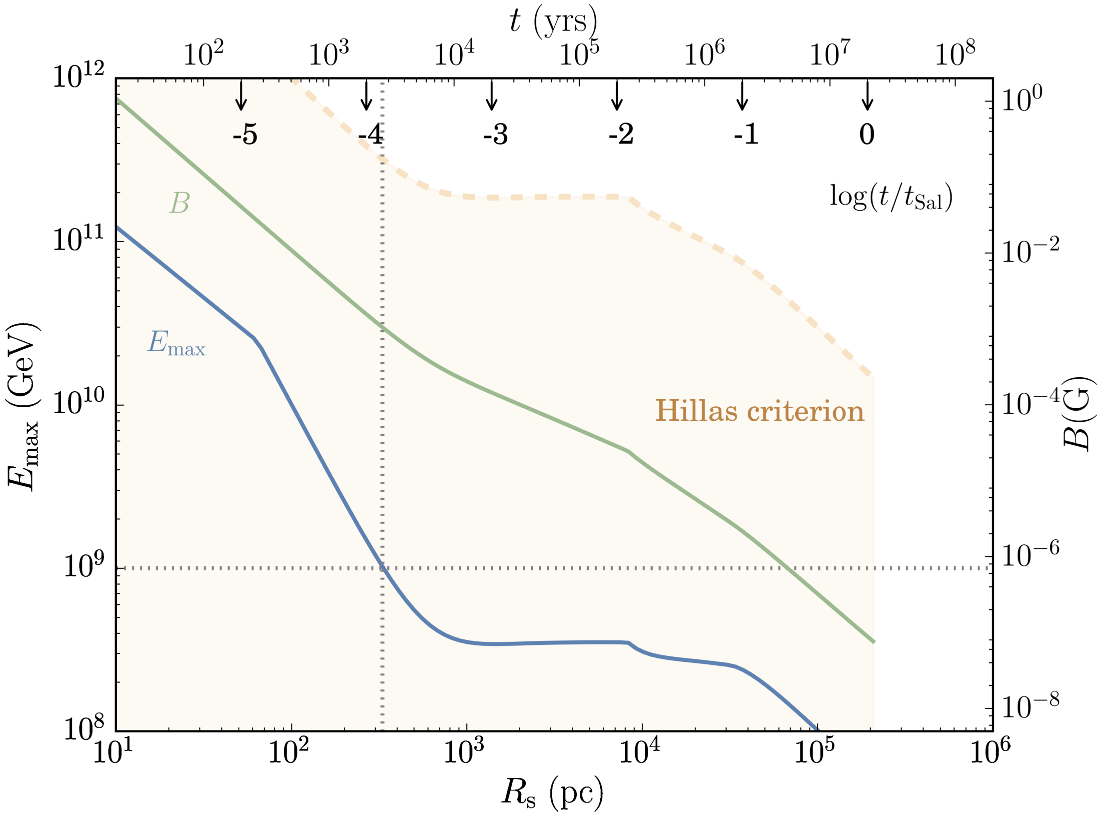

Figure 5.2 Maximum energy of the accelerated protons $E_{\rm max}$ (blue line; left vertical axis) and magnetic field behind the outflow shock B (green line; right vertical axis) as a function of outflow radius $R_{\rm s}$ (bottom axis) and time elapsed t (top axis). Here, we calibrate $E_{\rm max}$ and B by the consideration of equipartition with the post-shock thermal energy, for a halo mass $M_{\rm h} = 10^{12} M_\odot$, redshift $z = 0.1$, $\xi_{\rm B} \sim 0.1$, $\epsilon_{\rm nt} \sim 10\%$ and $f_{\rm kin} \sim 5\%$. The gray dashed lines mark the energy threshold of UHECRs at $E \sim 10^{18}$ eV. The upper axis is also scaled to the Salpeter time $t_{\rm Sal}$, indicating the fraction of a quasar's lifetime spent at each location. The shaded beige region represents the allowed $E_{\rm max}$ constrained by the Hillas criterion to confine protons (Hillas 2006; Kotera & Olinto 2011).

of Figure 5.2, and find that $t_{\rm dyn}$ and $t_{p\gamma}$ set a tighter constraint on $E_{\rm max}$.

5.3 Cumulative UHECR Intensity

The UHECRs interact with CMB photons in the intergalactic medium and produce secondary particles via photohadronic interaction which leads to pion production, $p + \gamma_{\rm CMB} \rightarrow n +$ pions, and pair production, $p + \gamma_{\rm CMB} \rightarrow p + e^+ + e^-$. We follow the detailed prescription given by Berezinsky et al. (2006) to calculate the corresponding energy losses, which produces the dip at $10^{18} - 10^{20}$ eV, where the second flattening at $\sim 10^{19}$ eV accounts for the ankle (Berezinsky et al. 2006; Kotera & Olinto 2011). The expected spectral shape is identical to the injection spectrum at each snapshot during the propagation of the outflow as UHECRs with energies $\gtrsim 10^{18}$ eV are not confined in the Galaxy and thus propagation effect can be neglected (Kotera & Olinto 2011). The piling up of spectra at each outflow snapshot makes the cumulative spectrum steeper due to the decrease of $E_{\rm max}$ at large $R_{\rm s}$. We estimate the cumulative UHECR intensity by summing over the entire quasar population:

$$\begin{aligned} E_{\rm CR}^2 \Phi_{\rm CR} = \frac{c}{4\pi H_0} \iint \phi(L_{\rm bol}, z) \frac{L_{\rm CR}(E'_{\rm CR}, L_{\rm bol}, z)}{E(z)} \\ \times f(E'_{\rm CR}, z)\, d\log L_{\rm bol}\, dz\ , \end{aligned} \tag{5.5}$$

where $L_{\rm CR} = E_{\rm CR}^2 d\dot{N}/dE_{\rm CR}$, $E'_{\rm CR} = (1+z)E_{\rm CR}$ is the intrinsic CR energy, $L_{\rm bol}$ is the bolometric luminosity, $\phi(L_{\rm bol}, z)$ is the bolometric luminosity function of quasars (Hopkins et al. 2007) and $E(z) = \sqrt{\Omega_{\rm M}(1+z)^3 + \Omega_\Lambda}$. We adopt the standard cosmological parameters, $H_0 = 70\,{\rm km\,s^{-1}Mpc^{-1}}$, $\Omega_{\rm M} = 0.3$ and $\Omega_\Lambda = 0.7$ (Planck Collaboration et al. 2016). $f(E'_{\rm CR}, z)$ is the modification factor due to interaction with the CMB photons (Berezinsky et al. 2006). We assign outflows to all quasars, consistently with the source redshift evolution rate limits set by the *Fermi*-LAT and IceCube observations (Murase & Waxman 2016).

In Figure 5.3, we show the most recent γ-ray data from *Fermi*-LAT (Ackermann et al. 2015b), neutrino data from IceCube (Aartsen et al. 2015) and UHECR data from the Pierre Auger Observatory (The Pierre Auger Collaboration et al. 2015) and Telescope Array (TA) (Fukushima 2015). Using values of $\epsilon_{\rm nt}$, $f_{\rm kin}$ and $\Gamma_{\rm p}$ constrained by fitting γ-rays to the EGB (Wang & Loeb 2016a) (left section) and neutrinos to the CNB (Wang & Loeb 2016b) (middle section), we derive the UHECR spectrum (right section) with $\Gamma_{\rm p} \sim 2.3 - 2.4$ at $E_{\rm CR} \gtrsim 10^{18}$ eV without additional parameter tuning. For $\epsilon_{\rm nt} \sim 10\%$, the best fit $f_{\rm kin} \sim 1 - 5\%$ (Wang & Loeb 2016a) is consistent with theoretical models and observations (Caprioli 2012; Tombesi et al. 2015). It is important to note that we naturally obtain the spectral shape and amplitude of the UHECR flux from the same outflow model that explains the EGB and CNB. A simultaneous fit to the UHECR spectrum, composition and anisotropy is challenging, as shown by the preliminary results from the Pierre Auger Collaboration (The Pierre Auger Collaboration et al. 2015). The spectrum could be sensitive to the detailed photohadronic interactions during UHECR propagation (Alves Batista et al. 2015), while the spectral shape might be affected by the presence of intervening magnetic fields at $E_{\rm CR} \lesssim 10^{18}$ eV (Alves Batista & Sigl 2014).

5.4 Multi-messenger Implications

Secondary photons and neutrinos are produced as UHECRs interact with the ambient interstellar protons. The resulting γ-ray photons can naturally account for the missing component of the EGB at $E_{\rm g} \lesssim 10$ GeV as suggested by the most recent *Fermi*-LAT

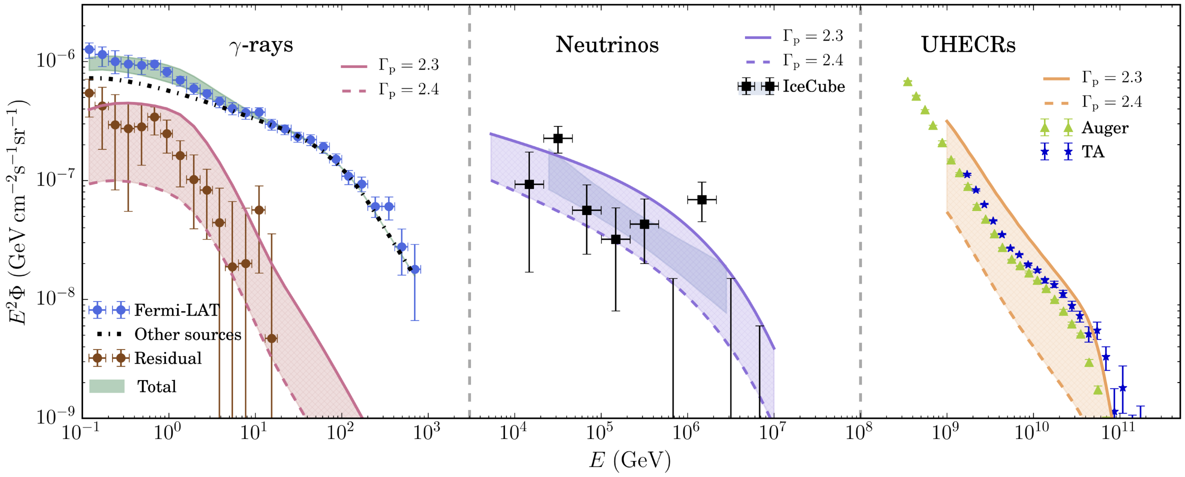

Figure 5.3 γ-ray photons, neutrinos and UHECRs produced by quasar outflows. From left to right, we show the cumulative γ-ray, neutrino background and UHECR flux for $\Gamma_p = 2.3$ (solid line) and $\Gamma_p = 2.4$ (dashed line), represented by the hatched regions, respectively. For the γ-ray background, the contribution from other components to the EGB including blazars, radio galaxies and star-forming galaxies is plotted in comparison with the most recent *Fermi*-LAT data (Ackermann et al. 2015b). The cumulative neutrino background observed by IceCube (Aartsen et al. 2015), represented by the data points and the gray band. In the right section, we show the most recent data from Pierre Auger Observatory (The Pierre Auger Collaboration et al. 2015) and TA (Fukushima 2015), and derive the cumulative UHECR intensity without additional parameter tuning. For simplicity, we assume a pure-proton prescription consistent with the composition of the ISM. We find that quasar outflows naturally explain the spectra of all three messengers with parameters consistent with observations (Tombesi et al. 2015) and theoretical models for supernova-driven shocks (Caprioli 2012).

observation (Ackermann et al. 2015b; Wang & Loeb 2016a), while the associated neutrinos explain the CNB as observed by IceCube (Aartsen et al. 2015; Wang & Loeb 2016b). With $\epsilon_{\rm nt} \sim 10\%$, $f_{\rm kin} \sim 1-5\%$ and $\Gamma_{\rm p} \sim 2.3-2.4$, constrained to fit the *Fermi*-LAT and IceCube data, we naturally explain the UHECR flux without additional parameter tuning, as shown in Figure 5.3. This is consistent with parameter values inferred from observations of outflows (Tombesi et al. 2015) as well as the branching ratio between secondary γ-rays and neutrinos, which sets an upper limit on the power-law index of the injection spectrum to be $\lesssim 2.2-2.4$ (Wang & Loeb 2016b; Murase et al. 2016). Indeed, recent γ-ray observations suggest the existence of hadronic emission from an outflow in a nearby galaxy (Lamastra et al. 2016). However, the predicted γ-ray emission from an individual outflow is too faint to be detected outside the local Universe ($z \sim 0.1$), explaining why these outflows have been barely detected in γ-rays. The simultaneous radio emission from accelerated electrons by the same outflow shocks is sufficiently bright to be observed to a redshift of ~ 5 and is free of contamination from scattered quasar light by the surrounding electrons in the halo (Wang & Loeb 2015). Radio observations with the *Jansky Very Large Array* and the *Square Kilometre Array* could therefore directly image the shock front. Stacking analysis of γ-rays and neutrinos can be performed in the future to search for more direct evidence of quasar outflows (Wang & Loeb 2016a). Alternative UHECR sources such as blazars (Murase et al. 2012) could make up to $\sim 50\%$ of the EGB at $E_{\rm g} \lesssim 10$ GeV through synchrotron self-Compton emission and potentially dominate the EGB at higher energies (Ajello et al. 2015). However, they produce only $\sim 10\%$ of the CNB at energies below ~ 0.5 PeV (Padovani et al. 2015). Radio galaxies with misaligned jets can accelerate UHECRs via the same mechanism as blazars (Dermer et al. 2009). However, they account for only $\lesssim 10\%$ of the EGB at $E_{\rm g} \lesssim 10$ GeV (Wang & Loeb 2016a) and do not fully account for the CNB. Another potential UHECR source is the gamma-ray bursts (GRBs) (Waxman & Bahcall 1997), which can not account for most of the EGB. Searches have found no correlation between γ-ray emission from *Fermi* sources and UHECRs (Álvarez et al. 2016), disfavoring candidates such as blazars, radio galaxies and GRBs. The identification of UHECR sources with γ-ray and neutrino sources would provide a smoking gun evidence for their origin (Becker et al. 2005; Kotera & Olinto 2011).

5.5 Summary

In this chapter, we have shown that the cumulative UHECR flux produced by non-relativistic quasar outflows naturally accounts for the observed spectrum at $E_{\rm CR} \gtrsim 10^{18}$ eV by Auger (The Pierre Auger Collaboration et al. 2015) and TA (Fukushima 2015). We constrained the free parameters of the model to fit data on the secondary γ-rays and neutrinos without additional parameter tuning. We find that the best fit power-law index of the injection spectrum is $\Gamma_{\rm p} \sim 2.3 - 2.4$, consistent with observations of supernova remnants and theoretical models (Caprioli 2012). Altogether, quasar outflows simultaneously produce all three messengers – γ-rays, neutrinos and UHECRs – that account for the missing component of the EGB, the CNB and the observed UHECR spectrum. Additionally, the lack of correlation between UHECR events and current γ-ray data favors the outflow model over other sources such as blazars, radio galaxies and GRBs (Álvarez et al. 2016).

Acknowledgments

We thank Xuening Bai and Rafael Alves Batista for helpful comments on the manuscript.

This work is supported by NSF grant AST-1312034.

Chapter 6

Formation and Spatial Distribution of Hypervelocity Stars in AGN Outflows

This thesis chapter originally appeared in the literature as

X. Wang & A. Loeb, Formation and Spatial Distribution of Hypervelocity Stars in AGN Outflows, *New Astronomy*, 61, 95 (2018)

Abstract

We study star formation within outflows driven by active galactic nuclei (AGN) as a new source of hypervelocity stars (HVSs). Recent observations revealed active star formation inside a galactic outflow at a rate of $\sim 15\,M_{\odot}\,\mathrm{yr}^{-1}$. We verify that the shells swept up by an AGN outflow are capable of cooling and fragmentation into cold clumps embedded in a hot tenuous gas via thermal instabilities. We show that cold clumps of $\sim 10^3\,M_\odot$ are formed within $\sim 10^5$ yrs. As a result, stars are produced along outflow's path, endowed with the outflow speed at their formation site. These HVSs travel through the galactic halo and eventually escape into the intergalactic medium. The expected instantaneous rate of star formation inside the outflow is $\sim 4-5$ orders of magnitude greater than the average rate associated with previously proposed mechanisms for producing HVSs, such as the Hills mechanism and three-body interaction between a star and a black hole binary. We predict the spatial distribution of HVSs formed in AGN outflows for future observational probe.

6.1 Introduction

There is growing observational evidence for large scale outflows driven by active galactic nuclei (AGNs). Such outflows have been detected in nearby ultra luminous infrared galaxies (Cicone et al. 2014; Tombesi et al. 2015) as well as in broad absorption line quasars (Arav et al. 2015). Interestingly, cold molecular clumps are observed through their CO and HCN emission to co-exist with hot gas in outflows, forming a multi-phase medium in equilibrium (Cicone et al. 2014). Recent observations of a nearby galaxy revealed possible ongoing star formation inside a massive galactic outflow for the first time (Maiolino et al. 2017).

Previously, Silk et al. (2012) discussed the ejection of hypervelocity stars (HVSs) in the Galactic Center as a result of AGN jet interaction with a giant molecular cloud. In addition, it has been discussed that AGN outflows can trigger or enhance star formation by compressing pre-existing cold gas in the interstellar medium (ISM), such as Ishibashi & Fabian (2012, 2014); Nayakshin & Zubovas (2012); Silk (2013); Zubovas et al. (2013); Zubovas & Bourne (2017). Instead, we focus here on a different scenario of HVS production where the outflow material itself fragments into stars late in the hydrodynamical evolution of the outflow. Numerical simulations have identified the required physical conditions for the formation of molecular clumps in AGN outflows (Costa et al. 2015; Ferrara & Scannapieco 2016; Scannapieco 2017; Richings & Faucher-Giguère 2018), due to a thermal instability. The resulting distribution of stars could be substantially different from the previously considered scenario since stars are born with the outflow's speed in this case. Here we calculate cold clump formation in detail, and discuss the detailed properties and statistics of the resulting stellar population and spatial distribution, which has not been considered in the literature (e.g. Zubovas & King (2014); Zubovas & Bourne (2017)).

Over the past decade, dozens of HVSs have been detected in the halo of the Milky Way (MW) galaxy (Brown 2015). The fastest known stars have velocities $\sim 700\,\mathrm{km\,s^{-1}}$ at distances of $50 - 100$ kpc (Brown et al. 2014), which significantly exceed the escape speed of the MW halo. Unbound HVSs are distributed equally across Galactic latitude but appear clumped in Galactic longitude (Brown et al. 2009; Boubert & Evans 2016; Boubert et al. 2017). The spatial and velocity distribution of identified HVSs suggest a scenario of three-body exchange in which the supermassive black hole at the Galactic center (GC), Sgr A*, dissociates through its gravitational tide a binary star system and ejects one of its members as a HVS, in a process known as the Hills mechanism (Hills 1988; Brown 2015).

Here we verify that star formation in AGN outflows could lead to an alternative production channel of HVSs, at a rate of $\sim 10\,M_{\odot}\,\mathrm{yr}^{-1}$, consistent with the observed rate (Maiolino et al. 2017), which is $\sim 4-5$ orders of magnitude greater than the Hills mechanism (Hills 1988), as well as other previously considered processes, such as three-body interaction between a star and a binary black hole system (Yu & Tremaine 2003; Guillochon & Loeb 2015). We discuss formation of cold clumps via thermal instabilities in detail, and predict the spatial distribution of HVSs formed in AGN outflows for future observational probe, which has not been discussed in previous literature (e.g. Zubovas & King (2014)).

This chapter is organized as follows. In §6.2, we discuss the AGN outflow hydrodynamics and the formation of cold clumps. In §6.3, we discuss star formation within the outflow and predict the statistics of hypervelocity stars born in an AGN outflow. Finally, in §6.4 we summarize our results and discuss related observational implications.

6.2 Two-Phase Medium

6.2.1 Outflow Hydrodynamics

AGNs are believed to launch a fast wind from their inner accretion disk with a velocity of $\sim 0.1\,c$, where c is the speed of light (King & Pounds 2015). The wind drives a double shock structure, where the outer forward shock sweeps up the ambient medium while the inner reverse shock decelerates the wind itself. The two shocks are separated at a contact discontinuity. Here we follow the hydrodynamical model of outflow's outer boundary from our previous work (see Wang & Loeb (2015) for details). The continuous energy injection into the wind is assumed to last for a Salpeter time, $t_{\rm Sal} \sim 4.5 \times 10^7$

yrs, after which the AGN shuts off, assuming a radiative efficiency from accretion of $\sim 10\%$. We adopt a broken power-law radial density profile for the gas, $\rho_{\rm g}$, which follows an isothermal sphere and NFW profiles in the disk and halo components, respectively. Figure 6.1 shows the hydrodynamics of the outflows embedded in halos of $10^{11}, 10^{12}, 10^{13}\,M_\odot$. The speed of the outflowing shell, $v_{\rm s}$, rapidly declines to a few hundreds of $\rm km\,s^{-1}$ when it reaches the edge of the galactic disk and enters the halo. The outflow continues to propagate into the halo even after the energy injection from the AGN shuts off.

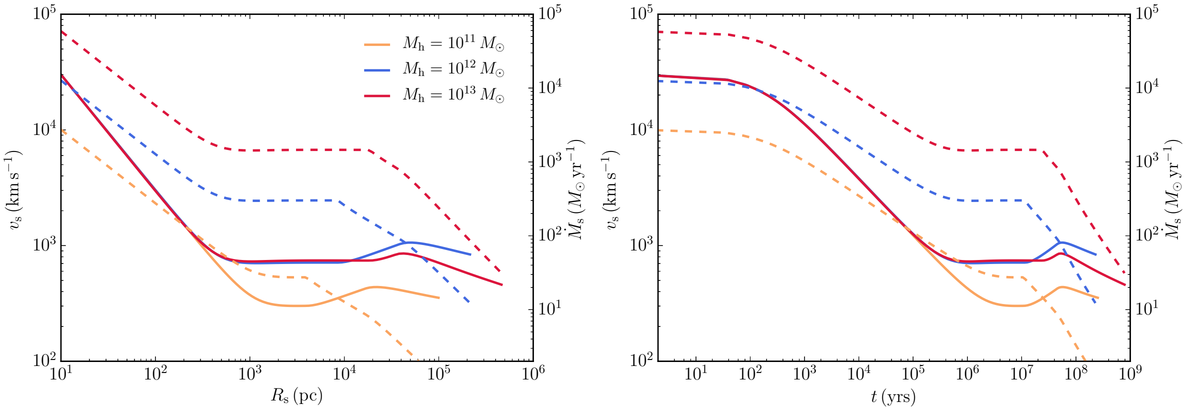

Figure 6.1 Hydrodynamics of AGN outflows embedded in halos of $M_{\rm h} = 10^{11}, 10^{12}, 10^{13}\,M_\odot$ (represented by orange, blue and red lines, respectively). In the left and right panels, we show the outflow speed, $v_{\rm s}$ (solid lines) and the interception rate of swept-up mass, $\dot{M}_{\rm s}$ (dashed lines), as functions of the outflow radius, $R_{\rm s}$ and time, t. The black hole mass, $M_\bullet$, and the gas density distribution are self-consistently determined by $M_{\rm h}$ and redshift z (see Wang & Loeb (2015) for details). For the outflow parameters of interest, we find that the outflow can reach the edge of the halo with a speed of $\gtrsim 300\,{\rm km\,s^{-1}}$ on a timescale of $\sim 10^8$ yrs.

6.2.2 Clump Formation

AGN outflows have been observed to be energy-conserving on large scales, where radiative cooling by the shocked wind is negligible (Tombesi et al. 2015), a result supported by theoretical models (Faucher-Giguère & Quataert 2012; King & Pounds 2015; Wang & Loeb 2015). We note that it is the cooling of the shocked wind, not the shocked ambient medium, that determines whether the outflow is energy or momentum-conserving. In analogy to supernova remnants, protons and electrons in the shocked wind region of AGN outflows can be significantly decoupled. The thermal energy carried by the protons is thus trapped in the shocked wind, leading to energy conservation. The final temperature of the plasma in the shocked wind region reaches $\sim 10^7$ K, and remains too hot for clump condensation (Faucher-Giguère & Quataert 2012). Previous simulations showed that during the dynamical transition between the momentum-driven and energy-driven phases, the shell is accelerated and fragmented by Rayleigh-Taylor instabilities, resulting in short-lived clumps entrained and ablated by hot gas flowing past them (Ferrara & Scannapieco 2016). Once the outflow becomes energy-conserving, the swept-up shell cools rapidly and condenses, with additional cold clumps formed via a thermal instability. These clumps are able to survive as they are nearly at rest with the hot tenuous gas surrounding them (Scannapieco 2017). Here we estimate the cooling timescale and final temperature of the clumps condensing out of the outflowing shell, and adopt prescriptions for the related heating and cooling functions (Sazonov et al. 2005; Koyama & Inutsuka 2002).

At $T \gtrsim 10^4$ K, the heating and cooling of the swept-up shell involves free-free emission, Compton heating/cooling, photoionization heating, line and recombination continuum cooling. We adopt numerical approximations for relevant heating and cooling curves from Sazonov et al. (2005) for optically thin gas illuminated by quasar radiation. At $T \lesssim 10^4$ K, the dominant cooling process includes atomic and molecular cooling. We adopt related prescriptions from Koyama & Inutsuka (2002) at solar metallicity:

$$\frac{\Lambda(T)}{\Gamma} = 10^7 \exp\left(-\frac{114800}{T+1000}\right) + 14\sqrt{T} \exp\left(-\frac{92}{T}\right) \ , \tag{6.1}$$

where $\Gamma = 2 \times 10^{-26}\,\mathrm{erg\,s^{-1}}$ and T is in units of K. The above formula includes the following processes: photoelectric heating from small grains and polycyclic aromatic hydrocarbons, heating and ionization by cosmic rays and X-rays, heating by H_2 formation and destruction, atomic line cooling from hydrogen Lyα, C II, O I, Fe II and Si II, rovibrational line cooling from H_2 and CO, and atomic and molecular collisions with dust grains at solar metallicity. The rate at which the energy density of the outflowing gas per unit volume changes due to the heating and cooling processes can be written as:

$$\dot{E} = H(n,T) - C(n,T) \ , \tag{6.2}$$

where $H(n,T)$ and $C(n,T)$ are the total heating and cooling functions, respectively. We numerically integrate the energy balance equation, starting from an initial temperature of the swept-up shell set by the Rankine-Hugoniot jump condition: $T_0 \approx 3\mu m_{\mathrm{p}} v_{\mathrm{s}}^2/16k_{\mathrm{B}} \approx 10^7\, v_{\mathrm{s},3}^2$ K, where $v_{\mathrm{s},3} = (v_{\mathrm{s}}/10^3\,\mathrm{km\,s^{-1}})$, $\mu = 0.5$ is the mean molecular weight of fully ionized gas, m_{p} is the proton mass and k_{B} is the Boltzmann constant.

As shown in Fig.6.2, we find that for a range of parameter values of interest, the swept-up shell can cool down to ~ 10 K on a timescale of $\lesssim 10^4$ yrs, approximately scaled as $t_{\mathrm{cool}} \sim 10^4\,(n/\mathrm{cm^{-3}})^{-1}$ yrs, which is much shorter than the dynamical timescale of the outflow, $t_{\mathrm{dyn}} \sim R_{\mathrm{s}}/v_{\mathrm{s}} \approx 10^7 R_{\mathrm{s},1}\, v_{\mathrm{s},3}\,\mathrm{yrs}$, where $R_{\mathrm{s},1} = (R_{\mathrm{s}}/10\,\mathrm{kpc})$. For comparison,

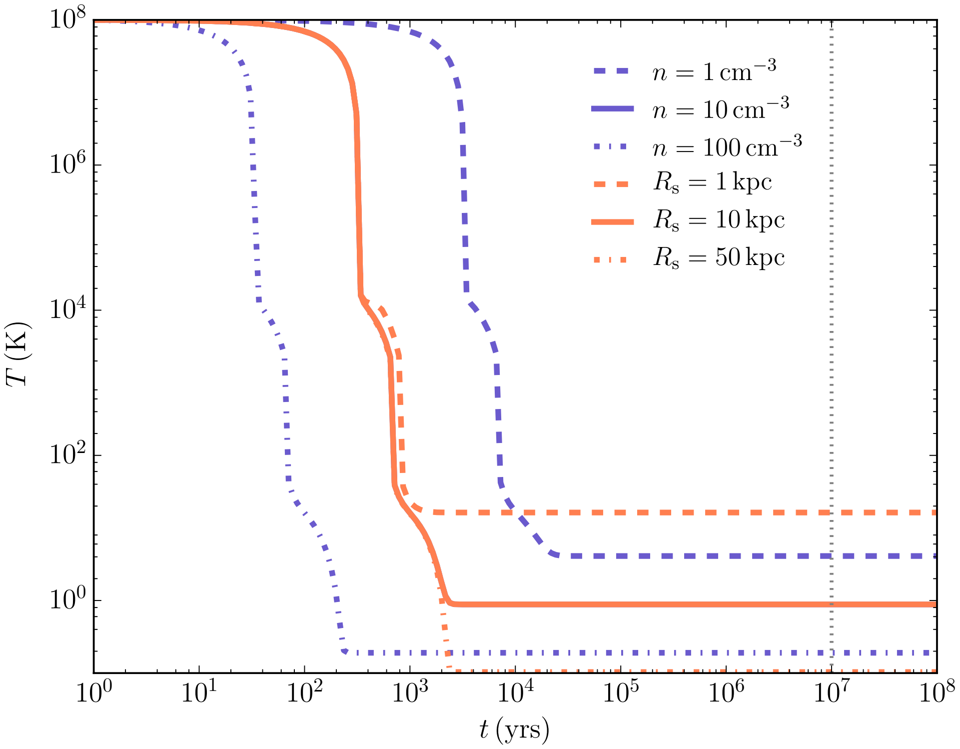

Figure 6.2 Temperature evolution of the swept-up gas shell. We integrate the heating and cooling function that includes free-free cooling, Compton heating/cooling, photoionization heating, line and recombination continuum cooling, and atomic and molecular cooling. The orange and purple lines show the temperature of the cooling gas as a function of time in a MW mass halo for different gas number density n and different outflow radii R_s. The AGN luminosity is fixed here to $\sim 10^{43}\,\mathrm{erg\,s^{-1}}$. The dotted grey line represents a characteristic outflow dynamical timescale, $t_\mathrm{dyn} \sim 10^7$ yrs.

the atomic and molecular cooling timescale is of order, $t_{\rm atm} \sim 3n_{\rm c}kt_{\rm cool}/\Lambda_{\rm atm} \approx 1.3 \times 10^{-3}\, n_{\rm c,0}\,{\rm yrs}$, where $n_{\rm c,0} = (n_{\rm c}/1\,{\rm cm}^{-3})$. $\Lambda_{\rm atm} \sim 10^{-25}\, n_{\rm c}^2\,{\rm erg\,s^{-1}cm^{-3}}$ is the cooling rate (Spitzer 1978). Thus, the shocked ambient gas cools efficiently to temperatures amenable to clump condensation and subsequent star formation. Thermal instability (TI) occurs if the heating rate at a constant pressure rises faster than the cooling rate (Field 1965). Material slightly cooler than the surrounding medium will keep cooling down at a constant pressure if the following condition holds (Beltrametti 1981):

$$\left[\frac{\partial}{\partial T}(H - C)\right]_p > 0\,. \tag{6.3}$$

We have verified that for $T \sim 10^4$ K and $n \sim 10^2\,{\rm cm}^{-3}$, the critical galactocentric distance above which the shell becomes thermally unstable is $r_{\rm c} \sim 1$ kpc. For $T \sim 10^4$ K and $n \sim 0.1\,{\rm cm}^{-3}$, $r_{\rm c} \sim 0.1$ kpc. Cold clumps condense out of the outflowing shell on a timescale much shorter than outflow's dynamical timescale. For a hot plasma with temperature of $T_{\rm h}$ and density $n_{\rm h}$, the minimum size of the cold clumps is constrained by thermal conductivity to the value (Beltrametti 1981):

$$l_{\rm TI} = \left(2\kappa_0 T_{\rm pl}/5c_0 n_{\rm pl}^2\right)^{1/2} = 33.2\, q_0^{1/2} T_{\rm h,7}^{3/2} n_{\rm h,1}^{-1}\,{\rm pc}\,, \tag{6.4}$$

where $T_{\rm h,7} = (T_{\rm h}/10^7\,{\rm K})$, $n_{\rm h,1} = (n_{\rm h}/10\,{\rm cm}^{-3})$, $\kappa_0 = 2 \times 10^{12} q_0 T_{\rm h,7}^{5/2}$ is the thermal conductivity, and $q_0 = 1 + 0.0015\ln(T_{\rm h,7}/n_{\rm h,1})$. We adopt $q_0 \approx 1$ in the calculation. The Bremsstrahlung coefficient is $c_0 = 7.6 \times 10^{-24}\, T_{\rm h,7}^{1/2}\,{\rm ergs\,cm^3\,s^{-1}}$. For clumps of size $\lesssim l_{\rm TI}$, thermal conduction will efficiently transport heat to prevent the growth of TI. The corresponding lower limit of gas mass enclosed in $l_{\rm cl}$ can be written as:

$$M_{\rm TI} = \left(\frac{4\pi}{3}\right) l_{\rm TI}^3\, n_{\rm h} m_{\rm p} = 3.5 \times 10^4\, T_{\rm h,7}^{9/2} n_{\rm h,1}^{-2}\, M_\odot \tag{6.5}$$

During clump contraction, the size and density of the resulting clumps can be estimated from mass conservation $n_{\rm cl}R_{\rm cl}^3 = n_{\rm h}l_{\rm TI}^3$ and pressure balance $n_{\rm cl}T_{\rm cl} = n_{\rm h}T_{\rm h}$, yielding:

$$R_{\rm cl} \approx 0.33\, T_{\rm cl,1}^{1/3} T_{\rm h,7}^{7/6} n_{\rm h,1}^{-1}\, {\rm pc}\ , \tag{6.6}$$

where $T_{\rm cl,1} = (T_{\rm cl}/10{\rm K})$ is the temperature of the cold clumps, and

$$n_{\rm cl} \approx 10^7 T_{\rm cl,1} T_{\rm h,7} n_{\rm h,1}\, {\rm cm}^{-3}\ . \tag{6.7}$$

The timescale of clump contraction driven by the surrounding medium can be obtained from:

$$t_{\rm shrink} \sim l_{\rm TI}/c_{\rm s} \approx 10^5 T_{\rm h,7} n_{\rm h,1}^{-1}\, {\rm yrs}\ , \tag{6.8}$$

where $c_{\rm s}$ is the adiabatic sound speed. We find that $t_{\rm shrink}$ is significantly longer than the cooling timescale, $t_{\rm cool}$, but much shorter than outflow's dynamical timescale, $t_{\rm dyn}$. Thus, the TI-formed clumps contract to reach their minimum size, determined by either thermal pressure or turbulent pressure. An additional constraint on the size of the TI-formed clumps is associated with the tidal force from mass within outflow's radius, $R_{\rm s}$. The corresponding clump size can be expressed as:

$$l_{\rm tid} = \left(\frac{M_{\rm TI}}{M_\star}\right)^{1/3} R_{\rm s} = 10.2 \left(\frac{M_{\rm TI,4}}{M_{\star,10}}\right)^{1/3} R_{\rm s,kpc}\, {\rm pc}\ , \tag{6.9}$$

where $M_{\rm TI,4} = (M_{\rm TI}/10^4\, M_\odot)$, $M_{\star,10} = (M_\star/10^{10}\, M_\odot)$ and $R_{\rm s,kpc} = (R_{\rm s}/{\rm kpc})$. For $M_{\rm TI} \sim 3.5\times 10^4\, M_\odot$, $l_{\rm tid} \approx 15.5\,{\rm pc} \sim l_{\rm TI}$, indicating that the clumps can survive the potential of galactic bulge. We note that the magnetic field in the ISM could modify both the amplitude and morphology of thermal instability. Recent numerical simulations show that magnetic tension suppresses buoyant oscillations of condensing gas, thus enhancing thermal instability (Ji et al. 2018). The density fluctuation amplitude scales as $\delta\rho/\rho \propto \beta^{-1/2}$, where β is the ratio between thermal and magnetic pressure, independent of the magnetic field orientation (Ji et al. 2018). Therefore, the scale constraints of the TI-induced clouds estimated here provide a lower limit on the growth of the clouds.

6.3 Hypervelocity Stars

6.3.1 Star Formation

Clumps with a mass $M_{\rm cl} \sim M_{\rm TI} \approx 3.5 \times 10^4\, T_{\rm h,7}^{9/2} n_{\rm h,1}^{-2}\, M_\odot$ and size $R_{\rm cl} \approx 0.33 T_{\rm cl,1}^{1/3} T_{\rm h,7}^{7/6} n_{\rm h,1}^{-1}$ pc, are formed in the shocked swept-up shell via TI. A detailed description of assembly of clumps requires distribution function in the galactic potential (e.g., Larson (1969)), which goes beyond the scope of this chapter. Here we focus on the total numbers of stars formed in the outflow and the corresponding star formation rate.

The cold clumps could be supported by turbulence with velocity dispersion $\sigma_\star = 21.6\, \alpha_\star T_{\rm cl,1}^{-1/6}\, T_{\rm h,7}^{5/3} n_{\rm h,1}^{-1/2}\, {\rm km\,s^{-1}}$ (McKee & Ostriker 2007), where $\alpha_\star \sim 1$. In comparison, the adiabatic sound speed $c_{\rm s} = 0.3 T_{\rm cl,1}^{1/2}\, {\rm km\,s^{-1}}$. We calculate the corresponding Jeans mass, $M_{\rm J}$, which is the minimum mass to initiate gravitational collapse of the cloud, given by (see, e.g. McKee & Ostriker (2007)):

$$M_{\rm J} = \left(\frac{3\pi^5}{32 G^3 m_{\rm p}}\right)^{1/2} \sigma_\star^3\, n_{\rm cl}^{-1/2} \approx 3 \times 10^5\, T_{\rm cl,1}^{-1}\, T_{\rm h,7}^{9/2}\, n_{\rm h,1}^{-4}\, M_\odot\ . \tag{6.10}$$

Comparing Eq.6.5 and Eq.6.10, we have verified that $M_{\rm cl} \sim 10\, M_{\rm J}$, indicating that TI-induced clouds collapse to form stars rapidly on a free-fall timescale much shorter than outflow's dynamical timescale $t_{\rm dyn}$, $t_{\rm ff} \sim (G\rho)^{-1/2} \sim 3 \times 10^4\, n_{\rm cl,7}^{-1/2}$ yrs, where $n_{\rm cl,7} = (n_{\rm cl}/10^7\, {\rm cm^{-3}})$. The stars are deposited at the outflow speed nearly at rest along the outflow's path. We assume that a fraction of the swept-up mass cools into form clumps and stars: $\dot{M}_\star \sim f_\star \dot{M}_{\rm s}$. The global star formation efficiency per dynamical time is often inferred to be around $\sim 1 - 10\%$ (Kennicutt 1998; Silk 2013; Somerville & Davé 2015), and so we adopt a total value of $f_\star \sim 10\%$ in the calculation. In Fig.6.1, we find that the interception rate of swept-up mass by the outflowing shell for a MW mass halo, $\dot{M}_{\rm s} \sim 10 - 100\, M_{\odot}\, {\rm yr}^{-1}$, corresponds to a star formation rate of $\sim 1 - 10\, M_{\odot}\, {\rm yr}^{-1}$, consistent with the recent observation of star formation within an AGN outflow (Maiolino et al. 2017). For halos of masses $\sim 10^{11}\, M_{\odot}$, the estimated star formation rate drops to $\sim 0.1 - 1\, M_{\odot}\, {\rm yr}^{-1}$, while for halos of masses $\sim 10^{13}\, M_{\odot}$, the expected star formation rate increases to $\sim 10 - 100\, M_{\odot}\, {\rm yr}^{-1}$. The speed distribution of the newly born stars resembles the velocity profile of the outflowing shell, as shown in Fig.6.1. Near the outer boundary of the galactic halo at ~ 100 kpc, the speeds of these stars exceed a few hundreds ${\rm km\, s}^{-1}$, making them potential HVSs. A fraction of these stars are unbound to the host galaxy.

6.3.2 Statistics

We divide the outflow's passage throughout the halo into a sets of shells of logarithmically equal width. The number of stars produced per unit logarithmic radius in the outflow can be written as:

$$\frac{dN_{\star}}{d\ln R_{\rm s}} = \frac{1}{\langle M_{\star} \rangle} \frac{\dot{M}_{\rm s} R_{\rm s}}{v_{\rm s}} \ , \tag{6.11}$$

where $\langle M_{\star} \rangle$ is the average stellar mass derived from the Salpeter mass function, given by $\langle M_{\star} \rangle = [(1-\beta)(1-s^{2-\beta})/(2-\beta)(1-s^{1-\beta})]\, M_{\star,{\rm min}}$, where $s = M_{\star,{\rm max}}/M_{\star,{\rm min}}$, $M_{\star,{\rm min}} = M_{\odot}$ and $M_{\star,{\rm max}} = \infty$ are the minimum and maximum masses of stars, respectively. For $\beta = 2.35$, $\langle M_{\star} \rangle \approx 3.85\, M_{\odot}$. We calculate the cumulative number of stars deposited in each shell at a given snapshot, shown in Fig.6.3. The lifetime of a main-sequence star can be simply expressed as (Meurs & van den Heuvel 1989):

$$\tau_{\rm ms} = 10^{\alpha} \left(\frac{M_{\star}}{M_{\odot}} \right)^{\beta} \ , \tag{6.12}$$

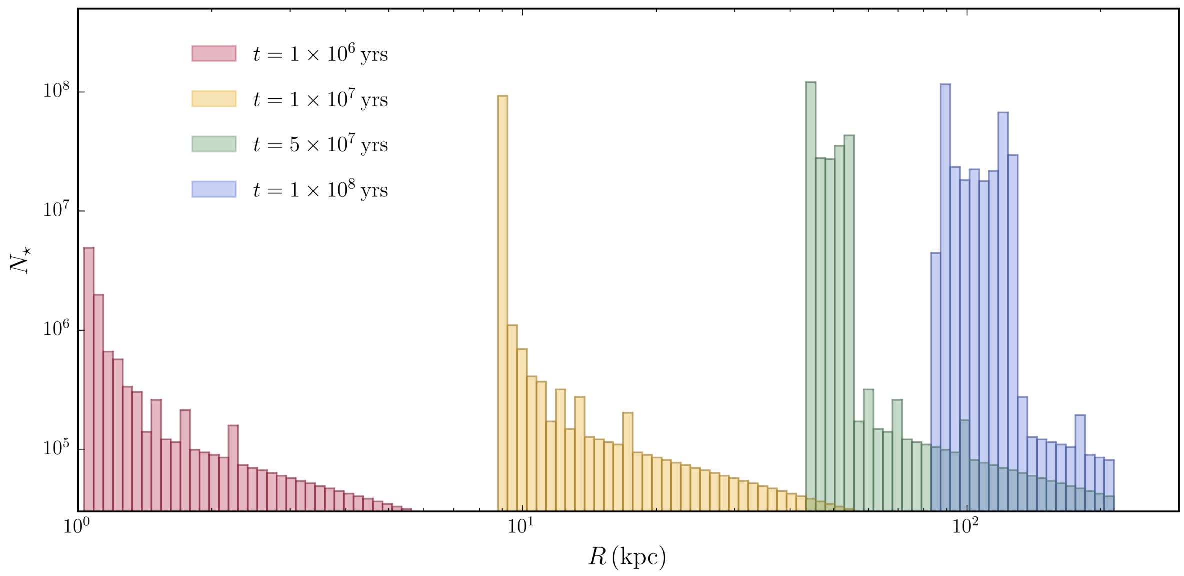

Figure 6.3 Cumulative number of stars in shells deposited along the outflow's path. We divide the outflow into 150 logarithmically spaced shells and count the total number of stars found in each shell at a given time. The red, orange, green and blue colors reflect the time elapsed since the outflow has launched. We assume a star formation efficiency of $f_\star \sim 10\%$. Stars are deposited with the speed of the outflow at the radial location and time of their birth. Stars produced at early times could move ahead of stars produced later on in the outflowing shell.

where $\alpha = 10.03$, $\beta = -4$ for $M_\star < 1.5M_\odot$, $\alpha = 9.86$, $\beta = -3$ for $1.5M_\odot \leq M_\star < 3.8M_\odot$, $\alpha = 9.28$, $\beta = -2$ for $3.8M_\odot \leq M_\star < 12M_\odot$ and $\alpha = 8.20$, $\beta = -1$ for $M_\star > 12\,M_\odot$. We have verified that stars of mass $\lesssim 2M_\odot$ will remain as main-sequence stars as the outflow reaches the edge of the halo. Stars of mass $M_\star \gtrsim 10M_\odot$ leave the main-sequence within the outflow's dynamical timescale, $t_{\rm dyn}$. The observed HVSs in the MW halo are massive B-type stars that are short-lived on main-sequence with lifetimes $\lesssim 10^8$ yrs (Brown et al. 2014). These stars fade at later times. We estimate that $\sim 10^7 - 10^8$ HVSs are produced per MW galaxy during its entire lifetime.

During AGN periods, the predicted instantaneous HVS formation rate is $\sim 1 - 10\,M_\odot\,{\rm yr}^{-1}$, which is 4-5 orders of magnitude greater than the time-averaged rate of producing HVS via tidal breakup of binary stars (Hills 1988) or three-body interaction between a star and a binary black hole (Yu & Tremaine 2003; Guillochon & Loeb 2015). Since the lifetime of bright AGN is of order a percent of the age of the Universe (e.g. Martini (2004)), the net production of HVS by AGN exceeds that from other mechanisms by several orders of magnitude, even when taking account of their short duty cycle.

6.4 Summary & Discussion

In this chapter, we studied star formation in AGN outflows as a new mechanism for HVS production. This possible channel for star formation is suggested by recent observations (Maiolino et al. 2017). We showed that the shocked ambient medium cools quickly and condenses to form cold clumps embedded in a hot tenuous gas via a thermal instability. Stars are deposited along outflow's path at the local outflow speed. We find that at a distance of $\sim 50 - 100$ kpc, stars are ejected with a speed of $\gtrsim 500\,{\rm km\,s^{-1}}$

at a rate of $\sim 1 - 10\, M_{\odot}\, \mathrm{yr}^{-1}$, assuming a star formation efficiency of $\sim 10\%$. Such a speed distribution is consistent with the HVS population in the MW halo (Brown 2015). During active periods of AGN outflows, the estimated HVS production rate is 4-5 orders greater than the rate predicted by other mechanisms. We note that a more precise estimation requires a more realistic outflow geometry, which is beyond the scope of this work. However, a spherically symmetric outflow model adopted here produces hydrodynamic results consistent with observations of molecular outflows (Cicone et al. 2014; Tombesi et al. 2015).

The discovery of Fermi bubbles suggests that Sgr A* was recently active (Su et al. 2010). Our model predicts significant HVSs production from an outflow driven by such an AGN activity. The observed B-type HVSs have lifetimes $\approx 10^8$ yrs, which suggests that Sgr A* could have been active $\sim 10^8$ yrs ago. Stars formed during AGN episodes will be challenging to identify as they fade and travel to greater distances. Recent IFU observations on local Seyfert galaxies with strong outflows revealed complicated gas structure and dynamics at $\sim$ kpc scales (Karouzos et al. 2016). Searches for HVSs in these galaxies could be promising provided that the local ionizing source of star formation dominates over AGNs, which can be justified by BPT diagram of emission line ratios (Baldwin et al. 1981).

Stars born at early times during the outflow history travel faster than those formed at later times. Thus, a large-scale double shell structure could appear, in which the outer shell consists of stars formed earlier while the inner shell contains stars formed later. Outflows could also lead to the appearance of ring galaxies (Macciò et al. 2006) by clearing out halo gas (Zubovas & King 2012) and producing a bright shell of stars at a large distance. The shape of these configurations would reflect the three-dimensional geometry of the outflow. Star formation rings are also predicted in cases where clouds are stationary before being struck by AGN winds, such as clumps within clouds struck by winds (Zubovas & King 2014; Dugan et al. 2017), clumps with high-velocity gas caused by the compression of the clouds from the outflow (Cresci et al. 2015), and stars formed in giant molecular clouds within AGN winds (Tremblay et al. 2016). The resulting stellar distribution from those scenarios is different from the scenario we discuss where the resulting stellar population have the speeds of the outflow at birth.

Acknowledgements

We thank Warren Brown and James Guillochon for insightful comments on the manuscript. This work was supported in part by the Black Hole Initiative, which is funded by a grant from the John Templeton Foundation.

Chapter 7

Self-Sustaining Star Formation Fronts in Filaments During Cosmic Dawn

This thesis chapter originally appeared in the literature as

X. Wang & A. Loeb, Self-Sustaining Star Formation Fronts in Filaments During Cosmic Dawn, *the Astrophysical Journal Letters*, 862, L14 (2018)

Abstract

We propose a new model for the ignition of star formation in low-mass halos by a self-sustaining shock front in cosmic filaments at high redshifts. The gaseous fuel for star formation resides in low mass halos which can not cool on their own due to their primordial composition and low virial temperatures. We show that star formation can

be triggered in these filaments by a passing shock wave. The shells swept-up by the shock cool and fragment into cold clumps that form massive stars via thermal instability on a timescale shorter than the front's dynamical timescale. The shock, in turn, is self-sustained by energy injection from supernova explosions. The star formation front is analogous to a detonation wave, which drives exothermic reactions powering the shock. We find that sustained star formation would typically propel the front to a speed of $\sim 300 - 700\,\mathrm{km\,s^{-1}}$ during the epoch of reionization. Future observations by the *James Webb Space Telescope* could reveal the illuminated regions of cosmic filaments, and constrain the initial mass function of stars in them.

7.1 Introduction

The gas reservoir of low-mass halos at high redshifts exhibits inefficient star formation due to the lack of metals, which are essential for the transition from intermediate temperature atomic gas to cold molecular gas (Krumholz & Dekel 2012; Loeb & Furlanetto 2013). Nevertheless, a significant population of star-forming galaxies beyond $z \gtrsim 10$ is required to explain the Thomson optical depth of the cosmic microwave background (Finkelstein et al. 2015; Robertson et al. 2015). A likely compensating factor for the shortage of ionizing photons is a population of faint low-mass halos (Bouwens et al. 2012; Anderson et al. 2017), observationally suggested by the steep faint end slope of the UV luminosity function (Finkelstein et al. 2015; Anderson et al. 2017). The process by which efficient star formation is initiated in low-mass halos at high redshifts is still unknown, given the inefficient star formation rate (SFR) observed in low-mass halos at low redshifts (Behroozi et al. 2013). Therefore, it is important to probe the SFR in low-mass halos during the epoch of reionization through future observations with the *James Webb Space Telescope* (*JWST*).

Galactic outflows play an important role in the formation and evolution of low-mass galaxies (e.g. Dekel & Silk 1986; Peeples & Shankar 2011), as well as in regulating star formation (Silk 1997; Hopkins et al. 2011) and the enrichment of circumgalactic and intergalactic medium (Furlanetto & Loeb 2003). Cold molecular clouds are identified in observations of such outflows (Rupke et al. 2005; Sturm et al. 2011). Numerical simulations have shown that outflowing shells tend to fragment through a thermal instability (Thompson et al. 2016; Ferrara & Scannapieco 2016; Scannapieco 2017; Schneider et al. 2018), which may lead to subsequent star formation within the outflows (Silk 2013; Zubovas & King 2014; Maiolino et al. 2017; Wang & Loeb 2018). However, previous studies of galactic outflows were limited to the scale of the host galaxy and the surrounding circumgalactic and intergalactic medium. How these outflows may affect their neighboring halos remained unclear.

In this chapter, we propose a new model for the ignition of star formation in low-mass halos that otherwise do not form stars. Such halos are often distributed in filaments. A passing shock could trigger star formation and generate a self-sustaining starburst front. We make an analogy between this process and the propagation of a detonation wave, in that the gas reservoir of low-mass halos is analogous to gunpowder, and the burning front triggers new star formation while being dynamically maintained by the energy release from supernovae (SNe). The chapter is organized as follows. In §7.2, we describe our model in analogy to detonation wave theory. In §7.3, we calculate the propagation of the star formation front and present numerical results. Finally, §7.4 summarizes our main results and observational implications.

7.2 Star Formation Front

The gas reservoir of low-mass halos can not initiate star formation on its own and remains quiescent if the virial temperature of the halo, $T_{\rm vir}$, is below the cooling threshold temperature, $t_{\rm cool}$. For primordial gas composition, the cooling threshold can be at minimum $t_{\rm cool} = 200$ K for molecular hydrogen, H_2 (below which molecular transitions are not excited) or $t_{\rm cool} = 10^4$ K for atomic hydrogen, H I, if H_2 is dissociated by a UV background (see review in chapter 6 of Loeb & Furlanetto 2013). Prior to star formation and feedback, sufficient baryons have been assembled into these halos as their virial masses exceed the cosmological Jeans (filtering) mass at $z \gtrsim 20$ (Haiman et al. 1996). The halos experience a gas-poor phase when feedback partially removes the gas, but recover a gas-rich phase when the gas accretes back from the IGM. The recycling of baryons results in an average baryon fraction which is $\sim 50\%$ of the cosmic average in halos of masses $\sim 10^7\,M_\odot$, with a lower fraction in lower-mass halos (Chen et al. 2014; Wise et al. 2014). However, during gas-rich phases, halos maintain a baryon fraction that is approximately the cosmic average (Chen et al. 2014). The average separation of halos with $T_{\rm vir}$ in the range of $\sim 0.5 - 1.0\ t_{\rm cool}$ is $\bar{l} \approx (4\pi n/3)^{-1/3}/(1+z)$, where n is the comoving number density of dark matter halos as derived from the halo mass function (Press & Schechter 1974; Sheth & Tormen 1999) . In cosmic filaments, halos are found to be closer together (Bond et al. 1996; Mo et al. 2010), with $\bar{l}$ smaller by up to a factor of ~ 10. Figure 7.1 shows that $\bar{l}$ is a few times $R_{\rm vir}$, and should shrink to $\sim R_{\rm vir}$ inside filaments. Thus, we assume that halos are contiguous with their neighbors, tightly packed along the filament.

A galactic outflow driven by active galactic nuclei or SN would propagate

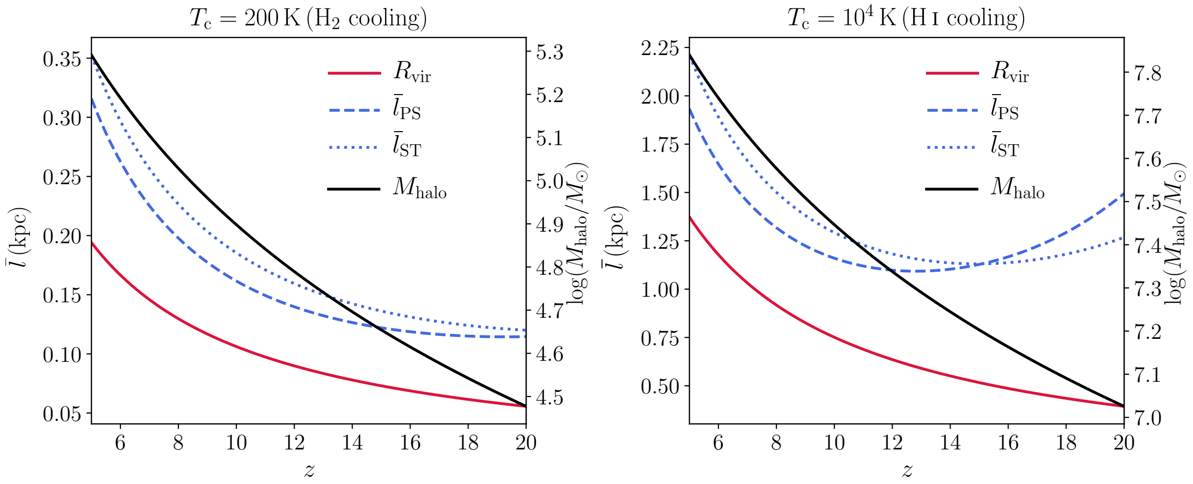

Figure 7.1 Comparison of the average separation of halos with $T_{\rm vir} = 0.5 - 1.0\,t_{\rm cool}$, and their $R_{\rm vir}$, in cosmic filaments. Two panels show the cases of H_2 and HI cooling thresholds, respectively. The red solid lines represent $R_{\rm vir}$, while the dashed and dotted blue lines correspond to the average separation estimated from the Press-Schechter (Press & Schechter 1974) and Sheth-Tormen (Sheth & Tormen 1999) halo mass functions, respectively (~ 10 times more compact in filaments). The black lines provide the halo mass, $M_{\rm halo}$, whose $T_{\rm vir}$ is just below $t_{\rm cool}$, with the scale labeled on the right-hand vertical axes. This implies that halos just below $t_{\rm cool}$ are tightly packed in filaments at high redshifts.

supersonically and sweeps up the ambient medium with a speed of hundreds of $\mathrm{km\,s^{-1}}$, as based on observations and theoretical calculations (e.g. King & Pounds 2015; Wang & Loeb 2015). The shells swept-up by the outflow tend to cool rapidly and fragment into cold clumps that subsequently form stars (Zubovas & King 2014; Scannapieco 2017; Wang & Loeb 2018). The outflow shock is rejuvenated as it gains energy from new SN explosions which sustain its propagation. Hence, star formation can be ignited by the front as it passes through the filament. The configuration of such a burning front of star formation is shown in Fig. 7.2. The propagation of this self-sustaining shock is analogous to a detonation wave, which involves an igniting shock self-sustained by an exothermal chemical process (Fickett & Davis 1979).

7.2.1 Detonation Model

The reactive Euler equations of high-speed flows coupled to energy release can be used to describe the propagation of star formation fronts, in analogy to detonation waves. These equations are,

$$\frac{D\rho}{Dt} + \rho\nabla\cdot\boldsymbol{v} = 0 \tag{7.1a}$$

$$\rho\frac{D\boldsymbol{v}}{Dt} = -\nabla p \tag{7.1b}$$

$$\frac{De}{Dt} - \frac{p}{\rho^2}\frac{D\rho}{Dt} = 0 \tag{7.1c}$$

$$\frac{D\lambda}{Dt} = W \tag{7.1d}$$

where $D/Dt = \partial/\partial t + \boldsymbol{v}\cdot\nabla$ is the full time derivatives of the flow. In a steady-state, $\partial/\partial t = 0$ in the rest frame of the detonation wave. Throughout our discussion, $\boldsymbol{v}$, ρ and p are the velocity, density and pressure of the flow, respectively; e is the internal

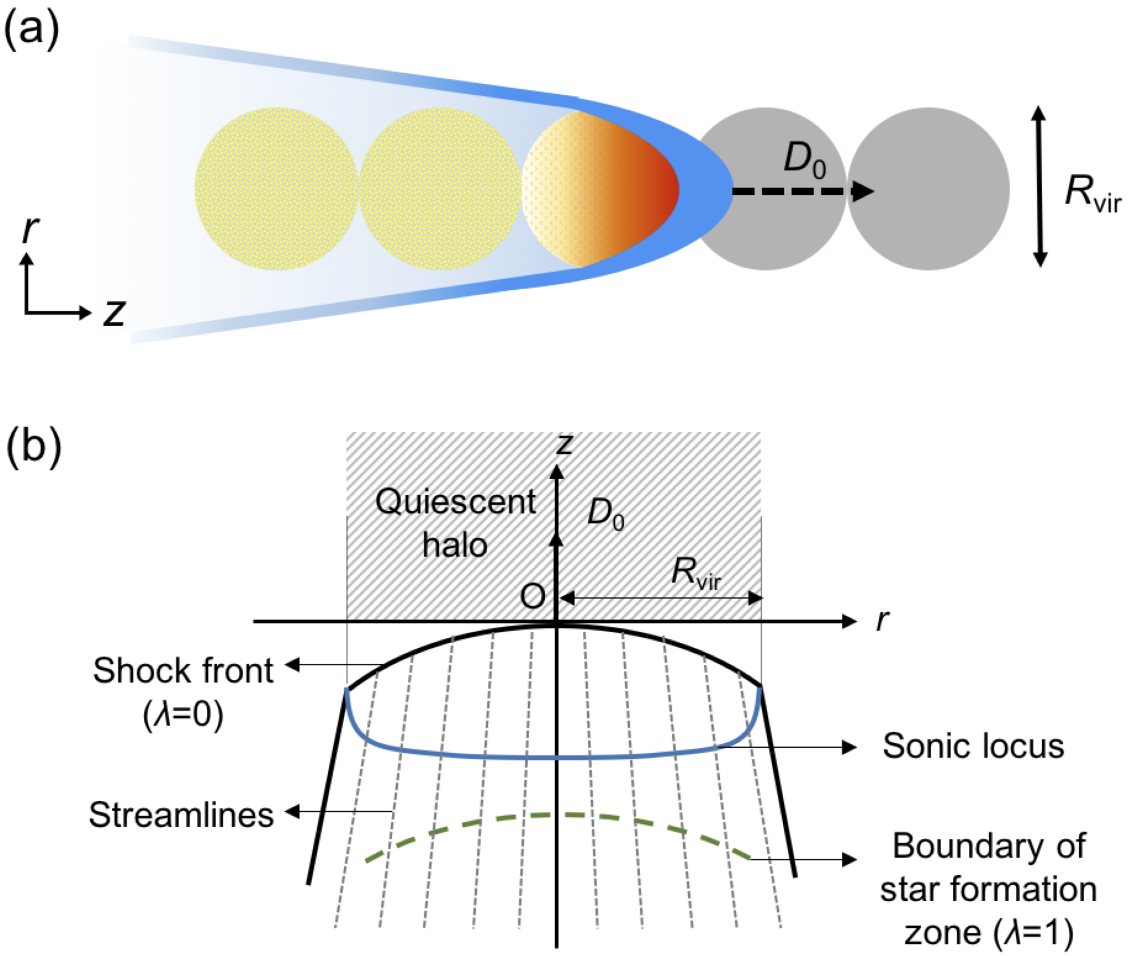

Figure 7.2 Configuration of a star formation front. Panel (a) sketches the burning front sweeping through halos packed in a filament that can not form stars before the passage of the shock, analogous to a self-propagating detonation wave in gunpowder. The width of the filament is $\sim R_{\rm vir}$. Panel (b) shows the schematic diagram of a two-dimensional cylindrical detonation wave. The blue solid line represents the sonic locus, where the Chapman-Jouguet (CJ) condition is satisfied. The green dashed line shows the boundary of the star formation zone, behind which SF had completed. The grey dotted lines correspond to the streamlines of post-shock flows, which are assumed to be straight but diverging (see Appendix for details). Ahead of the detonation shock front lies the unburnt fuel of low-mass halos, in which stars can not form until the shock's passage.

energy per unit mass; $\lambda = \rho_\star/(\rho_\star + \rho_{\rm g})$ is the stellar mass fraction; and $\rho_\star$ and $\rho_{\rm g}$ are the stellar and gas density, respectively. The location where $\lambda = 0$ corresponds to the detonation shock front, whereas $\lambda = 1$ corresponds to the completion of star formation. We approximate the fuel distribution as uniform, i.e. smooth over the scale of individual halos when describing the global propagation of the front. This approach is similar to the description of detonation waves in gunpowder, which involves smoothing over the scale of individual grains in the fuel. We adopt the polytropic equation of state:

$$e = \frac{p}{(\gamma - 1)\rho} - Q\lambda \ , \tag{7.2}$$

where $\gamma = 5/3$ is the polytropic index. Here Q is the energy release from SN explosions per unit mass of gas:

$$Q = \frac{q_{\rm IMF} f_{\rm SN} E_{\rm SN}}{\omega_{\rm SN}} \ , \tag{7.3}$$

where $E_{\rm SN}$ is the energy released by each SN, $\omega_{\rm SN}$ is the total amount of stellar mass that must be formed in order to produce one SN. For a very massive initial mass function (IMF), $E_{\rm SN} = 10^{52}$ ergs and $\omega_{\rm SN} = 462\,M_\odot$ (Furlanetto & Loeb 2003). The coefficient $f_{\rm SN} \sim 0.25$ is the fraction of the energy produced by SN to power the wind while the rest is lost mainly to radiative cooling (e.g, Mori et al. 2002).

The parameter $q_{\rm IMF}$ quantifies a deviation of the IMF from Pop III stars. In Eq. (7.1d), $W \equiv d\lambda/dt$ denotes the SFR, derived from the Kennicutt-Schmidt (KS) law (Kennicutt 1998) and converted to the volume density of SFR (Schaye & Dalla Vecchia 2008):

$$\dot{\rho_\star} = A'(1\,M_\odot\,{\rm pc}^{-2})^{-n'} \left[\frac{\gamma}{G}(1-\lambda)p\right]^{(n'-1)/2} \rho_{\rm g} \ , \tag{7.4}$$

where G is Newton's constant; $A' = (2.5 \pm 0.7) \times 10^{-4}$ and $n' = (1.4 \pm 0.15)$ are the normalization constant and power-law index in KS law for surface density. Thus,

$$W = \epsilon_\star \frac{\dot{\rho}_\star}{\rho_\star + \rho_{\rm g}} = \epsilon_\star A p^n (1-\lambda)^m \ , \tag{7.5}$$

where A is a normalization constant. We adopt $n' = 1.5$ and derive the power-law indices $n = 0.25$ and $m = 1.25$. Here, $\epsilon_\star$ is a correction factor for the formation rate of Pop III stars which could be different from KS law due to their low metallicity (Trenti & Stiavelli 2009). The fiducial values of free parameters are: $f_{\rm SN} = 0.25$, $q_{\rm IMF} = 1.0$, $\epsilon_\star = 1.0$, $E_{\rm SN} = 10^{52}$ erg, $\omega_{\rm SN} = 462\,M_\odot$, $m = 1.25$ and $n = 0.25$.

To solve Eqs. (7.1a)-(7.1d), we follow the semi-analytical approach from Watt et al. (2012) (see Appendix for details). In particular, we find that the average steady-state detonation speed, D_0, decreases as $R_{\rm vir}$ decreases, or equivalently, as z increases, as shown in Fig. 7.3. The star formation front travels with a speed of $D_0 \sim 200 - 400\,{\rm km\,s^{-1}}$ at the beginning of reionization ($z \sim 30$), and $D_0 \sim 300 - 600\,{\rm km\,s^{-1}}$ at the end of reionization ($z \sim 6$). We show that D_0 is a fraction, $\sim 0.2 - 0.7$ of the idealized one dimensional detonation speed, $D_{\rm CJ} = [2(\gamma^2-1)Q]^{1/2} \approx 1000\,{\rm km\,s^{-1}}$, for the free parameters set at their fiducial values. The significant deviation from a one-dimensional solution indicates that lateral expansion and energy losses along radial direction are non-negligible, particularly for high-redshift halos with a smaller $R_{\rm vir}$.

7.2.2 Star Formation

Next, we follow the prescription of our previously derived model for star formation within shells (Wang & Loeb 2018). The swept-up gas cools and fragments into cold clumps embedded in a hot tenuous gas via a thermal instability, which occurs if the heating rate at a constant pressure rises faster than the cooling rate as a function of temperature,

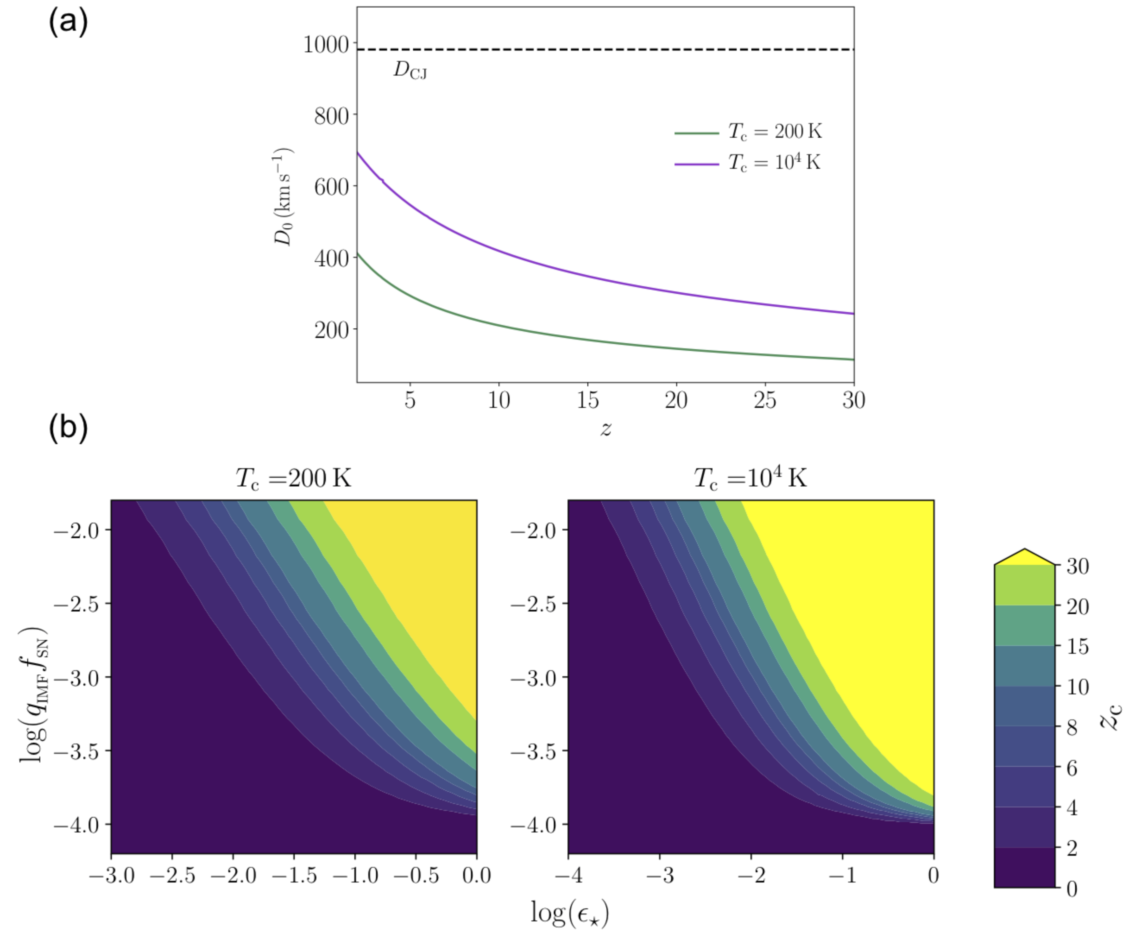

Figure 7.3 Panel (a) shows the average detonation speed, D_0, as a function of z, for $t_{\rm cool} = 200$ K (green) and 10^4 K (purple). The dashed line represents the ideal CJ speed, $D_{\rm CJ} \approx 10^3\,{\rm km\,s^{-1}}$. Model parameters are taken to be their fiducial values. Panel (b) represents the critical redshift of detonation failure, $z_{\rm c}$, as a function of model parameters $\epsilon_\star$, $q_{\rm IMF}$, $f_{\rm SN}$. We show contours of the $z_{\rm c}$, beyond which the detonation fails, for $t_{\rm cool} = 200$ K (left) and $t_{\rm cool} = 10^4$ K (right). The horizontal and vertical axes span different values of $\epsilon_\star$ and the product of $q_{\rm IMF}$ and $f_{\rm SN}$, respectively. We fix other parameters to their fiducial values. The color bar indicates $z_{\rm c}$.

consistent with observations (Maiolino et al. 2017) and numerical simulations (Ferrara & Scannapieco 2016; Schneider et al. 2018). The cooler gas continues to condense at a constant pressure, leading to the formation of a two-phase medium (Field 1965; Silk 2013; Zubovas & King 2014; Inoue & Omukai 2015). The cooling timescale of the swept-up gas can be estimated as $t_{\rm cool} \approx 3.3 \times 10^3\, n_1^{-1} T_4 \Lambda_{-23}^{-1}(T,Z)$ yrs, where $n_1 = (n_{\rm s}/1\,{\rm cm}^{-3})$ is the number density of post-shock gas, $T_4 = (T_{\rm s}/10^4\,{\rm K})$ is the post shock gas temperature, $\Lambda_{-23} = (\Lambda/10^{-23}\,{\rm erg\,cm^3\,s^{-1}})$ is the cooling function, and Z is the metallicity (e.g. Maio et al. 2007; Arata et al. 2018). For halos of mass $\sim 10^8\,M_\odot$ and size ~ 0.5 kpc, the characteristic shocked gas density at redshift $z \sim 10$ is $n_{\rm s} \sim 10\,{\rm cm}^{-3}$. For $Z \lesssim 10^{-2} Z_\odot$, where $Z_\odot$ denotes solar metallicity, Λ_{-23} is in the range $10^{-3} - 0.1$, approximately scaling as $\sim (Z/Z_\odot)$ (Sutherland & Dopita 1993; Maio et al. 2007; Inoue & Omukai 2015). Thus, $t_{\rm cool}$ is much shorter than the dynamical timescale of the flow, $t_{\rm dyn} \sim R_{\rm vir}/D_0 \sim 10^7$ yrs. The characteristic mass and size of the clouds induced by the thermal instability can be estimated as $M_{\rm cl} \sim 110\, T_{\rm h,6}^{9/2} n_{\rm h,0}^{-2}\, M_\odot$ and $R_{\rm cl} \sim 0.22\, T_{\rm cl,1}^{1/3} T_{\rm h,6}^{7/6} n_{\rm h,0}^{-1}$ pc (Field 1965; Wang & Loeb 2018), where $T_{\rm h,6} = (T_{\rm h}/10^6\,{\rm K})$ and $n_{\rm h,0} = (n_{\rm h}/1\,{\rm cm}^{-3})$ are the temperature and number density of the hot medium embedding the clouds, and $T_{\rm cl,1} = (T_{\rm cl}/10\,{\rm K})$ is the temperature of the clouds. The gas clouds induced by thermal instability have a particle number density of $n_{\rm cl} \sim 10^4\,{\rm cm}^{-3}$, and will therefore collapse to form stars on a free-fall timescale $t_{\rm ff} \sim (G\rho)^{-1/2} \sim 10^6\, n_{\rm cl,4}^{-1/2}$ yrs $\ll t_{\rm dyn}$, where $n_{\rm cl,4} = (n_{\rm cl}/10^4\,{\rm cm}^{-3})$.

7.3 Numerical Results

We note that D_0 must exceed the maximum of the local sound speed, $c_{\rm s}$, and the escape speed of the halo, $v_{\rm esc}$, in order to remain supersonic and capable of entering neighboring halos. Figure 7.3 shows the critical redshift, $z_{\rm c}$, beyond which the detonation mode of the star formation front fails to satisfy this requirement. Overall, we find that the star formation front is self-sustainable for a broad range of $q_{\rm IMF} f_{\rm SN}$ and $\epsilon_\star$. We numerically solve Eq. (7.1) for the density, pressure, axial and radial velocities of the flow behind the star formation shock front, as shown in Figures 7.4-7.5, for model parameters taken at their fiducial values. We find that two-dimensional effects are more significant in halos with smaller radii, which suffer from energy losses due to lateral expansion. In these halos, the star formation front propagates with a moderate speed of $\sim 300\,{\rm km\,s^{-1}}$, while in halos with a larger $R_{\rm vir}$, D_0 reaches $\gtrsim 700\,{\rm km\,s^{-1}}$. The star formation front is curved due to lateral expansion and the streamlines in the flow diverge. In the rest frame of the star formation front, the sonic locus, shown as the lower boundary in Figures 7.4-7.5, is the place where the flow speed is equal to the local sound speed. Star formation and energy release are incomplete in the subsonic zone between the shock front and sonic locus, behind which the flow is supersonic in the detonation front rest frame. Therefore, only the energy injection from this region, also known as the detonation driving zone (Watt et al. 2012), is available to drive the propagation of the star formation front. D_0 is less than the ideal one-dimensional value, $D_{\rm CJ}$, and depends on the shock curvature and $R_{\rm vir}$, consistently with the results shown in Fig. 7.3. Our plots indicate that the star formation front is self-perpetuating for $q_{\rm IMF} f_{\rm SN} \gtrsim 10^{-4}$ and $\epsilon_\star \gtrsim 10^{-4}$ in dwarf galaxies. This indicates that for a massive IMF, the required energy to sustain the propagation of the shock can be as low as $\sim 10^{-4}$ of the energy produced by SN, consistent with numerical simulation (Whalen et al. 2008). The front's characteristic speed is $\sim 300-700\,{\rm km\,s^{-1}}$ during the epoch of reionization. This indicates that the star formation front can initiate starbursts in dwarf galaxies and supply the needed ionizing photons in the early Universe (Finkelstein et al. 2015).

7.4 Summary & Discussion

We explored the ignition of star formation in low-mass halos by a self-sustaining star formation front along cosmic filaments in the early Universe. The gaseous fuel in these most abundant low-mass halos can not turn to stars due to their low-metallicity and low $T_{\rm vir}$. During the front's passage through each halo, the swept-up shell is capable of cooling rapidly and fragmenting into cold clumps that form stars on a timescale shorter than the front's dynamical timescale. The propagation of the star formation front is maintained by energy injection from SN explosions, in analogy with the propagation of a detonation shock in gunpowder. Assuming two-dimensional cylindrical symmetry, we find that the front traverses a filament with an average speed of $\sim 300-700\,{\rm km\,s^{-1}}$.

As the star formation front propagates, the active region would appear to have a length of $\sim D_0 T_\star \sim 1.5$ kpc (corresponding to $\sim 0.3''$ at $z \sim 10$, resolvable by *JWST*), where $T_\star \sim 3\times10^6$ yrs is the lifetime of massive stars ($\gtrsim 10\,M_\odot$) which should dominate the UV emission in the early Universe (Bromm & Yoshida 2011; Loeb & Furlanetto 2013). We find that the length of the illuminated starburst region is up to ten times longer than the width of the filament at $z \gtrsim 20$ for H_2 halos. Future observations with the *JWST* may reveal these elongated structures and constrain the speed of the star formation fronts.

Detection of the rest-frame UV flux from the illuminated fragment of filaments will constrain the free parameters of the detonation model, since the UV flux is correlated

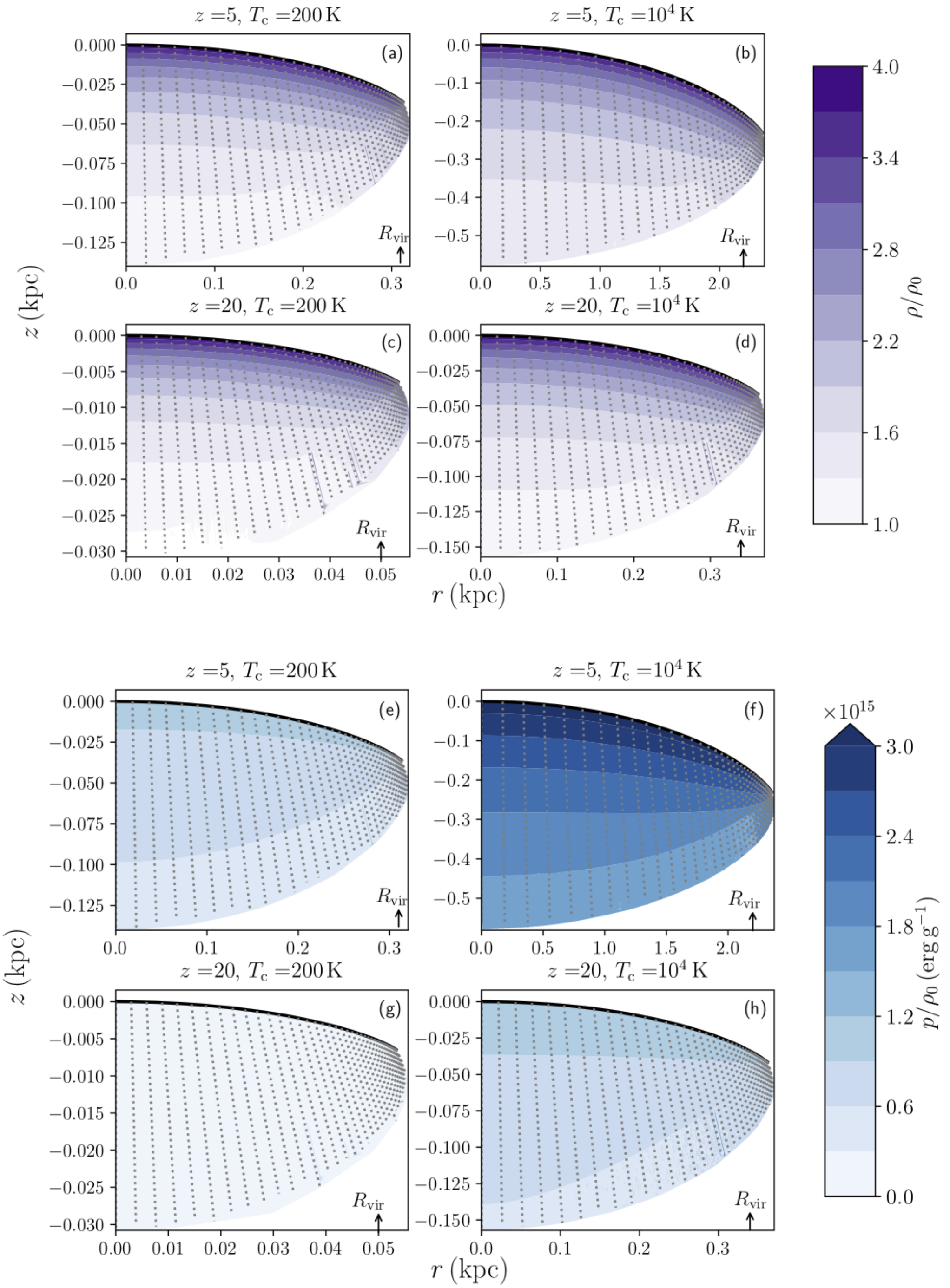

Figure 7.4 Flow density and pressure behind the detonation shock. We show the ratio of flow density (panel (a)-(d)) and pressure (panel (e)-(h)) behind the shock to the ambient medium density ρ_0, for $z = 5$, 20 and $t_{\rm cool} = 200$ K and 10^4 K. In each panel, the solid black and dashed grey curves represent the shock front and the flow streamlines, respectively. The end of the streamlines marks the sonic locus. The values of $R_{\rm vir}$ are shown at the bottom right corner.

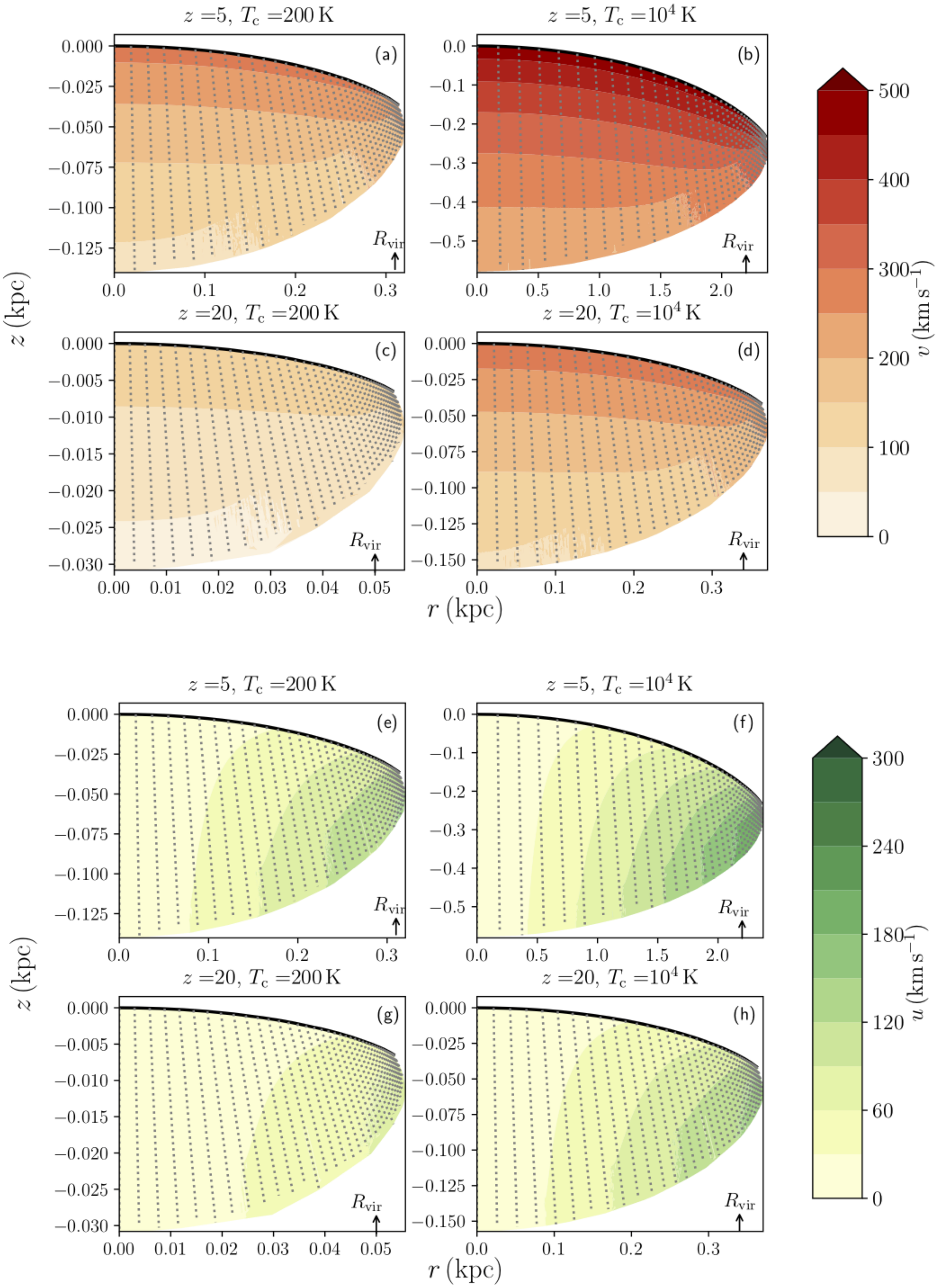

Figure 7.5 Axial flow speed (panel (a)-(d)) and radial flow speed (panel (e)-(h)), behind the detonation shock. The arrangement of the plot is the same as in Fig. 7.4. The detonation wave experiences energy loss due to lateral expansion, and thus D_0 departs from $D_{\rm CJ}$.

with the SFR, SFR $\approx 1.4\, L_{\nu,28}\, M_{\odot}\,\mathrm{yr}^{-1}$, where $L_{\nu,28} = (L_{\nu}/10^{28}\,\mathrm{erg\,s^{-1}\,Hz^{-1}})$ is the UV luminosity at a rest-frame wavelength of $\sim 1250 - 1500$ Å(see Loeb & Furlanetto 2013, p.352). Additionally, radio emission from the relativistic electrons produced in SN remnants can be measured to infer the SFR, as the SN rate tracks to the production rate of massive stars. Our model assumes that SFR is proportional to the locally observed KS law with a correction factor $\epsilon_{\star}$. We find that the detonation mode of star formation fronts is viable for a SFR up to $\gtrsim 10^4$ times less efficient than associated with the KS law, indicating that even at the beginning of reionization, low-mass halos may experience starburst activity during the passage of a shock from triggered star formation in neighboring halos. Radiative pre-processing by H II regions may be an additional source of energy injection to sustain the star formation fronts. However, H II regions produce shocks of speed $\sim 30\,\mathrm{km\,s^{-1}}$ in primordial halos (Wise et al. 2012), much smaller than that produced by SN, which are the dominate energy source. This self-sustaining mode of star formation fronts may account for the ionizing photons in low-mass halos at $z \gtrsim 10$, as required by current observations (Robertson et al. 2015; Anderson et al. 2017). Future probes of the faint end slope of the UV luminosity function of the star-forming galaxies with *JWST* will be able to test our predictions for star forming fronts in cosmic filaments. Even if the luminosity of an individual low-mass galaxy is below the detection threshold of *JWST*, filaments could be detectable since they contain many such galaxies.

7.5 Appendix

7.5.1 Idealized One-Dimensional Detonation Model

In a one-dimensional laminar flow detonation model, known as the Zeldovich-Von-Neumann-Doering (ZND) model, the flow equations are given by the one-dimensional conservation laws of mass continuity, momentum and energy (Fickett & Davis 1979; Watt et al. 2012):

$$\rho u = \rho_0 D_0 \tag{7.6a}$$

$$p + \rho u^2 = p_0 + \rho_0 D_0^2 \tag{7.6b}$$

$$e + \frac{p}{\rho} + \frac{1}{2}u^2 = e_0 + \frac{p_0}{\rho_0} + \frac{1}{2}D_0^2 \tag{7.6c}$$

$$\frac{d\lambda}{dt} = \frac{W}{u} \tag{7.6d}$$

where terms with subscript 0 denote initial conditions in the medium. The Rayleigh line in the (p, V) plane is defined as, where $V = 1/\rho$ is the specific volume:

$$R \equiv \rho_0^2 D_0^2 - \frac{p - p_0}{V_0 - V} = 0\ . \tag{7.7}$$

The curve on the (p, V) plane that corresponds to conservation of energy is known as the Hugonior curve:

$$H \equiv e - e_0 - \frac{1}{2}(p + p_0)(V_0 - V) = 0 \tag{7.8}$$

There is a unique solution of D_0 where the Rayleigh line and Hugoniot curve are tangent. This corresponds to the minimum detonation speed that satisfies the conservation laws, known as the Chapman-Jouguet (CJ) velocity, D_{CJ}.

7.5.2 Steady State Solution for Two-Dimensional Detonation Wave

For a two-dimensional cylindrical geometry, let r and z denote the radial and axial directions, with $r = 0$ corresponding to the center of the halo and $r = R_{\rm vir}$ representing the edge of the halo. $z = 0$ is chosen to correspond to the detonation shock position at the axis, as shown in Fig.7.2. We introduce a compressible streamline function, ψ, such that the continuity equation is satisfied:

$$\left(\frac{\partial \psi}{\partial r}\right)_z = -r\rho v \ , \quad \left(\frac{\partial \psi}{\partial z}\right)_r = r\rho u \ , \tag{7.9}$$

where u and v are the flow speed in r and z directions, respectively. Curves of constant ψ are streamlines. We can transform (r, z) to a streamline based coordinate (ψ, z), in which r is a function of ψ and z. Thus, the material derivative can be written as:

$$\frac{D}{Dt} = v\left(\frac{\partial}{\partial z}\right)_\psi \ . \tag{7.10}$$

Therefore, we can rewrite the governing PDEs in the streamline-based coordinate:

$$\frac{\partial}{\partial z}\left(\frac{1}{\rho v}\right)_\psi + r\frac{\partial}{\partial \psi}\left(\frac{u}{v}\right)_z = \frac{u}{\rho v^2 r} \ . \tag{7.11a}$$

$$\left(\frac{\partial u}{\partial z}\right)_\psi - r\left(\frac{\partial p}{\partial \psi}\right)_z = 0 \ ; \quad \rho v\left(\frac{\partial v}{\partial z}\right)_\psi + r\rho u\left(\frac{\partial p}{\partial \psi}\right)_z + \left(\frac{\partial p}{\partial z}\right)_\psi = 0 \ . \tag{7.11b}$$

$$\left(\frac{\partial e}{\partial z}\right)_z = \frac{p}{\rho^2}\left(\frac{\partial \rho}{\partial z}\right)_\psi \ . \tag{7.11c}$$

$$\left(\frac{\partial \lambda}{\partial z}\right)_\psi = \frac{W}{v} \ . \tag{7.11d}$$

We integrate Eq.(7.11b) and Eq.(7.11c) to obtain the Bernoulli equation:

$$\frac{\gamma p}{(\gamma - 1)\rho} + \frac{1}{2}\left(u^2 + v^2\right) - Q\lambda = \frac{1}{2}D_0^2 \ , \tag{7.12}$$

where D_0 is the steady state detonation velocity. Combining Eq.7.5 and Eq.7.11, we obtain:

$$\frac{\partial v}{\partial z}\left[v^2\left(1+\left(\frac{\partial r}{\partial z}\right)^2\right)-c_{\mathrm{s}}^2\right]=c_{\mathrm{s}}^2 v\left[\frac{\partial r}{\partial z}\frac{1}{r}+\frac{\partial^2 r}{\partial z\partial\psi}\left(\frac{\partial r}{\partial\psi}\right)^{-1}\right]-v^3\frac{\partial r}{\partial z}\frac{\partial^2 r}{\partial z^2}-(\gamma-1)QW\ , \tag{7.13a}$$

$$\frac{\partial\lambda}{\partial z}=\frac{W}{v}\ , \tag{7.13b}$$

where c_{s} is the sound speed.

If the shape of the streamlines, $r(\psi, z)$, were known a priori, then Eq.(7.13) reduce to a pair of ordinary differential equations for v and λ along each streamline where ψ =constant, and thus the full solution of the flow can be obtained (Watt et al. 2012).

Here we follow the straight streamline assumption (SSA), where we assume that the streamlines are straight but diverging, with deflection angle determined by the oblique shock jump condition. Therefore, we can express the streamline shape in the following form:

$$r=r_{\mathrm{f}}+F(\psi)(z-z_{\mathrm{f}})\ , \tag{7.14}$$

where $(r_{\mathrm{f}}, z_{\mathrm{f}})$ denotes the shock front locus, and at the shock front

$$F(\psi)=\left(\frac{\partial r}{\partial z}\right)_{\mathrm{f}}=\frac{u_{\mathrm{f}}}{v_{\mathrm{f}}}\ , \tag{7.15}$$

where u_{f} and v_{f} are the post-shock flow velocities that can be obtained from the shock jump conditions:

$$u_{\mathrm{f}}=-\frac{2D_0 z_{\mathrm{f}}'}{\gamma+1}\left[1+(z_{\mathrm{f}}')^2\right]^{-1}\ , \tag{7.16a}$$

$$v_{\mathrm{f}}=-D_0\left[(z_{\mathrm{f}}')^2+\frac{\gamma-1}{\gamma+1}\right]\left[1+(z_{\mathrm{f}}')^2\right]^{-1}\ , \tag{7.16b}$$

where $z'_{\rm f} = dz_{\rm f}/dr_{\rm f}$. We note that the undisturbed streamlines ahead of the shock are parallel, and thus:

$$\psi = \frac{1}{2} r_{\rm f}^2 \rho_0 D_0 \ , \tag{7.17}$$

where ρ_0 is the density of the ambient medium. To solve Eq.(7.13), we obtain the coefficients under SSA, where,

$$\left(\frac{\partial r}{\partial z}\right)_\psi = F(\psi) \ , \tag{7.18a}$$

$$\left(\frac{\partial r}{\partial \psi}\right)_z = \frac{dr_{\rm f}}{d\psi} + \frac{dF}{d\psi}(z - z_{\rm f}) - F(\psi) z'_{\rm f} \frac{dr_{\rm f}}{d\psi} \ , \tag{7.18b}$$

$$\frac{\partial^2 r}{\partial \psi \partial z} = \frac{dF}{d\psi} = \frac{z''_{\rm f}}{\rho_0 D_0 r_{\rm f}} \frac{dF}{dz'_{\rm f}} \ , \tag{7.18c}$$

$$\left(\frac{\partial^2 r}{\partial z^2}\right)_\psi = 0 \ . \tag{7.18d}$$

and where $z''_{\rm f} = dz'_{\rm f}/dr_{\rm f}$. We note that Eq.(7.18d) is a direct result from SSA.

Therefore, the solutions of Eq.(7.13) depend on the shock locus and shock shape via $(r_{\rm f}, z_{\rm f}, z'_{\rm f}, z''_{\rm f})$. This results in an eigenvalue problem of $z''_{\rm f}$ in that if $z'_{\rm f}$ was known a priori, there would be a unique $z''_{\rm f}$ that satisfies the shock jump condition and the CJ condition (Fickett & Davis 1979) for a given D_0:

$$v^2 \left[1 + \left(\frac{\partial x}{\partial y}\right)^2\right] - c_{\rm s}^2 = 0 \ , \quad \left(\frac{\partial x}{\partial \psi}\right)^{-1} c_{\rm s}^2 v \frac{\partial^2 x}{\partial y \partial \psi} - (\gamma - 1) Q W = 0 \ . \tag{7.19}$$

We find that $D_0 \propto 1/R_{\rm vir}$ due to the multi-dimensional effect, known as the diameter effect of detonation waves (Watt et al. 2012).

Acknowledgements

We thank Simon D. Watt and Anna Rosen for useful discussions. This work was supported in part by the Black Hole Initiative at Harvard University through a grant from the John Templeton Foundation.

Chapter 8

Detecting Floating Black Holes as They Traverse the Gas Disc of the Milky Way

This thesis chapter originally appeared in the literature as

X. Wang & A. Loeb, Detecting Floating Black Holes as They Traverse the Gas Disc of the Milky Way, *Monthly Notices of the Royal Astronomical Society*, 441, 809 (2014)

Abstract

A population of intermediate-mass black holes (BHs) is predicted to be freely floating in the Milky Way (MW) halo, due to gravitational wave recoil, ejection from triple BH systems, or tidal stripping in the dwarf galaxies that merged to make the MW. As these

BHs traverse the gaseous MW disk, a bow shock forms, producing detectable radio and mm/sub-mm synchrotron emission from accelerated electrons. We calculate the synchrotron flux to be $\sim 0.01 - 10\,\mathrm{mJy}$ at GHz frequency, detectable by *Jansky Very Large Array*, and $\sim 10 - 100\,\mu\mathrm{Jy}$ at $\sim 10^{10} - 10^{12}\,\mathrm{Hz}$ frequencies, detectable by *Atacama Large Millimeter/sub-millimter Array.* The discovery of the floating BH population will provide insights on the formation and merger history of the MW as well as on the evolution of massive BHs in the early Universe.

8.1 Introduction

Galaxies grow through accretion and hierarchical mergers. During the final phase of the merger of two central black holes, anisotropic emission of gravitational waves (GW) kicks the BH remnant with a velocity up to a few hundreds $\mathrm{km\,s^{-1}}$ (Baker et al. 2006; Campanelli et al. 2007; Blecha & Loeb 2008). Additionally, BHs can be ejected from triple systems (Kulkarni & Loeb 2012; Hoffman & Loeb 2007), or result from tidally-stripped cores of dwarf galaxies (Bellovary et al. 2010). For GW recoils, the typical kick velocity is large enough for the BHs to escape the shallow gravitational potential of low-mass galaxies, but smaller than the escape velocity of the MW halo. This is also the case for triple systems as long as the kick velocity is $< 500\,\mathrm{km\,s^{-1}}$. Consequently, a population of floating BHs formed from mergers of low-mass galaxies are trapped in the region that eventually makes the present-day MW (Madau & Quataert 2004; Volonteri & Perna 2005; Libeskind et al. 2006). Previous studies suggested that more than ~ 100 floating BHs should be in the halo today, based on a large statistical sample of possible merger tree histories for the MW halo today (O'Leary & Loeb 2009, 2012). This population of recoiled BHs is supplemented by BHs from tidally disrupted satellites of the MW (Bellovary et al. 2010). The discovery of this BH population will provide constraints on the formation and merger history of the MW as well as the dynamical evolution of massive BHs in the early Universe.

It has been proposed that a compact cluster of old stars from the original host galaxies is carried by each floating BH (O'Leary & Loeb 2009). In this Letter, we propose an additional observational signature of floating BHs, using the MW gas disk as a detector. As the BHs pass through the MW disk supersonically they generate a bow shock, which results in synchrotron radiation detectable at radio and mm/sub-mm frequencies.

The chapter is organized as follows. In § 8.2, we discuss the interaction between BHs and the gas in the MW disk. In § 8.3, we calculate the synchrotron radiation from the bow shocks produced as the BHs cross the MW disk, and discuss the detectability of this radiation. Finally, in § 8.4, we summarize our results and discuss their implications.

8.2 Interaction Between a Floating Black Hole and the MW Disk Gas

We consider a BH moving at a speed $V_\bullet$ relative to the interstellar medium (ISM) of number density $n_{\rm ISM}$. The effective radius of influence of the moving black hole is given by the Bondi accretion radius:

$$R_{\rm Bondi} = \frac{GM_\bullet}{c_{\rm s}^2 + V_\bullet^2} \approx \frac{GM_\bullet}{V_\bullet^2} = 0.01\, M_5\, V_{200}^{-2}\ {\rm pc}\ , \tag{8.1}$$

where G is Newton's constant, $M_5 = (M_\bullet/10^5 M_\odot)$ and $V_{200} = (V_\bullet/200\,\mathrm{km\,s^{-1}})$. The sound speed c_s of hydrogen in the ISM is given by $c_\mathrm{s} = (\Gamma P/\rho)^{1/2} = 11.7\,T_4^{1/2}\,\mathrm{km\,s^{-1}}$, where $\Gamma = 5/3$ is the adiabatic index and $T_4 = (T/10^4\,\mathrm{K})$. In the case of a supersonic shock with velocity $V_\mathrm{sh} \gg c_\mathrm{s}$, the total mass enclosed within the Bondi radius is given by $\Delta M_\mathrm{ISM} = 1.3 \times 10^{-7}\, M_5^3\, V_{200}^{-6}\, n_0\, M_\odot$, where $n_0 = (n_\mathrm{ISM}/10^0\,\mathrm{cm^{-3}})$. The rate of fresh mass being shocked in the ISM is $\Delta \dot{M}_\mathrm{ISM} = 3.7 \times 10^{-9}\, M_5^2\, V_{200}^{-3}\, n_0\, M_\odot\,\mathrm{yr^{-1}}$. The total kinetic power can be expressed as,

$$
\begin{aligned}
L_\mathrm{kin} &= \frac{1}{2}\left(2\pi R_\mathrm{Bondi}^2 n_\mathrm{ISM} m_\mathrm{p} V_\bullet\right) V_\bullet^2 \\
&= 4.7 \times 10^{31} M_5^2\, V_{200}^{-1}\, n_0\ \mathrm{erg\,s^{-1}}\ ,
\end{aligned}
\tag{8.2}
$$

where m_p is the proton mass.

8.3 Observational Appearance

As a floating BH travels through the MW disk supersonically, a bow shock is formed with a half opening angle $\theta \sim \mathcal{M}^{-1}$ (Shu 1992; Kim & Kim 2009), where the Mach number is given by $\mathcal{M} = V_\bullet/c_\mathrm{s} \approx 17.0\, V_{200}\, T_4^{-1/2}$ (see Fig.8.1). The electrons accelerated in the shock produce non-thermal radiation that can be detected.

8.3.1 Non-thermal Spectrum

Single Electron

Next, we calculate synchrotron emission from the shock accelerated electrons around the BH. We adopt $n_0 = 1$ and $T_4 = 1$ in the numerical examples that follow.

From the Rankine-Hugoniot jump conditions for a strong shock the density of the shocked gas is $n_{\rm s} \approx (\Gamma+1)\, n_{_{\rm ISM}}/\,(\Gamma-1) = 4\, n_{_{\rm ISM}}$, whereas its temperature is, $T_{\rm s} = [(\Gamma+1)+2\Gamma(\mathcal{M}^2-1)][(\Gamma+1)+(\Gamma-1)(\mathcal{M}^2-1)]T/(\Gamma+1)^2\mathcal{M}^2$. The magnetic field can by obtained by assuming a near-equipartition of energy $U_{\rm B} = B^2/8\pi = \xi_{\rm B}\, n_{\rm s}\, kT_{\rm s}$, where $\xi_{\rm B}$ is the fraction of thermal energy carried by the magnetic field. Thus, the magnetic field behind the shock is given by

$$B \approx 35\, \xi_{\rm B,-1}^{1/2}\, n_0^{1/2}\, T_4^{1/2}\ \mu{\rm G}\ , \tag{8.3}$$

where $\xi_{\rm B,-1} = (\xi_{\rm B}/0.1)$. We adopt $\xi_{\rm B,-1} = 1$ in what follows in analogy with supernova (SN) remnants (Chevalier 1998).

For a single electron with Lorentz factor γ, the peak of its synchrotron radiation is at a frequency $\nu_{\rm syn} = 4.2\, B_{-5}\, \gamma_4^2$ GHz, where $\gamma_4 = (\gamma/10^4)$ and $B_{-5} = (B/10^{-5}\,{\rm G})$. The total emitted power per unit frequency is given by (Rybicki & Lightman 1979)

$$P(\nu) = \frac{\sqrt{2}\, e^3 B}{m_{\rm e} c^2} F(x)\ , \tag{8.4}$$

where $F(x) \equiv x \int_x^\infty K_{5/3}(\xi)\, d\xi$, $K_{5/3}(x)$ is the modified Bessel function of 5/3 order, $x = \nu/c_1 B\gamma^2$, $c_1 = \sqrt{6}\, e/4\pi m_{\rm e} c$, c is the speed of light and $m_{\rm e}$, e are the electron mass and charge respectively. The pitch angle is assumed to be uniformly distributed.

The total power from synchrotron emission of a single electron is given by (Rybicki & Lightman 1979)

$$P_{\rm syn} = \frac{4}{9} r_0^2 c \beta^2 \gamma^2 B^2 = 2.5 \times 10^{-18} B_{-5}\, \nu_{_{\rm GHz}}\ {\rm erg\, s^{-1}}\ , \tag{8.5}$$

where $r_0 = e^2/m_{\rm e}c^2$ is the classical radius of the electron and $\nu_{_{\rm GHz}} = (\nu_{\rm syn}/{\rm GHz})$. We estimate the cooling time to be $t_{\rm cool} = \gamma mc^2/P_{\rm syn} = 5.0 \times 10^7 B_{-5}^{-3/2} \nu_{_{\rm GHz}}^{-1/2}$ yr for $V_{200} = 1$. Since most of the emission is near the head of the Mach cone, we compare the cooling timescale with the dynamical timescale, which is given by $t_{\rm dyn} = R_{\rm Bondi}/V_\bullet \approx 53\, M_5 V_{200}^{-3}$ yr. For the emission frequencies of interest, the cooling time is much longer than the lifetime of the shock.

Power-law distribution of electrons

Next we consider a broken power law distribution of electrons generated via Fermi acceleration:

$$N(\gamma)\, d\gamma = K_0 \gamma^{-p} \left(1 + \frac{\gamma}{\gamma_{\rm b}}\right)^{-1} \; (\gamma_{\rm min} \leq \gamma \leq \gamma_{\rm max}), \tag{8.6}$$

where K_0 is the normalization factor in electron density distribution, p is the electron power law distribution index, and $\gamma_{\rm b}$, $\gamma_{\rm min}$, $\gamma_{\rm max}$ are the break, minimum and maximum Lorentz factor respectively. The break in the power law is due to synchrotron cooling. The total synchrotron power can be written as,

$$\begin{aligned} L_{\rm nt} = \epsilon_{\rm nt} L_{\rm kin} &= \int_{\gamma_{\rm min}}^{\gamma_{\rm max}} P_{\rm syn} N(\gamma)\, d\gamma \\ &= 2.3 \times 10^{30} \epsilon_{\rm nt}5\, M_5^2\, V_{200}^{-1}\, n_0\ {\rm erg\, s^{-1}}\ , \end{aligned} \tag{8.7}$$

where $\epsilon_{\rm nt}5 = (\epsilon_{\rm nt}/5\%)$ is the fraction of electrons accelerated to produce non-thermal radiation. The normalization constant K_0 is obtained from the relation $K_0 = L_{\rm nt}/\int_{\gamma_{\rm min}}^{\gamma_{\rm max}} P_{\rm syn}\gamma^{-p}\, d\gamma$. Observations imply that the ISM density distribution in the MW disk midplane can be roughly described by the form (Spitzer 1942; Kalberla & Kerp 2009),

$$n_{\rm ISM}(r, z) = n_{\rm c} e^{-(r-R_\odot)/R_{\rm n}} {\rm sech}^2 \left[\frac{z}{\sqrt{2} z_0(r)}\right]\ , \tag{8.8}$$

where r and z are the radial and vertical coordinates relative to the disk midplane, $n_{\rm c} = 0.9\,{\rm cm}^{-3}$, $R_{\rm n} = 3.15\,{\rm kpc}$ and $z_0(r)$ is the scale height at r, given by $z_0(r) = h_0\, e^{(r-R_\odot)/r_0}$

with $h_0 = 0.15\,\mathrm{kpc}$, $R_\odot = 8.5\,\mathrm{kpc}$ and $r_0 = 9.8\,\mathrm{kpc}$ (Kalberla & Kerp 2009). The gas density and non-thermal luminosity as a function of radius in the MW disk midplane are shown in Figure 8.2.

The electron acceleration time scale is given by $t_{\rm acc} = \xi_{\rm acc}\gamma m_{\rm e} c^3/eBV_\bullet^2$, where $\xi_{\rm acc}$ is a dimensionless constant of order unity (Blandford & Eichler 1987). The upper limit of the Lorentz factor $\gamma_{\rm max}$ can be obtained by equaling the acceleration and cooling timescale of electrons, $t_{\rm acc} = t_{\rm cool}$, giving

$$\gamma_{\rm max} = \frac{3 m_{\rm e} c V_\bullet}{2\,\xi_{\rm acc}^{1/2} B^{1/2} e^{3/2}} = 2.5 \times 10^7\ V_{200}\, B_{-5}^{-1/2}\ . \tag{8.9}$$

Since the time the gas stays in the shocked region for the electrons to be accelerated is roughly the dynamical timescale, an additional constraint on $\gamma_{\rm max}$ can be obtained by equating the acceleration timescale of electrons and the dynamical time, $t_{\rm acc} = t_{\rm dyn}$, giving

$$\gamma_{\rm max} = \frac{eBV_\bullet R_{\rm Bondi}}{\xi_{\rm acc} m_{\rm e} c^3} = 1.2 \times 10^5\, B_{-5} M_5 V_{200}^{-1}\ . \tag{8.10}$$

We will adopt this tighter constraint on $\gamma_{\rm max}$ in the following calculation. The emission frequency associated with $\gamma_{\rm max}$ is $\nu_{\rm max} = 3\,\gamma_{\rm max}^2 eB/4\pi m_{\rm e} c = 4.2 \times 10^{11}\, B_{-5}\gamma_{\rm max,5}^2\,\mathrm{Hz}$, where $\gamma_{\rm max,5} = (\gamma_{\rm max}/10^5)$. The break Lorentz factor can be obtained by equaling the cooling and the dynamical time, giving $\gamma_{\rm b} = 5.0 \times 10^9 B_{-5}^{-2}\, M_5^{-1} V_{200}^3$ and the corresponding frequency $\nu_{\rm b} = 4.2 \times 10^{10}\, B_{-5}\gamma_{\rm b,9}^2\,\mathrm{GHz}$, where $\gamma_{\rm b,9} = (\gamma_{\rm b}/10^9)$. The value of $\nu_{\rm b}$ is above the frequency range of interest here and does not affect the observable synchrotron spectrum.

The emissivity and absorption coefficients are given by (Rybicki & Lightman 1979)

$$j_\nu = c_2 B \int_{\gamma_{\rm min}}^{\gamma_{\rm max}} F(x) N(\gamma)\, d\gamma\ , \tag{8.11}$$

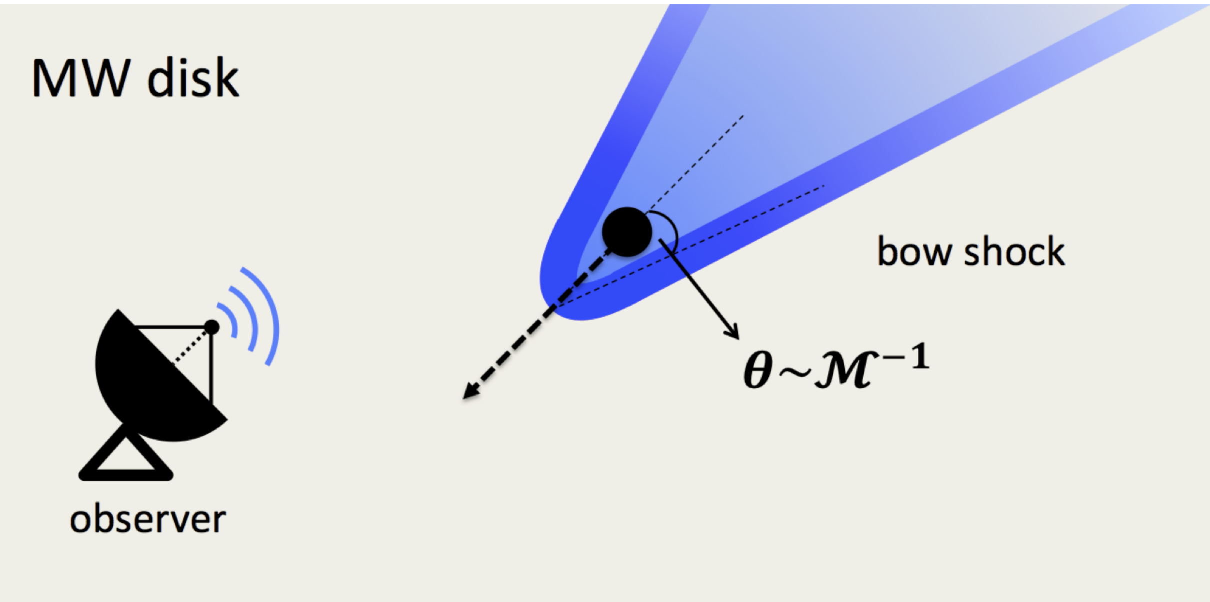

Figure 8.1 Sketch of the bow shock geometry around a BH crossing the gaseous MW disk.

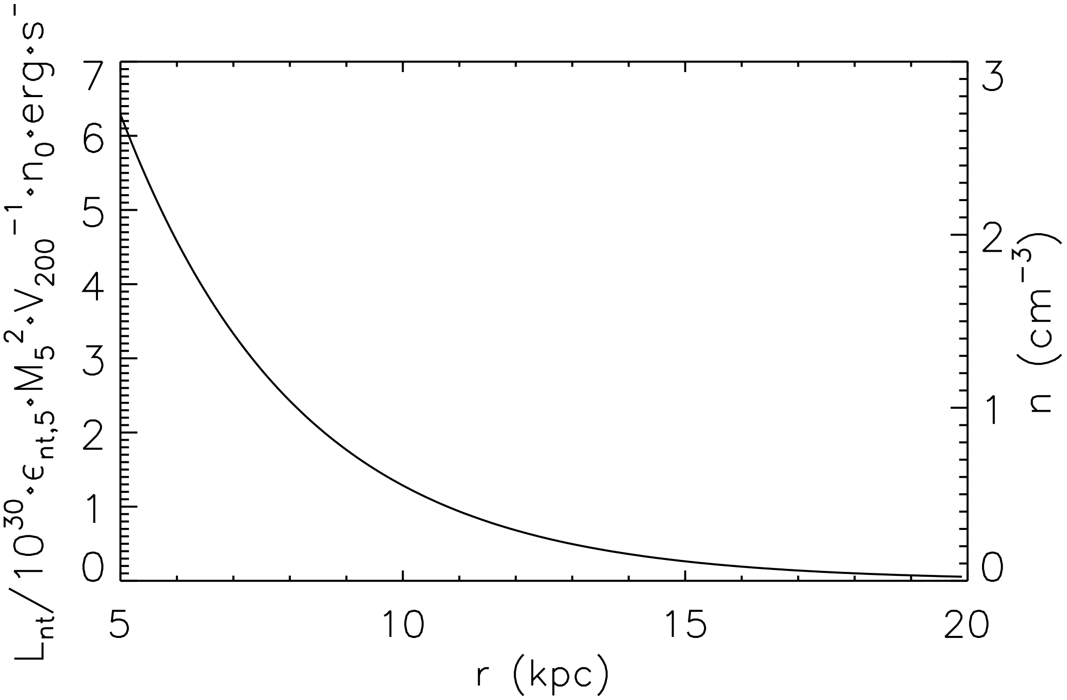

Figure 8.2 Gas density, $n_{\rm ISM}(z = 0)$, and non-thermal luminosity in units of $10^{30}\epsilon_{\rm nt}5M_5^2\,V_{200}^{-1}\,n_0$ in the midplane of the MW disk.

$$\alpha_\nu = -c_3 B \frac{1}{\nu^2} \int_{\gamma_{\rm min}}^{\gamma_{\rm max}} \gamma^2 \frac{d}{d\gamma} \left[\frac{N(\gamma)}{\gamma^2} \right] F(x)\, d\gamma \ , \tag{8.12}$$

where $c_2 = \sqrt{2} e^3/4\pi m_{\rm e} c^2$ and $c_3 = \sqrt{2} e^3/8\pi m_{\rm e}^2 c^2$. From the radiative transfer equation, the specific intensity is given by (Rybicki & Lightman 1979)

$$I_\nu = \frac{j_\nu}{\alpha_\nu} \left(1 - e^{-\tau_\nu} \right) \ , \tag{8.13}$$

where τ_ν is the optical depth. The synchrotron luminosity and corresponding flux at a distance $d = 10$ kpc from the observer are plotted in Figure 8.3.

8.3.2 Emission from the Vicinity of the BH

Next we estimate the emission from the vicinity of the BH through a hot accretion flow (Narayan & Yi 1994). The Bondi accretion rate is given by $\dot{M}_{\rm Bondi} = 9.1 \times 10^{17} M_5^2\, n_0 V_{200}^{-3}$ g s^{-1} (Armitage & Natarajan 1999), and the Eddington accretion rate can be expressed as $\dot{M}_{\rm Edd} = L_{\rm Edd}/0.1c^2 = 1.39 \times 10^{23}\, M_5$ g s^{-1}. We estimate the total luminosity in a radiatively inefficient accretion flow (RIAF) as,

$$L_\bullet = \eta \dot{M} c^2 = 5.4 \times 10^{31} \zeta_{-1}^2\, M_5^3\, n_0^2\, V_{200}^{-6}\ {\rm erg\, s^{-1}} \ , \tag{8.14}$$

where $\eta \approx 0.1 \left(\dot{M}/0.1\dot{M}_{\rm Edd} \right)$ is the efficiency of converting matter to radiation for $\dot{M} \leq 0.1\dot{M}_{\rm Edd}$ (Narayan & McClintock 2008) and $\zeta = \dot{M}/\dot{M}_{\rm Bondi} = 10\, \zeta_{-1}$ is the accretion rate in units of $\dot{M}_{\rm Bondi}$. The BH accretion would produce X-ray emission which is not expected from the bow shock spectrum in Fig.8.3. Since $L_\bullet \propto M_5^3$, the accretion luminosity from interstellar medium accretion onto stellar mass BHs is negligible compared to our souce (Fujita et al. 1998).

It is possible that an outflow would be formed near the BH. The outflow would produce a shock at a radius $R_{\rm out}$, which can be obtained from $f\dot{M} = \dot{M}_{\rm out} =$

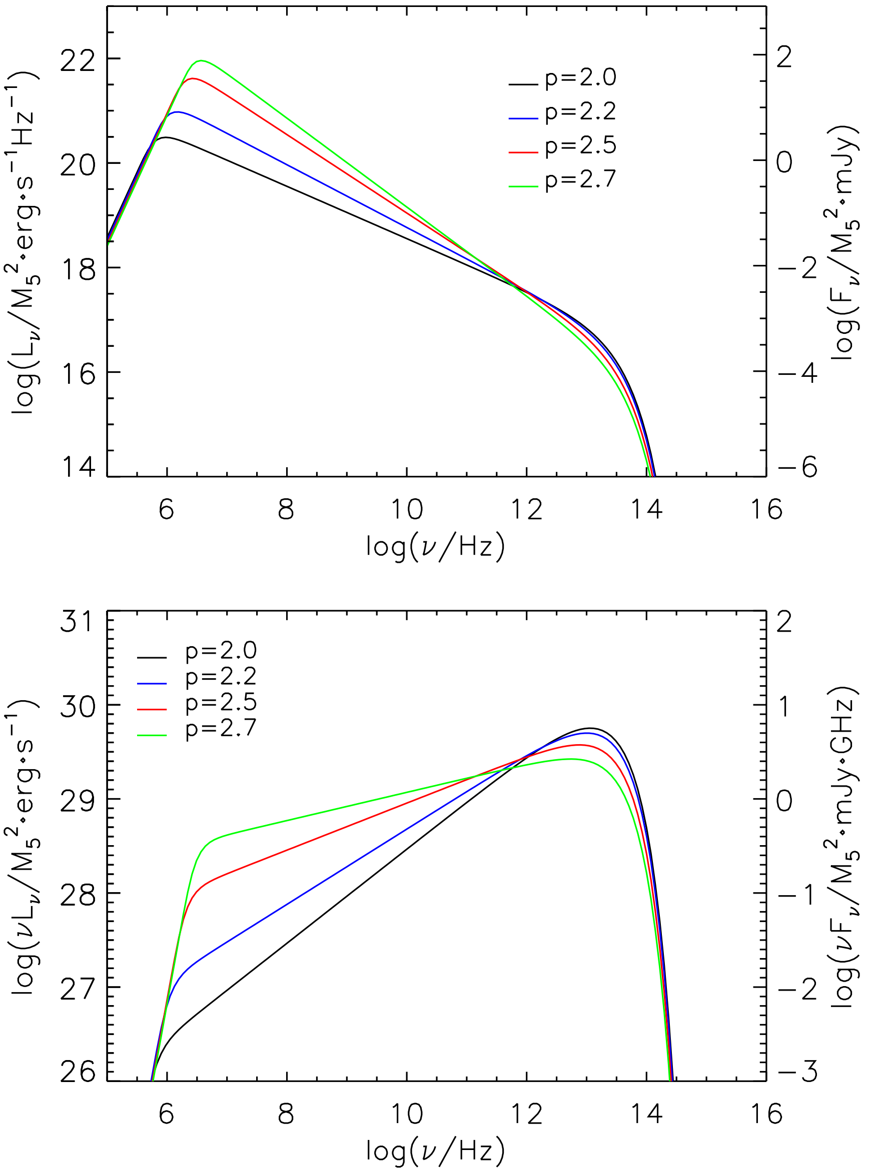

Figure 8.3 Synchrotron power and flux from non-thermal electrons accelerated by the bow shock of floating BHs, in units of M_5^2, for $n_0 = 1$, $V_{200} = 1$, $L_{\rm nt} = 3.0 \times 10^{30}\ {\rm erg\,s^{-1}}$, $B_{-5} = 3.5$, $\gamma_{\rm min} \sim 1$ and $\gamma_{\rm max} \sim 4.2 \times 10^5$. The upper panel shows synchrotron flux while the lower panel shows the corresponding power. The left label of the vertical axis marks synchrotron luminosity per unit frequency (upper panel) or power per $\log \nu$ (lower panel) while the right one marks the corresponding flux at a distance of $d = 10$ kpc. The black, blue, red and green lines correspond to power-law indices $p = 2.0,\ 2.2,\ 2.5,\ 2.7$ respectively in the electron energy distribution. Synchrotron self-absorption is significant at a frequency $\leq$ MHz and the cooling break corresponds to a frequency $\sim 10^{19}$ Hz, which are outside the frequency range of interest.

$4\pi R_{\rm out}^2 n_{\rm ISM} m_{\rm p} V_{\rm out}$, where $f \leq 1$ is the fraction of the inflowing mass channelled into the outflow. This gives,

$$\begin{aligned} R_{\rm out} &= \left(\frac{f\dot{M}}{4\pi n_{\rm ISM} m_{\rm p} V_{\rm out}} \right)^{1/2} \\ &= 6.8 \times 10^{-4} \, f^{1/2} \zeta_{-1}^{1/2} M_5 V_{200}^{-3/2} V_{\rm out,4}^{-1/2} \ \text{pc} \ , \end{aligned} \tag{8.15}$$

where $V_{\rm out,4} = (V_{\rm out}/10^4\,{\rm km\,s^{-1}})$ is the velocity of the outflow. For typical parameters, we find that the outflow would be bounded with $R_{\rm out} \leq R_{\rm Bondi}$.

8.3.3 Observational signatures and detectability

Observationally, the BH emission cone would appear arc-shaped, with an angular diameter $\theta = R_{\rm Bondi}/d = 0.22\, d_1^{-1} M_5 V_{200}^{-2}$ arcsec, where $d_1 = (d/10\,{\rm kpc})$. The non-thermal radiation should be detectable at radio and mm/sub-mm bands. At a frequency $\nu \sim 1\,{\rm GHz}$, the synchrotron flux at a distance of 10 kpc is of order $0.01 - 10\,{\rm mJy}$, depending on the choice of p. This flux is detectable with the Jansky Very Large Array (JVLA), which has a complete frequency coverage from $1 - 50$ GHz, with a sensitivity of $\sim 5.5\,\mu{\rm Jy}$/beam in a 1-hour integration and a signal to noise ratio S/N = 1 at $1 - 2$ GHz (Perley et al. 2011). At a frequency $\nu \sim 10^{10} - 10^{12}$ Hz in the mm/sub-mm band, the synchrotron flux at a distance of 10 kpc is of order $10 - 100\,\mu{\rm Jy}$, which is detectable by the Atacama Large Millimeter/sub-millimeter Array (ALMA), covering a wavelength range of $0.3 - 9.6\,{\rm mm}$, with an integration time of roughly 10^4 s.

Morphologically, it is possible to distinguish the bow shock emission from other radio sources such as SN remnants or HII regions. The bow shock emission is elongated along the direction of the BH's motion, whereas SN remnants would appear roughly circular on the sky. There are hundreds of cometary HII regions produced by a combination of supersonic motion of an OB-type star through dense gas and ionization of gas down a density gradient (Cyganowski et al. 2003; Immer et al. 2014). The Mach cone's opening angle can be used to distinguish them from the much faster floating BHs. The ongoing survey of the Galactic plane with JVLA (National Radio Astronomy Observatory NRAO) has the potential to separate out these HII regions. There are far fewer confusing HII region sources at larger radius in the disk. Other high-velocity sources are pulsar wind nebulae (Gaensler 2005), hyper-velocity stars (Brown et al. 2006) and runaway stars (del Valle & Romero 2012; del Valle et al. 2013). The first type can be distinguished by observing the pulsar as well as its X-ray emission. The last two types produce less synchrotron radiation (del Valle & Romero 2012; del Valle et al. 2013), and thus can be distinguished as well. Globular clusters crossing the MW disk produce another class of contaminants. Their velocity relative to the disk is much larger than the velocity dispersion of their stars, so their Bondi radius is much smaller than their size. Thus, they should not produce significant synchrotron emission. The floating BHs are also embedded in a star cluster, but the cluster size is more compact and its gravity is dominated by the central BH (O'Leary & Loeb 2009, 2012).

8.4 Summary and Discussion

If a floating BH happens to pass through the MW disk, then the non-thermal emission from the accelerated electrons in the bow shock around the BH should produce detectable signals in the radio and mm/sub-mm bands. The radio flux $\sim 0.01-10$ mJy is detectable by JVLA, while the mm/sub-mm flux $\sim 10-100\,\mu$Jy is detectable by ALMA.

The density distribution of floating BHs in the MW has been studied by O'Leary &

Loeb (2009, 2012) and by Rashkov & Madau (2014). High resolution simulations show that there is a BH of mass $\sim 2 \times 10^5 M_\odot$ within a few kpc from the Galactic center (Rashkov & Madau 2014).

Observations of the Galactic disk can be used to infer n_0 and T_4. The BH speed $V_\bullet$ can then be estimated from the Mach cone angle. The maximum Lorentz factor $\gamma_{\rm max}$ can be inferred from the peak of the synchrotron spectrum. This, in turn, yields B_{-5} based on Eq.(3). From the slope of the synchrotron spectrum, the power law index p can be estimated. Finally, with the above parameters constrained, the synchrotron flux can be used to calibrate $M_\bullet$. The above interpretation can be verified by observing the properties of the star cluster carried by the floating BHs (O'Leary & Loeb 2009, 2012). The diffuse X-ray emission from the BH and synchrotron emission from the bow shock is supplemented by stellar emission from the star cluster around it. Since the total mass of the star cluster is much smaller than $M_\bullet$, gravity is dominated by the BH, and thus the stars do not effect the bow shock. One can measure $M_\bullet$ spectroscopically from the velocity dispersion of the stars as a function of distance from the BH, and verify consistency with the synchrotron flux estimate.

Acknowledgements

We thank Jonathan Grindlay, James Guillochon, Ramesh Narayan, Mark Reid and Lorenzo Sironi for helpful comments on the manuscript. We thank Piero Madau for providing the data from *Via Lactea II* simulation. This work was supported in part by NSF grant AST-1312034.

Chapter 9

Non-Thermal Emission from the Interaction of Magnetized Exoplanets with the Wind of Their Host Star

This thesis chapter originally appeared in the literature as

X. Wang & A. Loeb, Non-Thermal Emission from the Interaction of Magnetized Exoplanets with the Wind of Their Host Star, *The Astrophysical Journal Letters*, 874, 2 (2019)

Abstract

We study the non-thermal emission from the interaction between magnetized Jupiter-like exoplanets and the wind from their host star. The supersonic motion of planets through the wind forms a bow shock that accelerates electrons which produces non-thermal radiation across a broad wavelength range. We discuss three wind mass loss rates: $\dot{M}_{\rm w} \sim 10^{-14}$, 10^{-9}, $10^{-6}\ M_\odot\,{\rm yr}^{-1}$ corresponding to solar-type, T Tauri and massive O/B type stars, respectively. We find that the expected radio synchrotron emission from a Jupiter-like planet is detectable by the *Jansky Very Large Array* and the *Square Kilometer Array* at $\sim 1-10$ GHz out to a distance ~ 100 pc, whereas the infrared emission is detectable by the *James Webb Space Telescope* out to a similar distance. Inverse Compton scattering of the stellar radiation results in X-ray emission detectable by *Chandra* X-ray Observatory out to ~ 150 pc. Finally, we apply our model to the upper limit constraints on V380 Tau, the first star-hot Jupiter system observed in radio wavelength. Our bow shock model provides constraints on the magnetic field, the interplanetary medium and the non-thermal emission efficiency in V380 Tau.

9.1 Introduction

Thousands of exoplanet systems have been identified over the past few decades (Winn & Fabrycky 2015). The majority of the currently known population was indirectly discovered via searches for the impact of the exoplanet on its host star.

In analogy with the solar system, exoplanets might possess intrinsic magnetic fields and generate non-thermal radio emission (Garraffo et al. 2016). These magnetized exoplanets can be probed in radio observations since they produce more radio emission than the host star. A number of observations support the existence of magnetic fields in exoplanets. For instance, the near-UV spectroscopic transit of a giant planet WASP-12b shows an early ingress compared to its optical transit and an excess absorption during the transit (Haswell et al. 2012); such a signature has been explained by absorption in a bow shock surrounding the planetary magnetosphere (Llama et al. 2011). Another clue is provided by the modulations of chromoshperic spectral lines in phase with the orbital period, indicating induced activity on the stellar surface due to magnetic interactions between star and planet (Shkolnik et al. 2008). The magnetized planets in the solar system emit low-frequency radio waves from their auroral regions via the cyclotron maser instability (CMI) (Treumann 2006). This emission is observed to be highly circularly (or elliptically) polarized and variable on a time scale from seconds to days (Treumann 2006; Zarka 2007). Magnetized exoplanets are expected to produce radio emission via a similar mechanism. The power of this emission can be estimated by the empirical relation known as the radiometric Bode's law, which relates the incident energy flux of the stellar wind to the radio intensity of a planet, as inferred from observations of magnetized planets in the solar system (Zarka et al. 2001). This method was applied to hot-Jupiters but no detection has been reported as of yet (Jardine & Collier Cameron 2008).

A number of theoretical studies computed the expected exoplanetary radio emission by applying the radiometric Bode's law. They found that the power of the radio emission depends on the planetary magnetic field and the kinetic energy flux of the stellar wind or coronal mass ejections (Grießmeier et al. 2011). Lazio et al. (2004) predicted that planets on tight orbits at distances of a few pc might produce mJy level emission at $\sim 10 - 1000$ MHz frequencies. It has been suggested that stars with winds carrying a larger mass loss rate and velocities than the Sun are ideal targets for radio observations (Stevens 2005), highlighting close-in hot Jupiters around pre-main-sequence and post-main-sequence stars for radio selection (Vidotto & Donati 2017). Many observational campaigns have made effort to detect radio emission from exoplanets. Some of them targeted nearby hot Jupiters (e.g. Bastian et al. (2000); O'Gorman et al. (2018)), while others search for radio emission at locations of known exoplanets from low-frequency sky surveys (e.g. Lazio et al. (2004); Murphy et al. (2015)).

Planetary emission can be used to discover new planets or set constraints on the properties of the interplanetary medium around stars (Wood et al. 2005). The interaction between exoplanets and stellar winds leads to distinct observational signatures, such as stellar activity enhancement (Shkolnik et al. 2005), cometary tail structures (Rappaport et al. 2012) and charge transfer between wind protons and neutral hydrogen atoms (Kislyakova et al. 2014). These signatures provide constraints on the mass loss rate and speed of the stellar wind as well as the planetary magnetic field. The formation of a bow shock from the interaction between stellar wind and exoplanetary magnetic field has been considered (e.g. Zarka (2007); Vidotto et al. (2015)). However, previous discussions were limited to low-frequency radio emission from CMI, with no detailed calculation of the non-thermal emission produced by relativistic particles accelerated by the bow shock.

Here, we compute the non-thermal spectrum as a novel observational signature of exoplanets as they travel in the wind of their host star. The supersonic motion of a planet can produce multi-wavelength emission detectable at a distance of up to hundreds of pc with current and upcoming instrumentation. Aside from revealing new planets, any detection of such an emission can be used to set constraints on the properties of the interplanetary medium, wind mass loss rate and planetary magnetic field.

This chapter is organized as follows. In § 9.2, we characterized the properties of the planetary bow shocks. In § 9.3, we compute the resulting non-thermal synchrotron and inverse Compton emission. In § 9.4, we apply our model to the solar system and the V380 Tau system. Finally, in § 9.5, we summarize our results and discuss observational implications.

9.2 Planetary Bow Shock

As an exoplanet orbits around its host star, it interacts with the wind outflowing from the star. For simplicity, we assume that the wind speed, $v_{\rm w} \sim v_{\rm esc}$, where $v_{\rm esc} \sim (2GM_\star/R_\star)^{1/2}$ is the escape velocity from the star, G is the Newton's constant and $M_\star$ and $R_\star$ are the mass and radius of the star, respectively. The orbits of planets at small separation from their host star are often circularized by tidal dissipation, and their Keplerian orbital velocity is given by, $v_{\rm k} = (GM_\star/R_{\rm orb})^{1/2}$, where $R_{\rm orb}$ is the orbital radius of the planet. Thus, the effective velocity of the planet relative to the interplanetary plasma is of order $\Delta v \sim (v_{\rm w}^2 + v_{\rm k}^2)^{1/2}$ (Lynch et al. 2018). For simplicity, we adopt an isothermal profile for the stellar wind, $\rho_{\rm w} = \dot{M}_{\rm w}/(4\pi v_{\rm w} R_{\rm orb}^2)$, where $\dot{M}_{\rm w}$ is the stellar mass loss rate (See et al. 2014). The magnetic field of exoplanets shields the stellar wind and deflects the interplanetary particles from reaching the planetary atmosphere. Assuming a dipolar planetary magnetic field, we obtain the magnetic field at the stand-off radius, $B_{\rm p} = B_0(R_{\rm p}/R_{\rm so})^3$, where B_0 is the magnetic field at the equator on the planet's surface ($\sim$ half of the intensity at the magnetic pole) and $R_{\rm p}$ is the planet's radius.

The stand-off radius, $R_{\rm so}$, is estimated by balancing the total pressure of the stellar wind and the planet's magnetic pressure:

$$p_{\rm w} \approx \frac{1}{2}\rho_{\rm w}\Delta v^2 = \frac{B_{\rm p}^2}{8\pi} \ . \tag{9.1}$$

The thermal pressure of the wind is assumed to be negligible compared with its ram pressure (Vidotto et al. 2015). Therefore, the Mach number of the bow shock is given by, $\mathcal{M} = \Delta v / c_{\rm s}$, where $c_{\rm s} = (\Gamma P_{\rm w}/\rho_{\rm w})^{1/2}$ is the sound speed, with $\Gamma \sim 1$ for an isothermal gas, and $P_{\rm w}$ is the wind thermal pressure. For $M_\star \sim M_\odot$, $R_\star \sim R_\odot$ and wind temperature $T_{\rm w} \sim 10^6$ K, the mach number $\mathcal{M} \sim 10$, where $R_\odot$ is the solar radius, consistent with numerical simulations (Vidotto et al. 2015). Therefore, the orbits of close-in hot Jupiters are supersonic, leading to a bow shock with a Mach cone of opening angle $\sim 1/\mathcal{M}$ in the direction of planet's relative motion, that accelerates interplanetary electrons to relativistic energies, producing non-thermal emission.

9.3 Non-Thermal Emission

Next, we calculate the non-thermal emission from the bow shock as the planet plunges through the stellar wind with $\mathcal{M} \gg 1$.

9.3.1 Synchrotron Emission

In analogy with the collisionless shocks around supernova remnants (Helder et al. 2012), the free electrons in the interplanetary medium are expected to be accelerated to relativistic energies via the Fermi acceleration mechanism. Their energy distribution can be described by a broken power-law:

$$N(\gamma)d\gamma = N_0\gamma^{-p}\left(1+\frac{\gamma}{\gamma_{\rm b}}\right)^{-1} \quad (\gamma_{\rm min} \le \gamma \le \gamma_{\rm max})\ , \tag{9.2}$$

where N_0 and p are the normalization factor and power-law index of the electron density distribution, with $\gamma_{\rm b}$, $\gamma_{\rm min}$ and $\gamma_{\rm max}$ being the break, minimum and maximum Lorentz factor, respectively. The electron acceleration timescale is given by $t_{\rm acc} = \xi_{\rm acc}R_{\rm L}c/v_{\rm w}^2$, where $\xi_{\rm acc}$ is a dimensionless constant of unity (Blandford & Eichler 1987), $R_{\rm L} = \gamma m_{\rm e}c^2/eB_{\rm p}$ is the Larmor radius, and $m_{\rm e}$ is the electron mass. The maximum Lorentz factor, $\gamma_{\rm max}$, is obtained by equating $t_{\rm acc}$ to the minimum between the dynamical timescale, $t_{\rm dyn} \sim R_{\rm so}/v_{\rm w}$, and the cooling timescale, $t_{\rm cool} = 3m_{\rm e}c/4(U_{\rm B}+U_\star)\sigma_{\rm T}\gamma$. Here $U_{\rm B} = B_{\rm p}^2/8\pi$ and $U_\star = L_\star/(4\pi R_{\rm so}^2 c)$ are the energy densities of the magnetic field and host star, respectively, and $\sigma_{\rm T}$ is the Thomson cross-section. For typical parameters, we find that $t_{\rm acc} >> t_{\rm dyn}$, and so $\gamma_{\rm max}$ is mainly constrained by $t_{\rm dyn}$. The break Lorentz factor, $\gamma_{\rm b}$, can be obtained by equating $t_{\rm dyn}$ and $t_{\rm cool}$, which yields $\gamma_{\rm b} = 3m_{\rm e}cv_{\rm w}/4\sigma_{\rm T}R_{\rm so}(U_{\rm B}+U_\star)$. We adopt $\gamma_{\rm min} \sim 1$ in the calculation. The power-law index of accelerated electrons, p, is related to the Mach number of the shock, $\mathcal{M}$, through (Drury 1983; Gargaté & Spitkovsky 2012):

$$p = \frac{r+2}{r-1} \tag{9.3}$$

where r is the shock compression ratio, derived from the shock jump condition:

$$r = \frac{(\Gamma+1)\mathcal{M}^2}{(\Gamma-1)\mathcal{M}^2+2} \tag{9.4}$$

$p \sim 2-2.2$ is inferred from numerical simulations of strong shocks (Gargaté & Spitkovsky 2012). Numerical simulation and observations of supernova-driven shock suggests that $p \sim 2.1-2.5$ (Helder et al. 2012; Caprioli & Spitkovsky 2014a). Here, we consider p as a free parameter in the calculation. We assume that a fraction of the kinetic energy of the stellar wind is converted to the total non-thermal luminosity:

$$L_{\rm nt} = \epsilon_{\rm nt} L_{\rm kin} \approx \frac{1}{2}\epsilon_{\rm nt}\rho_{\rm w}\Delta v^3(\pi R_{\rm so}^2) \ , \tag{9.5}$$

where $\epsilon_{\rm nt}$ is the fraction of electrons accelerated to produce non-thermal radiation which we leave as a free parameter in our model. For supernova remnants, $\epsilon_{\rm nt} \sim 5\%$ (Helder et al. 2012).

Next, we compute the synchrotron emission following the standard formula from Rybicki & Lightman (1979). The emission and absorption coefficients are given by:

$$j_\nu^{\rm syn} = c_1 B \int_{\gamma_{\rm min}}^{\gamma_{\rm max}} F(\frac{\nu}{c_1 B \gamma^2}) N(\gamma)\, d\gamma \ , \tag{9.6}$$

$$\alpha_\nu^{\rm syn} = -c_2 B \frac{1}{\nu^2} \int_{\gamma_{\rm min}}^{\gamma_{\rm max}} \gamma^2 \frac{d}{d\gamma}\left[\frac{N(\gamma)}{\gamma^2}\right] F(\frac{\nu}{c_1 B \gamma^2})\, d\gamma \ , \tag{9.7}$$

where $c_1 = \sqrt{2}e^3/4\pi m_{\rm e} c^2$, $c_2 = \sqrt{2}e^3/8\pi m_{\rm e}^2 c^2$, $F(x) \equiv x\int_x^\infty K_{5/3}(\xi)\, d\xi$ and $K_{5/3}(x)$ is the modified Bessel function of 5/3 order. The synchrotron emission peaks at a frequency of $\nu_{\rm syn} = 4.2 \times 10^{14} B_1 \gamma_4^2$ Hz, where $B_1 = (B_{\rm p}/1\,{\rm G})$ and $\gamma_4 = (\gamma/10^4)$. The specific intensity of synchrotron emission can be obtained by the radiative transfer equation (Rybicki & Lightman 1979):

$$I_\nu = \frac{j_\nu^{\rm syn}}{\alpha_\nu^{\rm syn}}\left(1 - e^{-\tau_\nu}\right) \ , \tag{9.8}$$

where τ_ν is the optical depth. The solid lines in Fig. 9.1 show the synchrotron emission for three cases of $\dot{M}_{\rm w}$, which corresponds to solar-type stars ($\dot{M}_{\rm w} \sim 10^{-14}\, M_\odot\,{\rm yr}^{-1}$), T Tauri type stars with intermediate mass loss ($\dot{M}_{\rm w} \sim 10^{-9}\, M_\odot\,{\rm yr}^{-1}$) and massive O/B type stars ($\dot{M}_{\rm w} \sim 10^{-6}\, M_\odot\,{\rm yr}^{-1}$). We apply our model to the non-thermal emission produced by the bow shock from Jupiter in the solar system to constrain our free parameters. For solar wind of mass loss rate $\dot{M}_{\rm w} = 3 \times 10^{-14}\ M_\odot\,{\rm yr}^{-1}$, $R_{\rm orb} \sim 5$ AU, Jovian polar magnetic field $B_{\rm Jup} \sim 7$ G, we find that $R_{\rm so} \sim 40\, R_{\rm jup}$, $\gamma_{\rm max} \sim 100$, consistent with the estimate from de Pater & Dunn (2003). The observed radio flux at 1.4 GHz from Jupiter is $\sim 4 - 5$ Jy (de Pater & Dunn 2003; Zarka 2007), setting an upper limit on $\epsilon_{\rm nt} \lesssim 0.3$, consistent with the value of $\epsilon_{\rm nt} \sim 5\%$ inferred in supernova remnants (Helder et al. 2012).

We find that for massive stars, radio synchrotron emission below ~ 10 GHz is self-absorbed, and emission at $\gtrsim 10$ GHz can be detected at a distance of $\lesssim 300$ pc (see Table 9.1 for details). For intermediate mass stars, synchrotron self-absorption takes place at ~ 1 GHz and radio emission at $\gtrsim 1$ GHz is observable out to ~ 200 pc. For solar-type stars, GHz emission is not affected by self-absorption. However, the low kinetic luminosity of the wind leads to weak non-thermal intensity and the detectability is limited to $\lesssim 100$ pc.

9.3.2 Inverse Compton Scattering

Inverse-Compton (IC) scattering of low-energy photons by the same electrons responsible for the synchrotron emission could produce high-energy radiation. The soft photons are provided by the photosphere of the host star as well as the synchrotron photons. The energy density of the stellar radiation field is $U_\star = L_\star/(4\pi R_{\rm orb}^2 c)$. In comparison, the magnetic field has an energy density of $U_{\rm B} = B_{\rm p}^2/8\pi$. The ratio between synchrotron and IC power is equivalent to the ratio between magnetic and stellar radiation energy density, i.e. $P_{\rm syn}/P_{\rm IC} = U_{\rm B}/U_\star \approx 0.01\, B_1^2 R_{\rm orb,-2}^2 L_{\star,\odot}^{-1}$, where $R_{\rm orb,-2} = (R_{\rm orb}/10^{-2}\,{\rm AU})$, $L_{\star,\odot} = (L_\star/L_\odot)$, $L_\odot$ is the solar luminosity. Thus, we expect significant IC emission from close-in exoplanet systems, such as hot Jupiters. For simplicity, we approximate the spectral energy distribution of the stellar emission as a blackbody spectrum of temperature $T_\star$. The specific intensity of a stellar spectrum can be written as:

$$I_\nu = \frac{L_\star}{4\pi R_{\rm orb}^2 c} f_\nu(T_\star) \ , \tag{9.9}$$

where f_ν is the normalized Planck function. The stellar luminosity-mass relationship can be expressed as $L_\star \propto M_\star^\alpha$, where $\alpha \sim 2.3$, 4.0, 3.5 and 1.0 for $M_\star < 0.43 M_\odot$, $0.43 < M_\star/M_\odot < 2.0$, $2.0 < M_\star/M_\odot < 20$ and $M_\odot > 50 M_\odot$, respectively (Malkov 2007).

The IC scattering of stellar photons peaks at a frequency of $\nu_{\rm IC} \approx \gamma^2 \nu_\star = 5.9 \times 10^{21}\, \gamma_4^2 T_{\star,3}$ Hz, where $\gamma_4 = (\gamma/10^4)$ and $T_{\star,3} = (T_\star/10^3\,{\rm K})$. The differential production rate of high-energy photons with energy $\epsilon m_{\rm e} c^2$ is given by (Coppi & Blandford 1990):

$$Q(\epsilon) = \int d\epsilon_0\, n(\epsilon_0) \int d\gamma N(\gamma)\, K(\epsilon, \gamma, \epsilon_0) \ , \tag{9.10}$$

where $\epsilon_0 m_{\rm e} c^2$ is the soft photon energy, $\gamma m_{\rm e} c^2$ is the electron energy and $n(\epsilon_0)$ is the number density of soft photons. $K(\epsilon, \gamma, \epsilon_0)$ is the Compton kernel, expressed as:

$$\begin{aligned} K(\epsilon, \gamma, \epsilon_0) = \frac{2\pi r_{\rm e}^2 c}{\gamma^2 \epsilon_0} [& 2\kappa \ln \kappa + (1 + 2\kappa)(1 - \kappa) \\ & + \frac{(4\epsilon_0 \gamma \kappa)^2}{2(1 + 4\epsilon_0 \gamma \kappa)} (1 - \kappa)] \ , \end{aligned} \tag{9.11}$$

where $\kappa = \epsilon/[4\epsilon_0 \gamma(\gamma - \epsilon)]$ and $r_{\rm e} = e^2/m_{\rm e} c^2$ is the classical electron radius. The emissivity of IC scattering is given by:

$$j_\nu^{\rm IC} = \frac{h}{4\pi} \epsilon Q(\epsilon) \ , \tag{9.12}$$

where h is Planck's constant.

The expected IC emission for three cases of $\dot{M}_{\rm w}$ is shown by the dashed lines in Fig. 9.1. We find that the X-ray emission is detectable the *Chandra* X-ray Observatory out to a distance of ~ 200 pc for massive stars (see Table 9.1 for details). In particular,

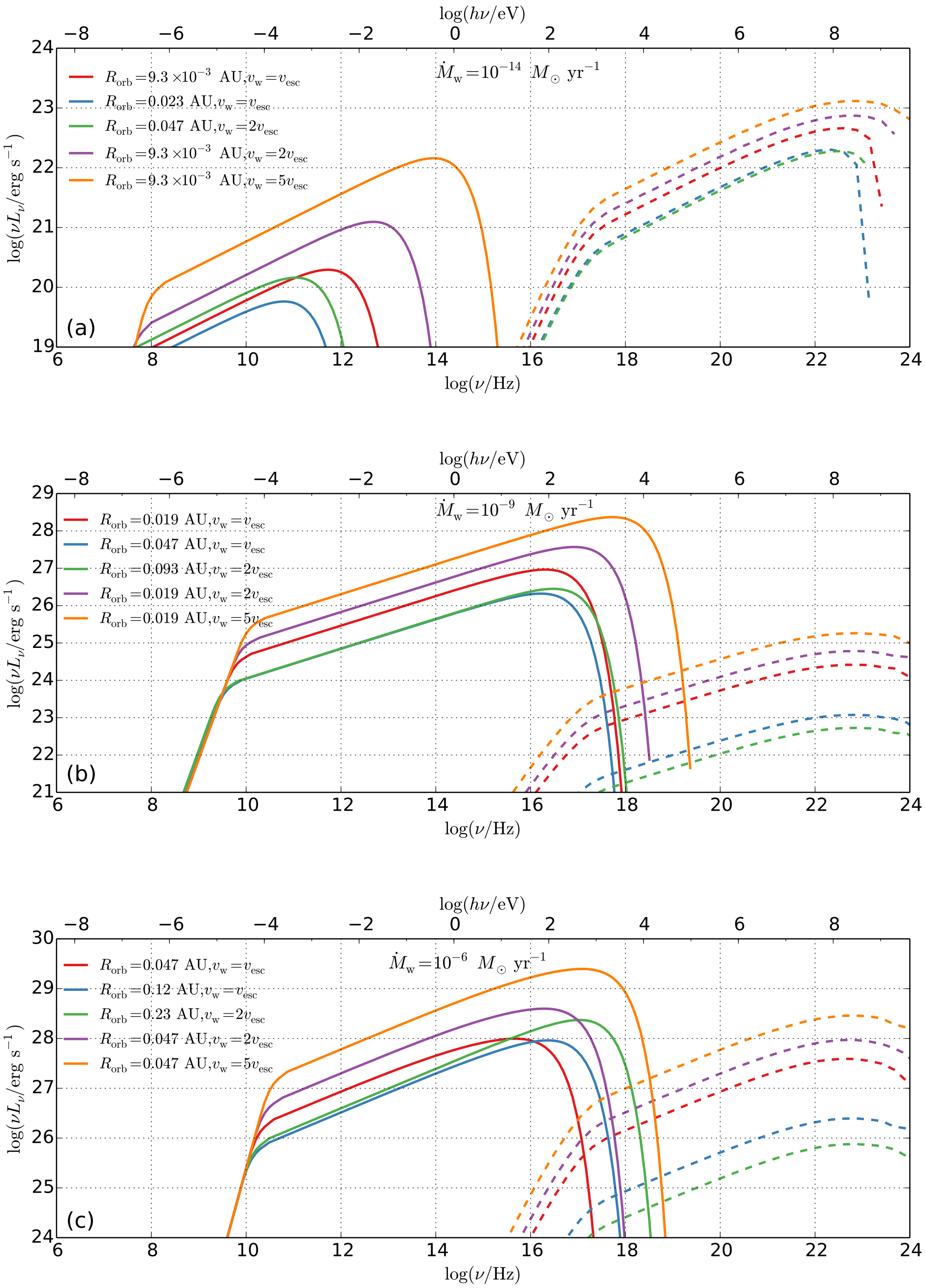

Figure 9.1 Non-thermal emission from stars with a characteristic wind mass loss rate of $\dot{M}_{\rm w} \sim 10^{-14}$, 10^{-9} and 10^{-6} $M_\odot\,{\rm yr}^{-1}$, interacting with Jupiter-like planets, as shown in panel (a)-(c) respectively. The solid and dashed lines corresponds to synchrotron emission and inverse Compton scattering off stellar photons, respectively. The vertical axis shows the luminosity per e-folding in frequency and the horizontal axes show the frequency in Hz (bottom) or the equivalent photon energy in eV (top). In panel (a), $L_\star \sim L_\odot$ and $R_\star \sim R_\odot$. In panel (b), $L_\star \sim 3L_\odot$ and $R_\star \sim 2R_\odot$. In panel (c), $L_\star \sim 10^3 L_\odot$ and $R_\star \sim 5R_\odot$.

for solar-type stars, the total power in IC exceeds the synchrotron power. Thus X-ray observations could detect close-in planets with $R_{\rm orb} \lesssim 5R_\star$.

9.3.3 Detectability

Table 9.1 summarizes the detectability of our calculated non-thermal emission. For solar-type stars ($\dot{M}_{\rm w} = 10^{-14}\ M_\odot\,{\rm yr}^{-1}$), the predicted radio fluxes are detectable out to $\lesssim$ 100 pc with current and upcoming instrumentation. The emission at higher frequencies is too weak for detection. For T Tauri stars ($\dot{M}_{\rm w} = 10^{-9}\ M_\odot\,{\rm yr}^{-1}$), we expect radio detection out to $\sim$ 150 pc. For massive O/B type stars, the emission is bright across all wavelengths from radio to X-rays, and observable out to a distance of $\sim$ 300 pc. Note that synchrotron self-absorption is significant at GHz for massive stars and the spectrum peaks at $\gtrsim$ 8 GHz (see Fig.9.1). Thus, radio observation at higher frequencies is required to detect synchrotron emission from massive stars, in contrast to the CMI expected at low frequencies (Vidotto et al. 2010).

9.4 Application to V380 Tau

We apply our model to V380 Tau, a non-accreting solar mass T-tauri star that hosts a hot Jupiter orbiting at a radius of 0.057 AU, located at a distance of 150 pc (Donati et al. 2016). *Very Large Array* (VLA) observations at a frequency of 6 GHz reveal a flux density $919 \pm 26\,\mu$Jy, along with non-detections at two other epochs corresponding to limits of ¡ 66 and ¡ 150 μJy (Bower et al. 2016). In addition, *Very Long Baseline Array* (VLBA) observations show one detection and one non-detection at comparable sensitivity, which

Table 9.1: Detectability of non-thermal emission from exoplanet bow shock at a distance of 150 pc.

	$\dot{M}_{\rm w} = 10^{-14}\ M_\odot\,{\rm yr}^{-1}$		$\dot{M}_{\rm w} = 10^{-9}\ M_\odot\,{\rm yr}^{-1}$		$\dot{M}_{\rm w} = 10^{-6}\ M_\odot\,{\rm yr}^{-1}$	
Telescopes	F_ν (μJy)	detectability	F_ν (μJy)	detectability	F_ν (μJy)	detectability
JVLA	0.02; 0.004	No; No	0.2; 20	Marginal; Yes	0.3; 380	Marginal; Yes
SKA	0.02; 0.004	No	0.2; 20	Yes	0.3; 380	Yes
ALMA	0.001	No	4.0	Marginal	150	Yes
HST	N/A	No	0.038	Marginal	0.43	Yes
JWST	N/A	No	0.038	Marginal	0.43	Yes
	νF_ν $({\rm erg\,cm^{-2}\,s^{-1}})$	detectability	νF_ν $({\rm erg\,cm^{-2}\,s^{-1}})$	detectability	νF_ν $({\rm erg\,cm^{-2}\,s^{-1}})$	detecatbility
XMM-Newton	10^{-20}	No	4×10^{-15}	Yes	1.9×10^{-13}	Yes
ATHENA	10^{-20}	No	4×10^{-15}	Yes	1.9×10^{-13}	Yes
Chandra	2×10^{-20}	No	5×10^{-15}	Yes	4×10^{-14}	Yes
NuSTAR	2×10^{-20}	No	5×10^{-15}	Marginal	4×10^{-14}	Yes

We choose the characteristic values described in the text as representative examples for the exoplanet systems at a distance of $\sim$ 150 pc. For radio frequencies, we provide fluxes at 1 GHz and 10 GHz, in units of mJy. For X-ray observation, we present νF_ν in units of ${\rm erg\,cm^{-2}\,s^{-1}}$. The telescope detection limits are as follows:

1. *Jansky Very Large Array (JVLA)*: $\sim 1\mu$Jy for 1 σ detection and 12h integration time at most bands (National Radio Astronomy Observatory NRAO).
2. *The Square Kilometer Array (SKA-MID)*: $\sim 0.7\mu$Jy RMS sensitivity for a 10h integration time (Prandoni & Seymour 2014).
3. *The Atacama Large Millimeter/submillimeter Array (ALMA)*: At frequency 345 GHz, the sensitivity $\sim 8.7\,\mu$Jy for 10h integration time is calculated by the *ALMA* Sensitivity Calculator (ASC) (https://almascience.eso.org/proposing/sensitivity-calculator).
4. *Hubble Space Telescope (HST)*: sensitivity $\sim 40-50$ nJy for the wavelength range of $0.6-1.5\,\mu$m for 10σ detection and 10^4 s integration time (Space Telescope Science Institute STScI).
5. *The James Webb Space Telescope (JWST)*: sensitivity $\sim$ 10 nJy for the wavelength range of $1-3\,\mu$m and $\sim$ 30nJy for wavelengths $4-5\,\mu$m for 10σ detection and 10^4 s integration time (Space Telescope Science Institute STScI).
6. *Chandra*: sensitivity of high resolution camera (HRC) $\sim 9 \times 10^{-16}{\rm erg\,cm^{-2}\,s^{-1}}$ covering energy range $0.08-10$ keV for 3σ detection and 3×10^5 s integration time (The Chandra Proposers' Observatory Guide 2014).
7. *XMM-Newton*: $\sim 3.1 \times 10^{-16}\,{\rm erg\,cm^{-2}\,s^{-1}}$ in the $0.5-2.0$ keV band (Hasinger et al. 2001).
8. *Advanced Telescope for High Energy Astrophysics (ATHENA)*: $\sim 4 \times 10^{-17}\,{\rm erg\,cm^{-2}\,s^{-1}}$ in the $0.5-2$ keV band in a 10^6s deep field (Barcons et al. 2012).
9. *Nuclear Spectroscopic Telescope Array (NuStar)*: $\sim 2 \times 10^{-15}\,{\rm erg\,cm^{-2}\,s^{-1}}$ in $6-10$ keV band for 3σ detection and 10^6 s integration time (Harrison et al. 2013).

indicates that the emission might be transient and possibly is non-thermal in origin (Bower et al. 2016). In Fig. 9.2, we fit the non-detection limit of V380 Tau system using the bow shock model with various combination of parameters as listed in Table 9.2. We find that the synchrotron spectrum is steeper at $\nu \lesssim 10$ GHz due to synchrotron self-absorption. An X-ray counterpart of this emission from IC emission is expected, as shown in Fig. 9.1. Additionally, the predicted non-thermal synchrotron emission has a steeper spectrum than the CMI emission estimated from the radiometric Bode's law (Vidotto & Donati 2017). The non-thermal emission model can be applied to CI Tau b, which is around a star of comparable age to V380 Tau (Johns-Krull et al. 2016).

9.5 Discussion

In this chapter, we studied the non-thermal emission produced by the supersonic motion of an exoplanet through the wind of its host stars. This produces a unique fingerprint of the interaction between the planet's magnetosphere and the stellar wind, observable across a broad range of wavelengths from radio to X-rays. In particular, we considered three characteristic cases of stellar wind mass loss rates, namely $\dot{M}_{\rm w} = 10^{-14}, 10^{-9}, 10^{-6}\ M_{\odot}\,{\rm yr}^{-1}$, corresponding to solar-type, T Tauri and massive O/B stars, respectively. We have found that it is challenging to detect emission from solar-type stars farther than ~ 100 pc, but the detection of planets around massive stars is feasible out to a distance of ~ 300 pc. For stars with intermediate mass loss rate, we find that X-ray frequencies allow the detection of exoplanets to a greater distance than their radio emission. For stars with substantial mass loss, the search for radio emission should be restricted to higher frequencies $\gtrsim 10$ GHz as emission at lower frequencies is

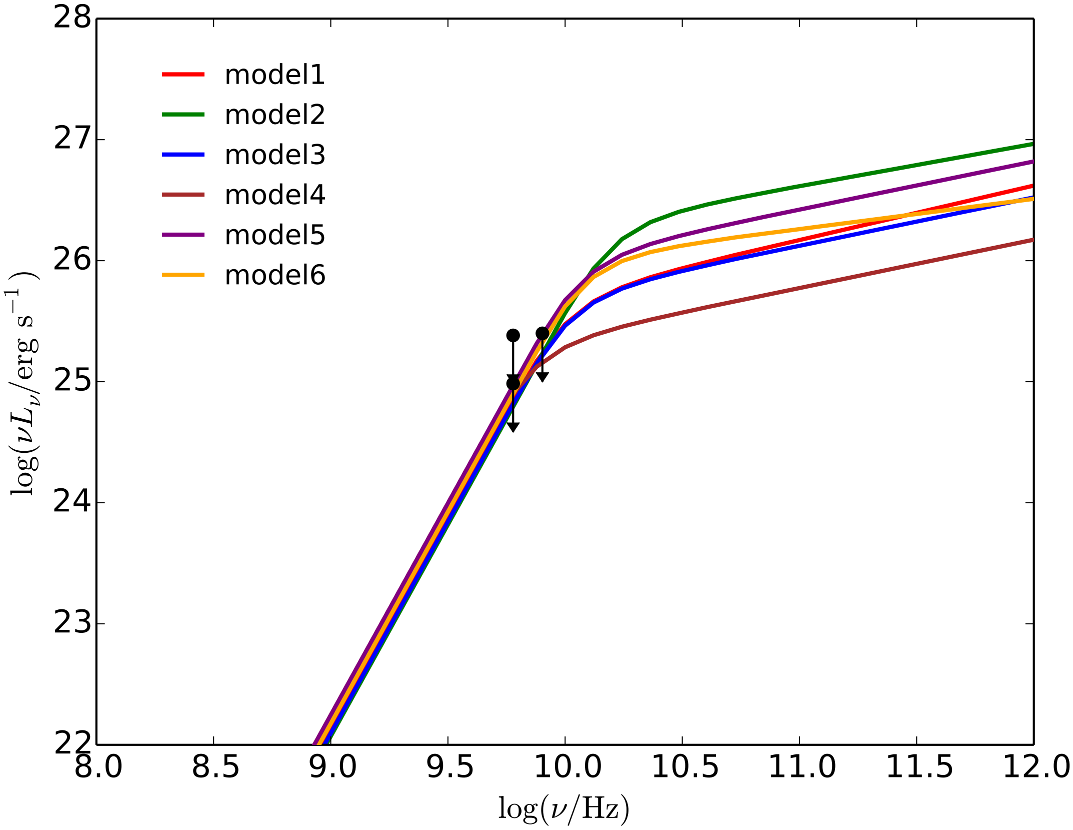

Figure 9.2 Estimated synchrotron emission from V380 Tau for the six models in Table 9.2. We estimate the non-thermal synchrotron emission from the interaction between stellar wind and magnetosphere of the hot Jupiter, constrained by non-detection upper limits from *VLA* and *VLBA* observations.

suppressed by synchrotron self-absorption. We note that the variability of the host star's magnetic field could mask the temporal variability from the bow shock (Llama et al. 2013).

Past observations have searched for radio signatures of cyclotron emission from close-in exoplanets at low radio frequency using instruments such as the Low-Frequency Array (LOFAR) (Zarka 2007). However, radio signatures of cyclotron emission from close-in exoplanets had not yet been detected due to instrumental sensitivity limitations at the ~ 100 MHz frequency range (Bastian et al. 2000), though subtle hints of such emission had been claimed (e.g. O'Gorman et al. (2018)), and was postulated that the beaming of the emission could explain the non-detections (Lenc et al. 2018). Since only a small fraction of the exoplanets orbits is sampled by these observations, there could be an optimal orbital phase for the related radio detection (Lynch et al. 2018). Weber et al. (2017) showed that super-massive planets such as Tau Bootis b and CI Tau b (Johns-Krull et al. 2016) are highly favorable targets for CMI emission. We find that the non-thermal signal is weakly subject to planet's mass, making it more promising for detection of less massive planets than the CMI emission. Another CMI source is the host star itself, which could contaminate the emission from planet (Llama et al. 2018; Cotton et al. 2019). However, the associated frequencies are $\ll$ GHz, below the frequency of the non-thermal emission from planet-host star interaction. In addition to low-frequency CMI searches, we propose to look for the non-thermal signature of these systems at higher frequencies. Our calculations imply a new window for discovering exoplanet systems across a broad range of wavelengths from radio to X-rays. Detection of the emission signal from an exoplanet-wind interaction can provide constraints on the properties of stellar wind as well as the planet's magnetosphere.

Table 9.2. Model parameters of synchrotron emission from V380 Tau

Parameters	$\dot{M}_{\rm w}$ ($M_\odot\,{\rm yr}^{-1}$)	$\Delta v/v_{\rm esc}$	$B_{\rm p}$ (G)	$\epsilon_{\rm nt}$	p
Model 1	5×10^{-9}	6.0	2.0	0.1	2.1
Model 2	5×10^{-9}	6.0	2.0	0.1	2.3
Model 3	1×10^{-8}	2.0	2.0	0.1	2.2
Model 4	6×10^{-10}	3.0	1.0	0.25	2.2
Model 5	1×10^{-8}	1.0	1.0	0.25	2.2
Model 6	1×10^{-10}	7.0	1.0	0.5	2.5

Note. — $\dot{M}_{\rm w}$: stellar wind mass loss rate; $\Delta v/v_{\rm esc}$: the ratio between exoplanet's relative speed to stellar wind and wind speed; $\epsilon_{\rm nt}$: the fraction of wind kinetic luminosity converted to accelerate electrons to relativistic energies; p: the power-law index of non-thermal electrons; $B_{\rm p}$: the magnetic field at the surface of the hot Jupiter.

Acknowledgements

We thank an anonymous referee and John Forbes for insightful comments on the manuscript. This work was supported in part by a grant from the Breakthrough Prize Foundation.

References

Aartsen, M. G., Abraham, K., Ackermann, M., et al. 2015, ApJ, 809, 98

Abdo, A. A., Ackermann, M., Ajello, M., et al. 2010a, Science, 328, 725

—. 2010b, ApJ, 720, 912

Ackermann, M., Ajello, M., Allafort, A., et al. 2012, ApJ, 755, 164

—. 2013, Science, 339, 807

Ackermann, M., Arcavi, I., Baldini, L., et al. 2015a, ApJ, 807, 169

Ackermann, M., Ajello, M., Albert, A., et al. 2015b, ApJ, 799, 86

Ackermann, M., Ajello, M., Atwood, W. B., et al. 2015c, ApJ, 810, 14

Aharonian, F. A., & Atoyan, A. M. 2000, A&A, 362, 937

Ajello, M., Gasparrini, D., Sánchez-Conde, M., et al. 2015, ApJ, 800, L27

Akritas, M. G., & Bershady, M. A. 1996, ApJ, 470, 706

Allard, D., Parizot, E., & Olinto, A. V. 2007, Astroparticle Physics, 27, 61

Aloisio, R., Berezinsky, V., & Gazizov, A. 2011, Astroparticle Physics, 34, 620

Álvarez, E., Cuoco, A., Mirabal, N., & Zaharijas, G. 2016, JCAP, 12, 023

Alvarez-Muñiz, J., & Halzen, F. 2002, ApJ, 576, L33

Alves Batista, R., Boncioli, D., di Matteo, A., van Vliet, A., & Walz, D. 2015, JCAP, 10, 063

Alves Batista, R., & Sigl, G. 2014, JCAP, 11, 031

Anderson, L., Governato, F., Karcher, M., Quinn, T., & Wadsley, J. 2017, MNRAS, 468, 4077

Arata, S., Yajima, H., & Nagamine, K. 2018, MNRAS, 475, 4252

Arav, N., Borguet, B., Chamberlain, C., Edmonds, D., & Danforth, C. 2013, MNRAS, 436, 3286

Arav, N., Chamberlain, C., Kriss, G. A., et al. 2015, A&A, 577, A37

Armitage, P. J., & Natarajan, P. 1999, ApJ, 523, L7

Bahcall, J. N., Kirhakos, S., Saxe, D. H., & Schneider, D. P. 1997, ApJ, 479, 642

Baker, J. G., Centrella, J., Choi, D.-I., et al. 2006, ApJ, 653, L93

Baldwin, J. A., Phillips, M. M., & Terlevich, R. 1981, PASP, 93, 5

Barcons, X., Barret, D., Decourchelle, A., et al. 2012, arXiv e-prints, arXiv:1207.2745

Bastian, T. S., Dulk, G. A., & Leblanc, Y. 2000, ApJ, 545, 1058

Becker, J. K., Biermann, P. L., & Rhode, W. 2005, Astroparticle Physics, 23, 355

Behroozi, P. S., Wechsler, R. H., & Conroy, C. 2013, ApJ, 770, 57

Bellovary, J. M., Governato, F., Quinn, T. R., et al. 2010, ApJ, 721, L148

Beltrametti, M. 1981, ApJ, 250, 18

Berezinsky, V., Gazizov, A., & Grigorieva, S. 2006, Phys. Rev. D, 74, 043005

Blandford, R., & Eichler, D. 1987, Phys. Rep., 154, 1

Blecha, L., & Loeb, A. 2008, MNRAS, 390, 1311

Bluck, A. F. L., Mendel, J. T., Ellison, S. L., et al. 2014, MNRAS, 441, 599

Bogdán, Á., Forman, W. R., Vogelsberger, M., et al. 2013, ApJ, 772, 97

Bogdán, Á., Vogelsberger, M., Kraft, R. P., et al. 2015, ApJ, 804, 72

Bond, J. R., Kofman, L., & Pogosyan, D. 1996, Nature, 380, 603

Boubert, D., Erkal, D., Evans, N. W., & Izzard, R. G. 2017, MNRAS, 469, 2151

Boubert, D., & Evans, N. W. 2016, ApJ, 825, L6

Bouwens, R. J., Illingworth, G. D., Oesch, P. A., et al. 2012, ApJ, 754, 83

Bower, G. C., Loinard, L., Dzib, S., et al. 2016, ApJ, 830, 107

Bower, G. C., Metzger, B. D., Cenko, S. B., Silverman, J. M., & Bloom, J. S. 2013, ApJ, 763, 84

Bromm, V., & Yoshida, N. 2011, ARA&A, 49, 373

Brown, W. R. 2015, ARA&A, 53, 15

Brown, W. R., Geller, M. J., & Kenyon, S. J. 2014, ApJ, 787, 89

Brown, W. R., Geller, M. J., Kenyon, S. J., & Bromley, B. C. 2009, ApJ, 690, L69

Brown, W. R., Geller, M. J., Kenyon, S. J., & Kurtz, M. J. 2006, ApJ, 647, 303

Bustard, C., Zweibel, E. G., & Cotter, C. 2017, ApJ, 835, 72

Campanelli, M., Lousto, C. O., Zlochower, Y., & Merritt, D. 2007, Physical Review Letters, 98, 231102

Caprioli, D. 2012, JCAP, 7, 038

Caprioli, D., & Spitkovsky, A. 2014a, ApJ, 783, 91

—. 2014b, ApJ, 794, 47

Carniani, S., Marconi, A., Maiolino, R., et al. 2015, A&A, 580, A102

Carroll, S. M., Press, W. H., & Turner, E. L. 1992, ARA&A, 30, 499

Celotti, A., & Fabian, A. C. 2004, MNRAS, 353, 523

Chen, P., Wise, J. H., Norman, M. L., Xu, H., & O'Shea, B. W. 2014, ApJ, 795, 144

Chevalier, R. A. 1998, ApJ, 499, 810

Cicone, C., Maiolino, R., Sturm, E., et al. 2014, A&A, 562, A21

Cillis, A. N., Hartman, R. C., & Bertsch, D. L. 2004, ApJ, 601, 142

Collinson, J. S., Ward, M. J., Landt, H., et al. 2017, MNRAS, 465, 358

Coppi, P. S., & Blandford, R. D. 1990, MNRAS, 245, 453

Costa, T., Sijacki, D., & Haehnelt, M. G. 2015, MNRAS, 448, L30

Cotton, D. V., Evensberget, D., Marsden, S. C., et al. 2019, MNRAS, 483, 1574

Courtois, H. M., Zaritsky, D., Sorce, J. G., & Pomarède, D. 2015, MNRAS, 448, 1767

Cresci, G., Mainieri, V., Brusa, M., et al. 2015, ApJ, 799, 82

Crocker, R. M., & Aharonian, F. 2011, Physical Review Letters, 106, 101102

Crocker, R. M., Bicknell, G. V., Taylor, A. M., & Carretti, E. 2015, ApJ, 808, 107

Crocker, R. M., Melia, F., & Volkas, R. R. 2000, ApJS, 130, 339

Cyganowski, C. J., Reid, M. J., Fish, V. L., & Ho, P. T. P. 2003, ApJ, 596, 344

de Pater, I., & Dunn, D. E. 2003, Icarus, 163, 449

Dekel, A., & Silk, J. 1986, ApJ, 303, 39

del Valle, M. V., & Romero, G. E. 2012, A&A, 543, A56

del Valle, M. V., Romero, G. E., & De Becker, M. 2013, A&A, 550, A112

Dermer, C. D., Razzaque, S., Finke, J. D., & Atoyan, A. 2009, New Journal of Physics, 11, 065016

Di Matteo, T., Springel, V., & Hernquist, L. 2005, Nature, 433, 604

Di Mauro, M., Calore, F., Donato, F., Ajello, M., & Latronico, L. 2014, ApJ, 780, 161

Donati, J. F., Moutou, C., Malo, L., et al. 2016, Nature, 534, 662

Drury, L. O. 1983, Reports on Progress in Physics, 46, 973

Dugan, Z., Gaibler, V., & Silk, J. 2017, ApJ, 844, 37

Elvis, M., Wilkes, B. J., McDowell, J. C., et al. 1994, ApJS, 95, 1

Fabian, A. C. 2012, ARA&A, 50, 455

Fang, K., & Olinto, A. V. 2016, ApJ, 828, 37

Farina, E. P., Falomo, R., Scarpa, R., et al. 2014, MNRAS, 441, 886

Faucher-Giguère, C.-A., & Quataert, E. 2012, MNRAS, 425, 605

Ferrara, A., & Scannapieco, E. 2016, ApJ, 833, 46

Feruglio, C., Fiore, F., Carniani, S., et al. 2015, A&A, 583, A99

Fickett, W., & Davis, C. 1979, Detonation

Field, G. B. 1965, ApJ, 142, 531

Finkelstein, S. L., Ryan, Jr., R. E., Papovich, C., et al. 2015, ApJ, 810, 71

Fisher, D. B., & Drory, N. 2011, ApJ, 733, L47

Ford, A. B., Davé, R., Oppenheimer, B. D., et al. 2014, MNRAS, 444, 1260

Fornasa, M., & Sánchez-Conde, M. A. 2015, Phys. Rep., 598, 1

Fu, H., & Stockton, A. 2009, ApJ, 696, 1693

Fujita, Y., Inoue, S., Nakamura, T., Manmoto, T., & Nakamura, K. E. 1998, ApJ, 495, L85

Fukushima, M. 2015, in European Physical Journal Web of Conferences, Vol. 99, European Physical Journal Web of Conferences, 04004

Furlanetto, S. R., & Loeb, A. 2001, ApJ, 556, 619

—. 2003, ApJ, 588, 18

Gaensler, B. M. 2005, Advances in Space Research, 35, 1116

Ganguly, R., Brotherton, M. S., Cales, S., et al. 2007, ApJ, 665, 990

Gargaté, L., & Spitkovsky, A. 2012, ApJ, 744, 67

Garraffo, C., Drake, J. J., & Cohen, O. 2016, ApJ, 833, L4

Gofford, J., Reeves, J. N., McLaughlin, D. E., et al. 2015, MNRAS, 451, 4169

Greisen, K. 1966, Physical Review Letters, 16, 748

Grießmeier, J.-M., Zarka, P., & Girard, J. N. 2011, Radio Science, 46, RS0F09

Guillochon, J., & Loeb, A. 2015, ApJ, 806, 124

Haiman, Z., Thoul, A. A., & Loeb, A. 1996, ApJ, 464, 523

Harrison, C. M., Thomson, A. P., Alexander, D. M., et al. 2015, ApJ, 800, 45

Harrison, F. A., Craig, W. W., Christensen, F. E., et al. 2013, ApJ, 770, 103

Hasinger, G., Altieri, B., Arnaud, M., et al. 2001, A&A, 365, L45

Haswell, C. A., Fossati, L., Ayres, T., et al. 2012, ApJ, 760, 79

Heckman, T. M., & Best, P. N. 2014, ARA&A, 52, 589

Helder, E. A., Vink, J., Bykov, A. M., et al. 2012, Space Sci. Rev., 173, 369

Hillas, A. M. 1984, ARA&A, 22, 425

—. 2006, arXiv Astrophysics e-prints, astro-ph/0607109

Hills, J. G. 1988, Nature, 331, 687

Hinshaw, G., Larson, D., Komatsu, E., et al. 2013, ApJS, 208, 19

Hoffman, L., & Loeb, A. 2007, MNRAS, 377, 957

Holder, G. P., & Loeb, A. 2004, ApJ, 602, 659

Hopkins, P. F., Hernquist, L., Cox, T. J., & Kere, D. 2008, ApJS, 175, 356

Hopkins, P. F., Quataert, E., & Murray, N. 2011, MNRAS, 417, 950

Hopkins, P. F., Richards, G. T., & Hernquist, L. 2007, ApJ, 654, 731

Hopkins, P. F., Torrey, P., Faucher-Giguère, C.-A., Quataert, E., & Murray, N. 2016, MNRAS, 458, 816

Immer, K., Cyganowski, C., Reid, M. J., & Menten, K. M. 2014, A&A, 563, A39

Inoue, T., & Omukai, K. 2015, ApJ, 805, 73

Inoue, Y. 2011, ApJ, 733, 66

Ishibashi, W., & Fabian, A. C. 2012, MNRAS, 427, 2998

—. 2014, MNRAS, 441, 1474

Ito, H., Kino, M., Kawakatu, N., & Orienti, M. 2015, ApJ, 806, 241

Jardine, M., & Collier Cameron, A. 2008, A&A, 490, 843

Ji, S., Oh, S. P., & McCourt, M. 2018, MNRAS, 476, 852

Jiang, Y.-F., Ciotti, L., Ostriker, J. P., & Spitkovsky, A. 2010, ApJ, 711, 125

Johns-Krull, C. M., McLane, J. N., Prato, L., et al. 2016, ApJ, 826, 206

Jones, F. C. 1968, Physical Review, 167, 1159

Kalberla, P. M. W., Burton, W. B., Hartmann, D., et al. 2005, A&A, 440, 775

Kalberla, P. M. W., & Kerp, J. 2009, ARA&A, 47, 27

Karouzos, M., Woo, J.-H., & Bae, H.-J. 2016, ApJ, 819, 148

Kaufmann, T., Mayer, L., Wadsley, J., Stadel, J., & Moore, B. 2006, MNRAS, 370, 1612

Kelner, S. R., Aharonian, F. A., & Bugayov, V. V. 2006, Phys. Rev. D, 74, 034018

Kennicutt, Jr., R. C. 1998, ApJ, 498, 541

Kim, H., & Kim, W.-T. 2009, ApJ, 703, 1278

King, A. 2003, ApJ, 596, L27

King, A., & Pounds, K. 2015, ARA&A, 53, 115

King, A. R., Zubovas, K., & Power, C. 2011, MNRAS, 415, L6

Kislyakova, K. G., Johnstone, C. P., Odert, P., et al. 2014, A&A, 562, A116

Kormendy, J., & Ho, L. C. 2013, ARA&A, 51, 511

Kotera, K., & Olinto, A. V. 2011, ARA&A, 49, 119

Koyama, H., & Inutsuka, S.-i. 2002, ApJ, 564, L97

Kraushaar, W. L., Clark, G. W., Garmire, G. P., et al. 1972, ApJ, 177, 341

Krumholz, M. R., & Dekel, A. 2012, ApJ, 753, 16

Kulkarni, G., & Loeb, A. 2012, MNRAS, 422, 1306

Lamastra, A., Fiore, F., Guetta, D., et al. 2016, A&A, 596, A68

Lara, L., Giovannini, G., Cotton, W. D., et al. 2004, A&A, 421, 899

Larson, R. B. 1969, MNRAS, 145, 405

Lazio, W., T. J., Farrell, W. M., Dietrick, J., et al. 2004, ApJ, 612, 511

Lehner, N., Howk, J. C., Thom, C., et al. 2012, MNRAS, 424, 2896

Lenc, E., Murphy, T., Lynch, C. R., Kaplan, D. L., & Zhang, S. N. 2018, MNRAS, 478, 2835

Libeskind, N. I., Cole, S., Frenk, C. S., & Helly, J. C. 2006, MNRAS, 368, 1381

Licquia, T., & Newman, J. 2014, in American Astronomical Society Meeting Abstracts, Vol. 223, American Astronomical Society Meeting Abstracts #223, 336.04

Llama, J., Jardine, M. M., Wood, K., Hallinan, G., & Morin, J. 2018, ApJ, 854, 7

Llama, J., Vidotto, A. A., Jardine, M., et al. 2013, MNRAS, 436, 2179

Llama, J., Wood, K., Jardine, M., et al. 2011, MNRAS, 416, L41

Loeb, A., & Furlanetto, S. R. 2013, The First Galaxies in the Universe

Loeb, A., & Waxman, E. 2006, JCAP, 5, 003

Lynch, C. R., Murphy, T., Lenc, E., & Kaplan, D. L. 2018, MNRAS, 478, 1763

Macciò, A. V., Moore, B., & Stadel, J. 2006, ApJ, 636, L25

Madau, P., & Quataert, E. 2004, ApJ, 606, L17

Maio, U., Dolag, K., Ciardi, B., & Tornatore, L. 2007, MNRAS, 379, 963

Maiolino, R., Russell, H. R., Fabian, A. C., et al. 2017, Nature, 544, 202

Malkov, O. Y. 2007, MNRAS, 382, 1073

Mannheim, K., Protheroe, R. J., & Rachen, J. P. 2001, Phys. Rev. D, 63, 023003

Marasco, A., Marinacci, F., & Fraternali, F. 2013, MNRAS, 433, 1634

Marconi, A., Risaliti, G., Gilli, R., et al. 2004, MNRAS, 351, 169

Martini, P. 2004, Coevolution of Black Holes and Galaxies, 169

Martini, P., & Weinberg, D. H. 2001, ApJ, 547, 12

McConnell, N. J., & Ma, C.-P. 2013, ApJ, 764, 184

McKee, C. F., & Ostriker, E. C. 2007, ARA&A, 45, 565

McLeod, K. K., & Rieke, G. H. 1995, ApJ, 454, L77

Metzger, B. D., Giannios, D., & Mimica, P. 2012, MNRAS, 420, 3528

Meurs, E. J. A., & van den Heuvel, E. P. J. 1989, A&A, 226, 88

Miller, M. J., & Bregman, J. N. 2013, ApJ, 770, 118

Mo, H., van den Bosch, F. C., & White, S. 2010, Galaxy Formation and Evolution

Moe, M., Arav, N., Bautista, M. A., & Korista, K. T. 2009, ApJ, 706, 525

Mori, M., Ferrara, A., & Madau, P. 2002, ApJ, 571, 40

Moster, B. P., Somerville, R. S., Maulbetsch, C., et al. 2010, ApJ, 710, 903

Mücke, A., Engel, R., Rachen, J. P., Protheroe, R. J., & Stanev, T. 2000, Computer Physics Communications, 124, 290

Murase, K., Ahlers, M., & Lacki, B. C. 2013, Phys. Rev. D, 88, 121301

Murase, K., Beacom, J. F., & Takami, H. 2012, JCAP, 8, 030

Murase, K., Guetta, D., & Ahlers, M. 2016, Physical Review Letters, 116, 071101

Murase, K., & Waxman, E. 2016, Phys. Rev. D, 94, 103006

Murphy, T., Bell, M. E., Kaplan, D. L., et al. 2015, MNRAS, 446, 2560

Narayan, R., & McClintock, J. E. 2008, , 51, 733

Narayan, R., & Yi, I. 1994, ApJ, 428, L13

National Radio Astronomy Observatory (NRAO) website, h. 2014

Navarro, J. F., Frenk, C. S., & White, S. D. M. 1996, ApJ, 462, 563

Nayakshin, S., & Zubovas, K. 2012, MNRAS, 427, 372

Nims, J., Quataert, E., & Faucher-Giguère, C.-A. 2015, MNRAS, 447, 3612

O'Gorman, E., Coughlan, C. P., Vlemmings, W., et al. 2018, A&A, 612, A52

O'Leary, R. M., & Loeb, A. 2009, MNRAS, 395, 781

—. 2012, MNRAS, 421, 2737

Oosterloo, T., Fraternali, F., & Sancisi, R. 2007, AJ, 134, 1019

Pacholczyk, A. G. 1970, Radio astrophysics. Nonthermal processes in galactic and extragalactic sources

Padovani, P., Petropoulou, M., Giommi, P., & Resconi, E. 2015, MNRAS, 452, 1877

Patej, A., & Loeb, A. 2015, ApJ, 798, L20

Peeples, M. S., & Shankar, F. 2011, MNRAS, 417, 2962

Perley, R. A., Chandler, C. J., Butler, B. J., & Wrobel, J. M. 2011, ApJ, 739, L1

Planck Collaboration, Ade, P. A. R., Aghanim, N., et al. 2016, A&A, 594, A13

Prandoni, I., & Seymour, N. 2014, arXiv e-prints, arXiv:1412.6942

Press, W. H., & Schechter, P. 1974, ApJ, 187, 425

Prochaska, J. X., & Hennawi, J. F. 2009, ApJ, 690, 1558

Putman, M. E., Bland-Hawthorn, J., Veilleux, S., et al. 2003, ApJ, 597, 948

Putman, M. E., Peek, J. E. G., & Joung, M. R. 2012, ARA&A, 50, 491

Rappaport, S., Levine, A., Chiang, E., et al. 2012, ApJ, 752, 1

Rashkov, V., & Madau, P. 2014, ApJ, 780, 187

Richings, A. J., & Faucher-Giguère, C.-A. 2018, MNRAS, 478, 3100

Robertson, B. E., Ellis, R. S., Furlanetto, S. R., & Dunlop, J. S. 2015, ApJ, 802, L19

Rupke, D. S., Veilleux, S., & Sanders, D. B. 2005, ApJ, 632, 751

Rupke, D. S. N., & Veilleux, S. 2011, ApJ, 729, L27

Rybicki, G. B., & Lightman, A. P. 1979, Radiative processes in astrophysics

Saul, D. R., Peek, J. E. G., Grcevich, J., et al. 2012, ApJ, 758, 44

Savage, B. D., Narayanan, A., Lehner, N., & Wakker, B. P. 2011, ApJ, 731, 14

Sazonov, S. Y., Ostriker, J. P., Ciotti, L., & Sunyaev, R. A. 2005, MNRAS, 358, 168

Scannapieco, E. 2017, ApJ, 837, 28

Schaye, J., & Dalla Vecchia, C. 2008, MNRAS, 383, 1210

Schneider, E. E., Robertson, B. E., & Thompson, T. A. 2018, ApJ, 862, 56

Scott, A. E., & Stewart, G. C. 2014, MNRAS, 438, 2253

See, V., Jardine, M., Vidotto, A. A., et al. 2014, A&A, 570, A99

Shen, Y., Strauss, M. A., Ross, N. P., et al. 2009, ApJ, 697, 1656

Sheth, R. K., & Tormen, G. 1999, MNRAS, 308, 119

Shibuya, T., Ouchi, M., & Harikane, Y. 2015, ApJS, 219, 15

Shkolnik, E., Bohlender, D. A., Walker, G. A. H., & Collier Cameron, A. 2008, ApJ, 676, 628

Shkolnik, E., Walker, G. A. H., Bohlender, D. A., Gu, P.-G., & Kürster, M. 2005, ApJ, 622, 1075

Shu, F. H. 1992, The physics of astrophysics. Volume II: Gas dynamics.

Silk, J. 1997, ApJ, 481, 703

—. 2013, ApJ, 772, 112

Silk, J., Antonuccio-Delogu, V., Dubois, Y., et al. 2012, A&A, 545, L11

Silk, J., & Rees, M. J. 1998, A&A, 331, L1

Sokołowska, A., Mayer, L., Babul, A., Madau, P., & Shen, S. 2016, ApJ, 819, 21

Somerville, R. S., & Davé, R. 2015, ARA&A, 53, 51

Space Telescope Science Institute (STScI), STScI Newsletter, W. u. 2013, 30, 02

Spitzer, L. 1978, Physical processes in the interstellar medium, doi:10.1002/9783527617722

Spitzer, Jr., L. 1942, ApJ, 95, 329

Springel, V., Di Matteo, T., & Hernquist, L. 2005, MNRAS, 361, 776

Stecker, F. W. 1968, Physical Review Letters, 21, 1016

Stecker, F. W., Malkan, M. A., & Scully, S. T. 2007, ApJ, 658, 1392

Stevens, I. R. 2005, MNRAS, 356, 1053

Sturm, E., González-Alfonso, E., Veilleux, S., et al. 2011, ApJ, 733, L16

Sturner, S. J., Skibo, J. G., Dermer, C. D., & Mattox, J. R. 1997, ApJ, 490, 619

Su, M., Slatyer, T. R., & Finkbeiner, D. P. 2010, ApJ, 724, 1044

Suresh, J., Bird, S., Vogelsberger, M., et al. 2015, MNRAS, 448, 895

Sutherland, R. S., & Dopita, M. A. 1993, ApJS, 88, 253

Tamborra, I., Ando, S., & Murase, K. 2014, JCAP, 9, 043

The Chandra Proposers' Observatory Guide, V. . 2014

The Pierre Auger Collaboration, Aab, A., Abreu, P., et al. 2015, arXiv e-prints, arXiv:1509.03732

Thompson, T. A., Quataert, E., Zhang, D., & Weinberg, D. H. 2016, MNRAS, 455, 1830

Tombesi, F., Meléndez, M., Veilleux, S., et al. 2015, Nature, 519, 436

Tremblay, G. R., Oonk, J. B. R., Combes, F., et al. 2016, Nature, 534, 218

Trenti, M., & Stiavelli, M. 2009, ApJ, 694, 879

Treumann, R. A. 2006, A&A Rev., 13, 229

Tripp, T. M., Meiring, J. D., Prochaska, J. X., et al. 2011, Science, 334, 952

Vidotto, A. A., & Donati, J.-F. 2017, A&A, 602, A39

Vidotto, A. A., Fares, R., Jardine, M., Moutou, C., & Donati, J.-F. 2015, MNRAS, 449, 4117

Vidotto, A. A., Jardine, M., & Helling, C. 2010, ApJ, 722, L168

Villar-Martín, M., Humphrey, A., Delgado, R. G., Colina, L., & Arribas, S. 2011, MNRAS, 418, 2032

Volonteri, M., & Perna, R. 2005, MNRAS, 358, 913

Wakker, B. P., & Savage, B. D. 2009, ApJS, 182, 378

Wang, X., & Loeb, A. 2015, MNRAS, 453, 837

—. 2016a, Nature Physics, 12, 1116

—. 2016b, JCAP, 12, 012

—. 2018, ApJ, 862, L14

Watt, S. D., Sharpe, G. J., Falle, S. A. E. G., & Braithwaite, M. 2012, Journal of Engineering Mathematics, 75, 1

Waxman, E., & Bahcall, J. 1997, Physical Review Letters, 78, 2292

—. 1999, Phys. Rev. D, 59, 023002

Waxman, E., & Loeb, A. 2001, Physical Review Letters, 87, 071101

Weber, C., Lammer, H., Shaikhislamov, I. F., et al. 2017, MNRAS, 469, 3505

Westmeier, T., Brüns, C., & Kerp, J. 2005, A&A, 432, 937

Whalen, D., van Veelen, B., O'Shea, B. W., & Norman, M. L. 2008, ApJ, 682, 49

Willott, C. J., Rawlings, S., Blundell, K. M., Lacy, M., & Eales, S. A. 2001, MNRAS, 322, 536

Winn, J. N., & Fabrycky, D. C. 2015, ARA&A, 53, 409

Wise, J. H., Abel, T., Turk, M. J., Norman, M. L., & Smith, B. D. 2012, MNRAS, 427, 311

Wise, J. H., Demchenko, V. G., Halicek, M. T., et al. 2014, MNRAS, 442, 2560

Wise, M. W., & Sarazin, C. L. 1990, ApJ, 363, 344

Wood, B. E., Müller, H.-R., Zank, G. P., Linsky, J. L., & Redfield, S. 2005, ApJ, 628, L143

Young, S. 2000, MNRAS, 312, 567

Yu, Q., & Tremaine, S. 2002, MNRAS, 335, 965

—. 2003, ApJ, 599, 1129

Zakamska, N. L., & Greene, J. E. 2014, MNRAS, 442, 784

Zandanel, F., Tamborra, I., Gabici, S., & Ando, S. 2015, A&A, 578, A32

Zarka, P. 2007, Planet. Space Sci., 55, 598

Zarka, P., Treumann, R. A., Ryabov, B. P., & Ryabov, V. B. 2001, Ap&SS, 277, 293

Zatsepin, G. T., & Kuz'min, V. A. 1966, Soviet Journal of Experimental and Theoretical Physics Letters, 4, 78

Zel'dovich, Y. B., & Raizer, Y. P. 1967, Physics of shock waves and high-temperature hydrodynamic phenomena

Zubovas, K., & Bourne, M. A. 2017, MNRAS, 468, 4956

Zubovas, K., & King, A. 2012, ApJ, 745, L34

Zubovas, K., & King, A. R. 2014, MNRAS, 439, 400

Zubovas, K., Nayakshin, S., King, A., & Wilkinson, M. 2013, MNRAS, 433, 3079